BUDAPEST UNIVERSITY OF TECHNOLOGY AND ECONOMICS
FACULTY OF MECHANICAL ENGINEERING

Dynamics of Dual-Point Rolling Bodies

A doctoral thesis submitted by

Máté Antali

in partial fulfilment of the requirements for the degree of
Doctor of Philosophy in Mechanical Engineering.

Supervisor:

Dr. Gábor Stépán
professor
Department of Applied Mechanics

Budapest, 2017

The good of the soul does not consist in its thinking much,
but in its loving much.

(Saint Theresa of Avila: The book of her foundations)

Abstract

When a rigid body is in normal contact with two rigid surfaces, rolling or slipping motion can occur at both contact points. This situation leads to four kinematic cases of the body: dual-point rolling, dual-point slipping and two mixed rolling-slipping cases. In case of dual-point rolling, the rolling constraints at the two contact points are not independent; therefore, the contact forces are undetermined in the scope of rigid body dynamics. Hence, the dynamic condition of slipping from the Coulomb model cannot be determined.

This indeterminacy is avoided by analysing the discontinuous vector field of the dynamics of the system. In two-dimensional contact problems of rigid bodies, the Coulomb friction model leads to nonsmooth Filippov type dynamical systems. However, the three-dimensional contact with Coulomb friction is out of the scope of Filippov systems, because it leads to an isolated codimension-2 discontinuity in the phase space. For that purpose, the definition of *extended Filippov systems* is introduced, which is a natural generalisation of Filippov systems. The definition of sliding and crossing regions are defined analogously to usual Filippov systems and the construction of sliding dynamics is presented, as well.

The concept of extended Filippov systems is applied to the problem of the dual-point rolling body, and thus, the indeterminacy of the contact forces is avoided. This mechanical system contains two codimension-2 discontinuity sets in the phase space, and the dual-point rolling dynamics is located in the intersection of these sets. By analysing the vector field of the slipping dynamics in the vicinity of this subset, conditions are determined to decide whether there is a possibility of slipping at one or both contact points.

The developed analytical methods are demonstrated on two mechanical applications. One of them is the dynamics of a railway wheelset running with a constant speed on a straight track. Instead of the commonly used nonlinear creep model, the contact forces are approximated by Coulomb friction. From the discontinuous dynamical system, the conditions of slipping of the wheelset are determined. The maximum amplitude of the oscillations without slipping is derived, as well. In case of dual-point rolling, the effect of the amplitude of the kinematic oscillations is determined on the angular frequency of the oscillations.

The other application is the concept of a special flowmeter, where the flow rate is

measured from the motion of a ball driven by the flow. During usual operation, the ball is in a dual-point rolling contact with the bottom and the wall of a cylindrical vessel. The analysis of the discontinuous system shows that slipping of the ball occur at one or both contact points as the flow rate increases. The variation of the parameters results in several bifurcations of the system.

Acknowledgements

I would like to thank to my supervisor Gábor Stépán for the guidance of my research work since my undergraduate studies. He helped me not only by the valuable suggestions and comments but also by his attitude to mechanics, which inspired me to choose this area. I am also grateful to John S. Hogan for guiding my MSc thesis in Bristol and for the valuable discussions since then.

I would like to thank to Csaba Hős and Zoltán Dombóvári for the useful suggestions during the pre-review process of the thesis. I thank to Eszter Tóth for the language correction of the text.

I would like to offer my thank to my colleagues from the Department of Applied Mechanics for the motivating atmosphere, especially to the guys from the two offices of PhD students. I thank to my friends Csaba Budai and Ákos Vinkó for the new thoughts from different research areas. I am grateful to numerous researchers at conferences for the inspiring ideas and discussions.

I would like to express my thanks to my parents for supporting my studies from all aspects. I am grateful to my baby son Bernát for not typing critical errors to the program codes. I would like to express my gratitude to my wife Noémi for her patience and continuous support during my work.

The research leading to these results has received funding from the European Research Council under the European Union's Seventh Framework Programme (FP/2007-2013) / ERC Advanced Grant Agreement n. 340889. The research was also supported by the Hungarian Scientific Research Foundation OTKA under grant no. K101714.

I would like to thank to the developers and maintainers of the following software, which made it possible that this thesis was produced by using free computer tools only: LaTeX with TeXstudio environment (typesetting), Maxima with wxMaxima environment (algebraic calculations), Armadillo C++ library with CodeBlocks environment (numerical calculations), Gnuplot (plotting), Inkscape (vector graphics) and Ubuntu Linux with MATE desktop (operating system).

Contents

Overview

Outline of the thesis

The thesis is divided into five chapters. The chapters are constructed as units that present the different topics of the research work. However, the chapters are strongly connected to each other as the different topics were developed together during the research (see Figure 1).

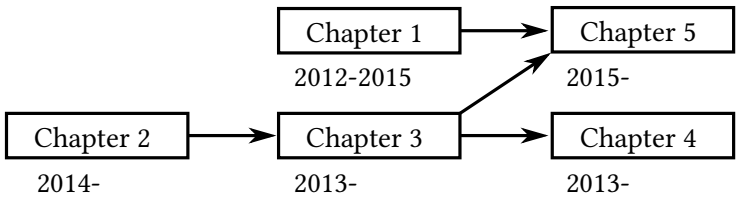

Figure 1: Chapters of the thesis. The arrows show the dependencies between the chapters. The numbers above the chapters denote the years of the corresponding research work.

In Chapter 1, the kinematic oscillations of a single railway wheelset are investigated. If rolling constraints are assumed between the wheelset and both rails then the motion of the wheelset is determined purely by kinematics. The frequency of the nonlinear oscillations is analysed with the exact modelling of the 3D motion of the wheelset. The relation between the amplitude and the frequency of the oscillations is shown, and the effect of the local geometry is derived, as well. The problem of calculating the conditions of slipping on the wheelset in this *dual-point rolling* case leads to the analysis of the following chapters.

In Chapter 2, the concept of Filippov systems is generalised to the codimension-2 case, which leads to the concept of *extended Filippov systems*. In other words, the analysis of dynamical systems is introduced that possess codimension-2 discontinuity surfaces in the phase space. Properties of sliding and crossing are generalised to these systems and the sliding dynamics can be defined similarly to that of simple Filippov systems. The main motivation behind this generalisation is that extended Filippov systems can be used effectively for modelling bodies with spatial Coulomb friction.

In Chapter 3, the general motion of a rigid body is investigated that is in normal

contact with two fixed surfaces. At both contact points, either rolling or slipping can occur, that is, there are four possible kinematic cases of the body. In case of dual-point rolling, the rolling constraints of the two contact points are not independent. Hence, the contact forces cannot be determined from rigid body dynamics, and thus, the condition of slipping cannot be calculated directly from the Coulomb model. However, conditions of slipping can be determined from the dynamics of the slipping cases by using the methods of extended Filippov systems. The resulting procedure is used to obtain the results of Chapters 4 and 5.

In Chapter 4, the dynamics of a flowmeter is analysed where the fluid flows through the device moving a ball along the edge of a cylindrical vessel. During its motion, the ball is in dual-point contact with the vessel, and it is possible that either one contact point or both contact point will slip. The conditions of slipping can be determined from the equations of motion by using the methods of extended Filippov systems. The resulting bifurcation diagrams of the stationary solutions show the limitations of the flowmeter depending on the different parameters.

In Chapter 5, the motion of a single wheelset is analysed by assuming Coulomb friction between the wheels and the rails. In contrast to the smooth nonlinear creep models used in the literature, this approach leads to discontinuous behaviour of the wheelset with switching between rolling and slipping. By the methods of extended Filippov systems, the condition of slipping is determined without calculating the contact forces. The maximum amplitude of the kinematic oscillation is calculated that is possible without the slipping of the wheelset at any of the contact points.

Notes for the reading of the thesis

Introductions to the different topics can be found at the beginning of each chapter. These introduction sections contain the overview of the topic and the corresponding literature. The joint reference list can be found at the end of the thesis. The new results are summarised at the end of each chapter in the form of thesis statements.

During the preparation of the thesis, it seemed hopeless to create a global nomenclature containing all notations of the thesis. Instead, the important notations are summarized in tables at the beginning of each chapter. Symbols with less frequent usage are explained in the text at the first appearance. All along the thesis, the vectors and tensors related to the 3D physical quantities are denoted by boldface letters. All other quantities – including the vectors without a physical meaning – are denoted by italic letters.

Chapter 1

Kinematic oscillations of railway wheelsets

1.1 Introduction

The conical shape of railway wheels is one of the most fundamental achievements in railway dynamics, which was a result of a long empirical development (see [72] for a historical overview). A pair of wheels are fixed rigidly to each other, and thus, there is no possibility for different rotating speeds of the wheels in railway curves. Still, rolling is possible at both wheels because due to the conical profile shape, the lateral displacement of the wheelset changes the rolling radii of the wheels (see Figure 1.2). This effect ensures steering of the vehicle in curves without any active intervention.

The side-effect of the conical shape is the appearance of the so-called *hunting oscillations* which are induced by the geometry of the profiles, and which are modified by several physical effects (see Figure 1.3). In usual circumstances, the local deformations at the wheel–rail contact are significant, and the resulting *creep effect* has to be included in the kinematic and dynamic description of the wheelset. This topic is discussed in more details in Chapter 5 of this thesis. See [35] for a brief overview or [14] for a more detailed description of the different models.

In the limit case of small deformations, the creep effect can be neglected and it can be assumed that there is pure rolling at the contact of both wheels. Then, the oscillations are purely determined by the geometry of the bodies; thus, they are called *kinematic oscillations*. The concept of kinematic oscillation is more important than being only a theoretical limit case. At low velocity of the vehicles, the kinematic description is a good approximation of the problem. It was shown that an isolated wheelset with creep effect provides oscillations which has a frequency very close to the kinematic oscillations [71], and this frequency can appear at the motion of a whole vehicle, too [64]. The frequency of kinematic oscillation appears in small-scale experiments, as well [45, 66], where the deformations are negligible. In the standards, the quantity of *equivalent conicity* is calculated from the kinematic oscillations [22, 67].

	Variable	Meaning
geometric parameters	r	rolling radius of the wheelset
	b	half-distance between contact points
	δ	contact angle
	h	nominal conicity (tangent of the contact angle, $h = \tan\delta$)
	R_r	radius of curvature of the rail profile
	R_w	radius of curvature of the wheel profile
	R_w', R_r'	derivatives of the radii of the curvatures along the profile curves
	R_w'', R_r''	second derivatives of the radii of the curvatures along the profile curves
parametric surfaces	$c_r(U_r)$	profile curve of the rails
	$c_w(U_w)$	profile curve of the wheels
	U_r, U_w	variables of the profile curves (distance along the axle of the wheelset)
	$\mathbf{e}_1, \mathbf{e}_2, \mathbf{e}_3$	basis vectors of the coordinate system
	$\mathbf{f}_r^{\pm}(U_r, V_r)$	surface of the rails (left and right)
	V_r	variable for the distance along the rails
	$\mathbf{f}_r^{\pm}(U_w, V_w)$	surface of the wheels in central position (left and right)
	V_w	variable for the angle around the sufrace of the wheelset
	$\hat{\mathbf{f}}_r^{\pm}(U_w, V_w)$	surface of the wheels in general position (left and right)
kinematics	w, y, z	longitudinal, lateral and vertical displacements of the geometric centre of the wheelset
	ψ	yaw angle of the wheelset (vertical axis)
	ϑ	roll angle of the wheelset (longitudinal axis)
	φ	rotation angle of the wheelset around its axle
	$U_r^{\pm}, V_r^{\pm}$	coordinates of the contact points on the surface of the rails
	$U_w^{\pm}, V_w^{\pm}$	coordinates of the contact points on the surface of the wheels
	q	vector of generalised coordinates
	$\hat{q}$	vector of dependent variables
kinematic oscillations	v	speed of the wheelset along the track
	ω_L	angular frequency of small amplitude kinematic oscillations (linear case)
	ω_{Kli}	approximation of the angular frequency by Klingel
	$\omega_{\text{Heu}}, \omega_{\text{Lor}}, \omega_{\text{Mei}}$	improvements of Klingel's approximation in the literature
	λ_L	wavelength of small amplitude oscillations
	h_L^*	equivalent conicity for small amplitude oscillations
	$\bar{y}$	amplitude of the kinematic oscillations
	$\omega_N(\bar{y})$	angular frequency of finite amplitude kinematic oscillations (nonlinear case)
	$h_N^*(\bar{y})$	equivalent conicity for finite amplitude oscillations
	$\lambda_N(\bar{y})$	wavelength of finite amplitude oscillations
	a_{01}, b_{10}	linear coefficients of the differential equations
	$a_{03}, a_{21}, b_{30}, b_{12}$	nonlinear coefficients of the differential equations
	β	nonlinearity factor

Table 1.1: Important notations of Chapter 1.

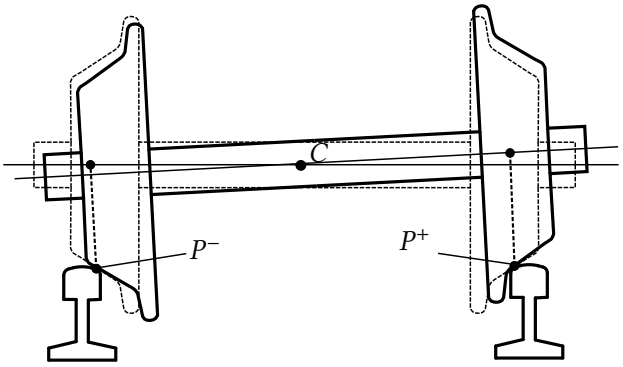

Figure 1.2: The change of the rolling radii of the wheelset due to the lateral displacement of the wheelset. The dotted lines denote the rolling radii in displaced position, and P^+ and P^- are the contact points. In the figure, the cone angle is shown exaggeratedly. In practice, the conicity of the wheelset is about 1:100−1:20.

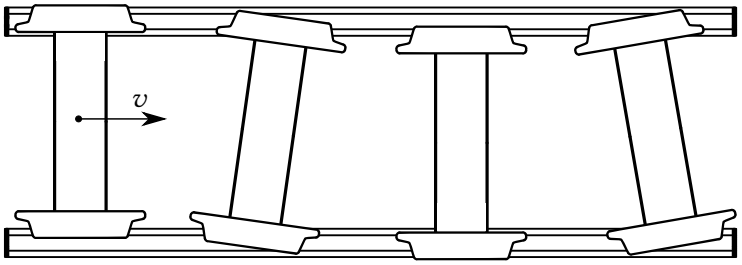

Figure 1.3: The oscillation of a railway wheelset on a straight track. These oscillations are superposed onto the top of the stationary rolling of the wheelset. In general, these oscillations are called *hunting oscillations*. The limit case of small deformations and pure rolling results in the case of *kinematic oscillations*.

The basic mechanical description of kinematic oscillations originates from the XIX. century and these relations are contained in every textbook of railway dynamics (see e.g. [14]). Yet, there are many inaccuracies and unexplained approximations in the literature. Many inaccuracies arise from the incorrect calculation of the three-dimensional rotation of the wheelset. The exact three-dimensional description of motion of the wheelset can be found in only a few works in the literature, and it is still not applied to kinematic oscillation. In his works, de Pater applied the 3D description of the motion to model the geometric constraint between the wheels and the rails accurately [18, 27]. The accurate calculation of multiple contact points needs the 3D description of motion, too (see e.g. [1]).

The motivation behind research work of this chapter was to achieve a thorough 3D description of kinematic oscillation of a railway wheelset assuming straight track and identical profiles at both wheels. The main goals of the chapter are to determine the

frequency of kinematic oscillations and its analytical dependence on the *geometry* of the bodies. The *nonlinear* dynamics of the wheelset is considered to reveal the effect of the *amplitude* on the frequency of oscillations. The first ideas of this chapter were presented in the Master's Thesis of the author [2], and in the next years, further results were published in three papers [12, 4, 9]. In a large part of this chapter, the discussion of [9] is followed.

The structure of the chapter is the following. Section 1.2, contains an overview of the results in the literature related to the frequency of kinematic oscillations. In Section 1.3, the new mechanical model is introduced and the differential equations of the system are derived. In Section 1.4, the angular frequency of kinematic oscillations is derived for the linear (small-amplitude) and for the nonlinear (finite amplitude) cases. The concept of *nonlinearity factor* is introduced which measures the change of the frequency when the amplitude of the oscillation is increasing. In Section 1.5, the formulae of the kinematic parameters are derived from the geometry of the wheel and rail profiles. The new results are summarised in Section 1.6.

1.2 Existing results in the literature

A single wheelset is considered running on a straight track with a constant speed v (see Figure 1.3). In this section, the existing methods and formulae are presented to determine the frequency (angular frequency) of the oscillations.

1.2.1 Klingel's approximate formula for small oscillations

The first approximate formula for the frequency of kinematic oscillations was determined by Klingel [43]. A possible derivation of this fundamental formula is presented below. For an alternative derivation, see e.g. [72], p. 8.

During this „naive" linearisation, it is required that the lateral displacement y of the wheelset and the yaw angle ψ is small (see Figure 1.4). Moreover, it is assumed that the nominal contact angle δ between the wheels and the rails is small in the sense that the roll angle ϑ and the vertical displacement z can be completely neglected. Then, the time derivative of the lateral displacement can be approximated by

$$\dot{y} \approx v \tan\psi \approx v\psi \tag{1.1}$$

The angular velocity $\boldsymbol{\Omega}$ of the wheelset and the position vector $\mathbf{r}_{P^+P^-}$ between the contact points (see Figure 1.2) can be approximated by

$$\boldsymbol{\Omega} \approx \begin{bmatrix} 0 \\ v/r \\ \dot{\psi} \end{bmatrix}, \qquad \mathbf{r}_{P^+P^-} \approx \begin{bmatrix} 0 \\ -2b \\ \Delta r(y) \end{bmatrix}, \tag{1.2}$$

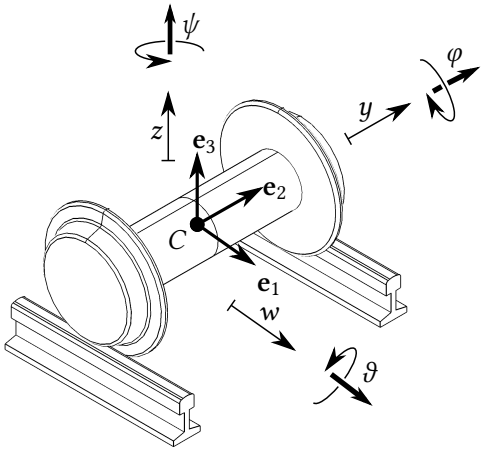

Figure 1.4: Quantities for describing the kinematics of the wheelset.

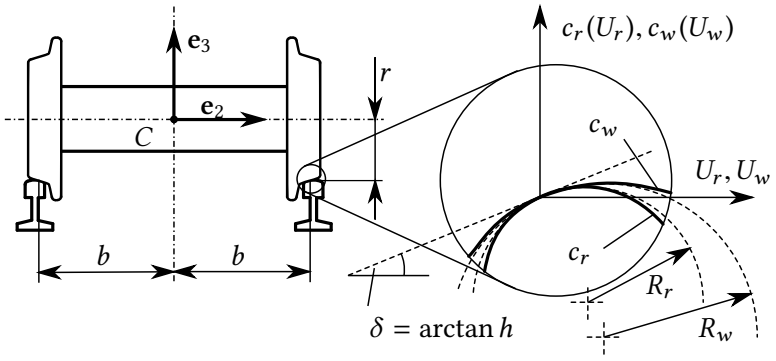

Figure 1.5: Geometric parameters of the wheelset in the central position.

where b is the distance between the contact points, r is the rolling radius of the wheelset in the central position (see Figure 1.5), and $\Delta r(y)$ is the difference between the rolling radii of the wheels at a laterally displaced position (see Figure 1.2).

The wheelset is rolling at both points P^+ and P^-, that is, the angular velocity Ω is parallel to $\mathbf{r}_{P^+P^-}$. This leads to

$$\dot{\psi} \approx -v \cdot \frac{\Delta r(y)}{2br}. \tag{1.3}$$

Equations (1.1) and (1.3) form a system of two first-order differential equations, and they can be transformed to a single second-order differential equation in the form

$$\ddot{y} + v^2 \frac{\Delta r(y)}{2br} \approx 0. \tag{1.4}$$

For purely conical wheels, the rolling radius difference can be approximated by

$$\Delta r(y) \approx 2hy, \tag{1.5}$$

where $h = \tan\delta$ denotes the conicity of the wheels. Then, (1.4) provides harmonically oscillating solutions in the form

$$y(t) = \bar{y} \cdot \cos(\omega_{\text{Kli}} \cdot t), \tag{1.6}$$

where $\bar{y}$ is the amplitude and

$$\omega_{\text{Kli}} = v\sqrt{\frac{h}{br}} \tag{1.7}$$

is the *angular frequency* of the kinematic oscillations. This formula is called Klingel's Formula, which was published already in 1883 [43]. In the literature, (1.7) is often presented for the frequency, time period or wavelength of oscillations, but angular frequency contains the same information about the phenomenon.

1.2.2 Improvements of the linear formula

Instead of the approximate formula (1.7), more accurate formulae can also be found in the literature. In 1937, Heumann [32] published the improved formula

$$\omega_{\text{Heu}} = v\sqrt{\frac{h}{br} \cdot \frac{R_w}{R_w - R_r}} \tag{1.8}$$

where R_w and R_r are the radii of curvature of the wheel and rail profile, respectively (see Figure 1.5). This formula shows that for *worn* wheel profiles, where R_w and R_r are possibly close to each other, the frequency of oscillations can be much higher than predicted by (1.7). In the limit case $R_w \to \infty$ of the conical wheels, (1.8) tends to (1.7). The formula (1.8) was still derived by using a similar „naive" linearisation that is presented in the previous subsection.

In 1993, Lorant [49] derived the formula

$$\omega_{\text{Lor}} = v\sqrt{\frac{h}{br} \cdot \left(1 + \frac{R_r h}{b\sqrt{1+h^2}}\right)}, \tag{1.9}$$

which is valid for rail profiles with constant curvature and *purely conical* wheels. This is an exact formula obtained by linearising the nonlinear differential equations of the wheelset. In the limit case $h \to 0$, (1.9) tends to Klingel's Formula.

In 2002, Meijaard [63] published the formula

$$\omega_{\text{Mei}} = v\sqrt{\frac{h}{br} \cdot \frac{R_w}{R_w - R_r} \cdot \left(1 + \frac{R_r h}{b\sqrt{1+h^2}}\right)}. \tag{1.10}$$

The derivation of this formula cannot be found neither in [63] nor in [52], but it was presumably derived by exact linearisation. It is not clear whether (1.10) is valid for the case when the radii of the curvature are *not constant*. Meijaard also derived a more general formula for the case when the radii of curvatures are not the same at the two wheels [53].

1.2.3 Effects of the amplitude of the oscillations

Linear formulae (1.7)-(1.10) are valid for *small-amplitude* kinematic oscillations. However, the increasing amplitude may cause a substantial change in the frequency of kinematics oscillations. This dependence is denoted by the function $\omega_N(\bar{y})$ with $\omega_N(0) = \omega_L$, where ω_L denotes the *linear* angular frequency (for small amplitudes) and ω_N denotes the *nonlinear* angular frequency (for finite amplitudes).

In the literature (see e.g. [58] or p. 107 of [14]) and in the standards (see [67, 22]), the dependence of the angular frequency on the amplitude is connected to the concept of *equivalent conicity* (sometimes called *effective conicity*). The equivalent conicity h^* can be defined by

$$\omega_L = v\sqrt{\frac{h_L^*}{br}} \tag{1.11}$$

for small oscillations and by

$$\omega_N(\bar{y}) = v\sqrt{\frac{h_N^*(\bar{y})}{br}} \tag{1.12}$$

for finite oscillations, where h_L^* and h_N^* denote the equivalent conicity for the small and finite amplitudes, respectively. As a limit case of small oscillations, $h_N^*(0) = h_L^*$ holds. In fact, the value of equivalent conicity provides the conicity of a purely conical wheelset for which Klingel's formula (1.7) provides the desired angular frequency. For purely conical wheels, $h^* \approx h$, the exact dependence can be expressed from (1.9).

Differential equation (1.4) contains the dependence on the lateral displacement y, which is usually the basis of calculation in the literature. Equation (1.4) can be used to calculate an approximate numerical dependence of the equivalent conicity $h_N^*(\bar{y})$ from the rolling radius difference function $\Delta r(y)$ [22, 67]. For describing the *change* of the equivalent conicity due to the amplitude, Polach suggests a *nonlinearity parameter* [58], which is based on chord approximation of the slope of the function $h_N^*(\bar{y})$.

All these methods in the literature can be applied numerically, and the dependence of angular frequency on the amplitude can be determined from measurements, as well. Yet, there exists no analytical formula to calculate this relation from the geometry of the profiles. To determine such formula is one of the main goals of this chapter.

1.3 Mechanical model with full 3D description

In this section, the a mechanical model is introduced to derive the differential equations of the system. First, the 3D description of the geometry and the motion is presented. Then, the geometric and kinematic constraints are applied to get the differential equations of the system.

1.3.1 Geometry and kinematics

The *nominal* contact points are defined as the contact points in the central position of the wheelset. Assume that the left and right wheels and rails are identical. The profile curves of the rails and the wheels are denoted by $c_r(U_r)$ and $c_w(U_w)$, respectively. The variables U_r and U_w measure the distance along the axle of the wheelset, and at the nominal contact point, $c_r(0) = c_w(0) = 0$ (see Figure (1.5)). In the subsequent analysis, it is required that the curves c_r and c_w are *four* times differentiable at the nominal contact point. This requirement is valid for a general *worn* wheelset, but it is satisfied many new wheels, as well, if the amplitude of the oscillations is not too large.

The surfaces of the wheels and the rails are expressed by explicit parametric surfaces. Let $\mathbf{e}_1, \mathbf{e}_2, \mathbf{e}_3$ denote the basis vectors of the coordinate system and let the origin be located at geometric centre C of the wheelset in its central position (see Figure 1.4-1.5). Then, the prismatic surfaces $\mathbf{f}_r^+$ and $\mathbf{f}_r^-$ of the rails are given by

$$\mathbf{f}_r^{\pm}(U_r, V_r) := \begin{bmatrix} V_r \\ \pm(b + U_r) \\ -r + c_r(U_r) \end{bmatrix}, \tag{1.13}$$

where b is the half-distance of the contact points, r is the nominal rolling radius of the wheels and the coordinate V_r measures the distance along the rails. Along this chapter, the superscripts + and − correspond to the left (+) and right (-) wheels (see Figure 1.4), and the superscript ± is used as shorthand notation for both cases.

In *central position*, we can express also the surfaces $\mathbf{f}_w^+$ and $\mathbf{f}_w^-$ of the wheels in explicit parametric form,

$$\mathbf{f}_w^{\pm}(U_w, V_w) := \begin{bmatrix} (-r + c_w(U_w)) \sin V_w \\ \pm(b + U_w) \\ (-r + c_w(U_w)) \cos V_w \end{bmatrix}, \tag{1.14}$$

where V_w denotes the angle measured along the circumference of the wheels. In *general position*, the surfaces of the wheels are transformed to $\hat{\mathbf{f}}_w^+$ and $\hat{\mathbf{f}}_w^-$, where

$$\hat{\mathbf{f}}_w^{\pm}(U_w, V_w) = \begin{bmatrix} 1 & 0 & 0 \\ 0 & \cos\vartheta & -\sin\vartheta \\ 0 & \sin\vartheta & \cos\vartheta \end{bmatrix} \cdot \begin{bmatrix} \cos\psi & -\sin\psi & 0 \\ \sin\psi & \cos\psi & 0 \\ 0 & 0 & 1 \end{bmatrix} \cdot \begin{bmatrix} \cos\varphi & 0 & \sin\varphi \\ 0 & 1 & 0 \\ -\sin\varphi & 0 & \cos\varphi \end{bmatrix} \cdot \mathbf{f}_w^{\pm}(U_w, V_w) + \begin{bmatrix} w \\ y \\ z \end{bmatrix}. \tag{1.15}$$

The variables w, y, z measure the displacement of the geometric centre C from the central position, and the Euler angles ϑ, ψ and φ describe the orientation of the wheelset (see Figure 1.4). According to the convention of the literature, ϑ is called *roll angle*, ψ is called *yaw angle* and φ is the rotation angle of the wheelset around its axle. (Note in [12], the authors used a different naming convention.)

By direct calculation, the velocity of a point on the surface of the wheels can be expressed by

$$\mathbf{v}^{\pm}(U_w, V_w) = \begin{bmatrix} \dot{\vartheta} - \dot{\varphi}\sin\psi \\ \dot{\varphi}\cos\psi\cos\vartheta - \dot{\psi}\sin\vartheta \\ \dot{\varphi}\cos\psi\sin\vartheta + \dot{\psi}\cos\vartheta \end{bmatrix} \times \left(\hat{\mathbf{f}}_w^{\pm}(U_w, V_w) - \begin{bmatrix} w \\ y \\ z \end{bmatrix} \right) + \begin{bmatrix} \dot{w} \\ \dot{y} \\ \dot{z} \end{bmatrix}. \tag{1.16}$$

1.3.2 Geometric constraints

In general position of the wheelset, let (U_w^+, V_w^+) and (U_w^-, V_w^-) denote the location of the contact points on the surfaces of the wheels, and let us use the notations (U_r^+, V_r^+) and (U_r^-, V_r^-) similarly to the rails. As the wheels and rails are in contact in these points, we require

$$\mathbf{f}_r^{\pm}(U_r^{\pm}, V_r^{\pm}) = \hat{\mathbf{f}}_w^{\pm}(U_w^{\pm}, V_w^{\pm}). \tag{1.17}$$

Moreover, the surfaces of the wheels and the rails are tangent to each other, which can be expressed by

$$\begin{aligned} \left(\frac{\partial \hat{\mathbf{f}}_w^{\pm}}{\partial U_w} \times \frac{\partial \hat{\mathbf{f}}_w^{\pm}}{\partial V_w} \right)(U_w^{\pm}, V_w^{\pm}) \cdot \frac{\partial \mathbf{f}_r^{\pm}}{\partial U_r}(U_r^{\pm}, V_r^{\pm}) = 0, \\ \left(\frac{\partial \hat{\mathbf{f}}_w^{\pm}}{\partial U_w} \times \frac{\partial \hat{\mathbf{f}}_w^{\pm}}{\partial V_w} \right)(U_w^{\pm}, V_w^{\pm}) \cdot \frac{\partial \mathbf{f}_r^{\pm}}{\partial V_r}(U_r^{\pm}, V_r^{\pm}) = 0. \end{aligned} \tag{1.18}$$

The mixed product in (1.18) expresses that at each contact point, the partial derivatives of the surface functions must lay in the same plane.

The constraints (1.17)-(1.18) contain 10 independent scalar equations (see later in (1.46)-(1.47)), and there are 14 scalar variables (6 variables from the rigid body motion (1.15) and the 8 variables related to the loci of the contact points on the surfaces). That is, $14 - 10 = 4$ generalised coordinates can be chosen. Let the vector of generalised coordinates be

$$q := \left[y, \psi, \varphi, w \right]. \tag{1.19}$$

This choice of independent variables proves to be appropriate to express all other variables. The vector of dependent variables is denoted by

$$\hat{q} := \left[\vartheta, z, U_r^+, U_r^-, V_r^+, V_r^-, U_w^+, U_w^-, V_w^+, V_w^- \right]. \tag{1.20}$$

1.3.3 Kinematic constraints and differential equations

When the wheelset is rolling at both contact points, the velocity is zero at the contact points, that is,

$$\mathbf{v}^{\pm}(U_w^{\pm}, V_w^{\pm}) = \mathbf{0}. \tag{1.21}$$

From these 6 scalar constraint equations, 2 equations can be eliminated since in the normal direction of the surfaces, the velocity is already fixed to zero by the geometric

constraints. A further equation can be also eliminated because the velocities of the two points of a rigid body cannot be chosen fully independently. That is, (1.21) leads to 3 independent scalar equations.

A further kinematic constraint prescribes that the velocity of the geometric centre of the wheelset along the track has constant value v, that is,

$$\dot{w} = v. \tag{1.22}$$

The independent components of kinematic constraints (1.21)-(1.22) lead to four independent linear scalar equations for the time derivatives $\dot{q}$ of the generalised coordinates (see later in (1.48)). Thus, the derivatives of the four generalised coordinates can be formally written as

$$\begin{aligned} \dot{y} &= f_y(y, \psi, w, \varphi), \\ \dot{\psi} &= f_\psi(y, \psi, w, \varphi), \\ \dot{\varphi} &= f_\varphi(y, \psi, w, \varphi), \\ \dot{w} &= v. \end{aligned} \tag{1.23}$$

The set (1.23) of four first-order differential equations describes the dynamics of the wheelset. That is, the motion of the system is determined purely by the constraints, and there is no need for considering Newton's Second Law or the Euler–Lagrange equations. In fact, this system corresponds to the special case of Gibbs–Appell equations ([26], p. 254) where no quasi-velocities remain.

Note, that the right-hand side of (1.23) cannot be expressed explicitly because geometric constraints (1.17)-(1.18) lead to implicit equations of trigonometric functions (see below in (1.46)-(1.47)). In Section 1.4, the formal relation between the frequency and the amplitude is derived from the structure and the symmetries of (1.23). In Section 1.5, the truncated Taylor series of (1.23) is produced to derive the dependence of this relation on the geometrical parameters.

1.4 Linear and nonlinear kinematic oscillations

In this section, the structure of the differential equations is utilized to characterize the kinematic oscillations of the wheelset. The main objective is to describe the formal dependence of the angular frequency on the amplitude of the oscillations by a few parameters. The values of these parameters are calculated from the geometry of the profiles in Section 1.5.

1.4.1 Symmetries

By considering symmetries of the system, many properties of (1.23) can be predicted before calculating the actual formulae. The system has a translation symmetry with

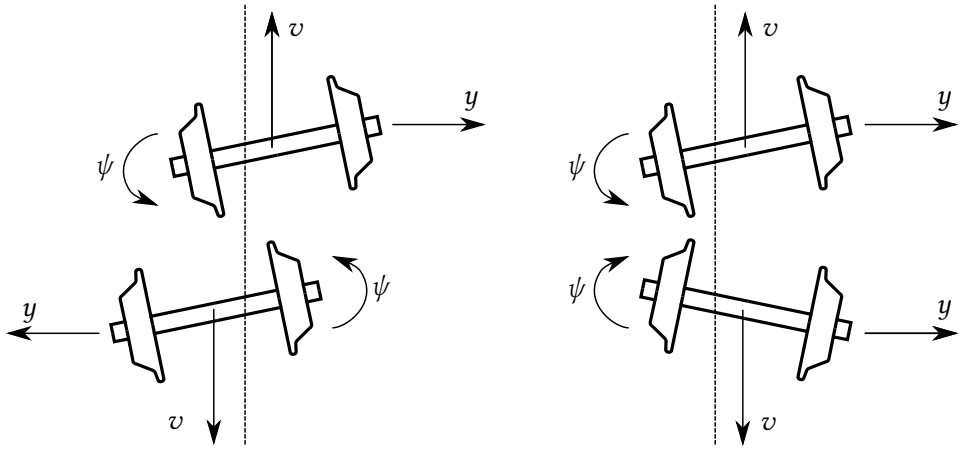

Figure 1.6: The symmetries of the system. The dotted line denotes the centreline of the track. Left panel: the rotation symmetry (1.25). Right panel: the reflection symmetry (1.26).

respect to the location of the wheelset along the track, that is, the right-hand side of (1.23) does not depend on w . Moreover, the rotational symmetry of the wheelset around its axle results in the missing of the dependence on φ, too. Hence, (1.23) should have the form of

$$\begin{aligned} \dot{y} &= f_y(y, \psi), \\ \dot{\psi} &= f_\psi(y, \psi), \\ \dot{\varphi} &= f_\varphi(y, \psi), \\ \dot{w} &= v. \end{aligned} \tag{1.24}$$

In other words, the variables w and φ are *cyclic variables*, that is, they do not effect the dynamics of the other variables. Therefore, the first two equations of (1.24) can be investigated separately, and the dynamics can be reduced to the plane of y and ψ.

There are further symmetries in the system (see Figure 1.6). Consider the rotation of the wheelset about the vertical axis z by 180 degrees, which corresponds to the transformation $y \to -y$ and $v \to -v$ (see the left panel of Figure 1.6). As the change of the direction of the velocity v should change the signs of $\dot{y}$ and $\dot{\psi}$, we require

$$f_y(-y, \psi) = f_y(y, \psi), \qquad f_\psi(-y, \psi) = -f_\psi(y, \psi). \tag{1.25}$$

Similarly, consider the reflection of the wheelset about the plane yz, which is related to the transformation $\psi \to -\psi$ and $v \to -v$ (see the right panel of Figure 1.6). Inverting the direction of the motion changes the signs of $\dot{y}$ and $\dot{\psi}$, again, thus,

$$f_y(y, -\psi) = -f_y(y, \psi), \qquad f_\psi(y, -\psi) = f_\psi(y, \psi). \tag{1.26}$$

Symmetry properties (1.25) and (1.26) have important consequences. The evaluation of (1.25)-(1.26) at $y = \psi = 0$ leads to $f_y(0, 0) = 0$ and $f_\psi(0, 0) = 0$. Hence, the trivial

solution of (1.23) can be written in the form

$$\begin{aligned} y(t) &\equiv 0, \\ \psi(t) &\equiv 0, \\ \varphi(t) &= \varphi_0 + f_\varphi(0,0) \cdot t, \\ w(t) &= w_0 + vt. \end{aligned} \tag{1.27}$$

In this case, the wheelset remains in the central position ($y = 0, \psi = 0$), and by starting from the initial state φ_0 and w_0, the wheelset is rolling along the track without the presence of kinematic oscillations. When dynamics of the equations (1.23) is perturbed from the stationary rolling (1.27), we get the effect of kinematic oscillation.

By restricting the dynamics to the phase plane (y, ψ) of the reduced system, the stationary rolling (1.27) becomes the equilibrium point $y = \psi = 0$. The kinematic oscillations correspond to trajectories around this equilibrium point. The odd and even properties (1.25) and (1.26) provide symmetries in the phase plane: the phase portrait is symmetric with respect to the reflection about the lines $y = 0$ and $\psi = 0$. In this case, if the equilibrium $y = \psi = 0$ is found to be a centre then there is a neighbourhood of the equilibrium where *all* trajectories are periodic (see see [65] p. 164). *That is, the kinematic motion of the wheelset is neutrally stable also for finite amplitude oscillations.*

1.4.2 Linear oscillations

By considering the symmetries (1.25)-(1.26), the first-order Taylor expansion of (1.24) results in

$$\begin{aligned} \dot{y} &= a_{01}\psi + O^3(y,\psi), \\ \dot{\psi} &= b_{10}y + O^3(y,\psi), \end{aligned} \tag{1.28}$$

where

$$a_{ij} = \frac{\partial f_y}{\partial \psi}(0,0), \qquad b_{ij} = \frac{\partial f_\psi}{\partial y}(0,0), \tag{1.29}$$

and $O^n(y,\psi)$ denotes the n^{th} or higher order terms. If we expect $a_{01} \cdot b_{10} < 0$ then the system (1.28) can be transformed into the single second-order differential equation

$$\ddot{y} + \omega_L^2 y + O^3(y,\dot{y}) = 0, \tag{1.30}$$

where

$$\omega_L := \sqrt{-a_{01}b_{10}} \tag{1.31}$$

is the angular frequency of the linear (small amplitude) oscillations.

1.4.3 Nonlinear oscillations

Let us continue the Taylor expansion (1.28) up to the third order terms. By considering the symmetries (1.25)-(1.26), we get

$$\begin{aligned} \dot{y} &= a_{01}\psi + a_{03}\psi^3 + a_{21}y^2\psi + O^5(y,\psi), \\ \dot{\psi} &= b_{10}y + b_{30}y^3 + b_{12}y\psi^2 + O^5(y,\psi), \end{aligned} \tag{1.32}$$

where

$$a_{ij} = \frac{1}{i!j!}\frac{\partial^{i+j} f_y}{\partial y^i \partial \psi^j}(0,0), \qquad b_{ij} = \frac{1}{i!j!}\frac{\partial^{i+j} f_\psi}{\partial y^i \partial \psi^j}(0,0). \tag{1.33}$$

The system (1.32) can be also expressed as a single second-order differential equation,

$$\ddot{y} + \omega_L^2 y + c_{03}y^3 + c_{21}y\dot{y}^2 + O^5(y,\dot{y}) = 0, \tag{1.34}$$

where the formulae

$$c_{03} = -a_{01}b_{30} - a_{21}b_{10}, \qquad c_{21} = -\frac{a_{01}b_{12} + 2a_{01}a_{21} + 3a_{03}b_{10}}{a_{01}^2} \tag{1.35}$$

for the constants are obtained by direct calculation from (1.32). Note that the dependence on $\dot{y}$ was missing from the differential equation (1.4). This shows the deficiency of the classical approximate derivation from the rolling radius difference.

To determine the angular frequency of the system, let us apply the transformation

$$\begin{aligned} y^*(y,\psi) &= y \cdot \left(1 + A_{20}y^2 + A_{02}\psi^2 + O^4(y,\psi)\right), \\ \psi^*(y,\psi) &= \psi \cdot \left(B_{00} + B_{20}y^2 + B_{02}\psi^2 + O^4(y,\psi)\right). \end{aligned} \tag{1.36}$$

By the appropriately chosen constants of (1.36), the system (1.32) can be put into the form

$$\begin{bmatrix} \dot{y}^* \\ \dot{\psi}^* \end{bmatrix} = \left(\begin{bmatrix} 0 & \omega_L \\ -\omega_L & 0 \end{bmatrix} + \left(y^{*2} + \psi^{*2}\right) \begin{bmatrix} 0 & \beta\omega_L \\ -\beta\omega_L & 0 \end{bmatrix} + O^2(y^{*2} + \psi^{*2}) \right) \cdot \begin{bmatrix} y^* \\ \psi^* \end{bmatrix}. \tag{1.37}$$

The angular frequency ω_L of small oscillations was defined in (1.31), and it can be shown by direct calculation that the formula for the parameter β becomes

$$\beta := \frac{1}{8} \cdot \left(\frac{3b_{30}}{b_{10}} + \frac{a_{21}}{a_{01}} - \frac{b_{12}}{a_{01}} - \frac{3a_{03}b_{10}}{a_{01}^2} \right). \tag{1.38}$$

The structure of the system (1.37) has a structure similar to that of the normal form of the Hopf bifurcation (see [29] p. 152 or [73] p. 385), but the main diagonal of the second matrix of (1.37) is empty due to the neutral stability of the system.

Let us perform a further transformation by replacing y^* and ψ^* by polar coordinates. That is, let us define

$$\rho := \sqrt{y^{*2} + \psi^{*2}}, \qquad \tan\varepsilon := \frac{\psi^*}{y^*}, \tag{1.39}$$

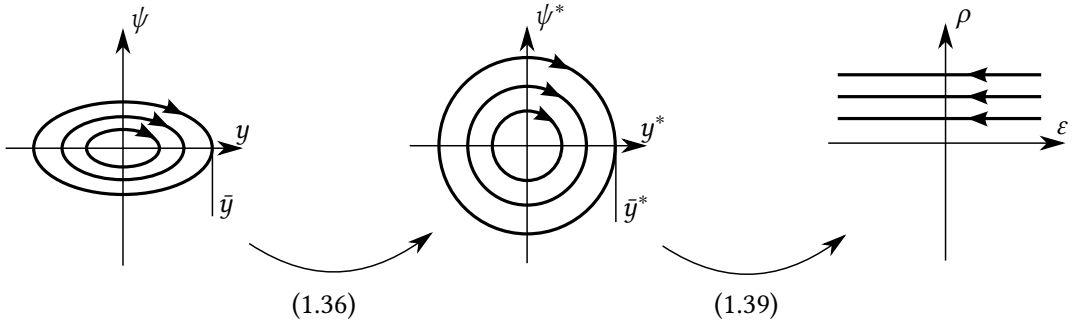

Figure 1.7: The sketch of the transformations (1.36) and (1.39). Left panel: phase plane of (1.32). Middle panel: phase plane of (1.37). Right panel: phase plane of (1.40). The transformation from (y, ψ) to (y^*, ψ^*) is a *near-identity transformation* with respect to y, because $y \approx y^*$ in linear approximation. The transformation into polar coordinates causes that the equilibrium $y = \psi = 0$ of (1.32) corresponds to the line $\rho = 0$ in (1.40).

where ρ is related to the amplitude of the oscillation and ε is related to the phase angle of the oscillation (see Figure 1.7). Then, (1.37) becomes

$$\dot{\rho} = 0 + O^5(\rho), \qquad \dot{\epsilon} = -\omega_L \cdot \left(1 + \beta\rho^2 + O^4(\rho)\right), \tag{1.40}$$

The first equation shows that the amplitude ρ of the oscillations in (1.37) is constant even by considering the third-order terms. The absolute value of the time derivative $\dot{\epsilon}$ gives the *nonlinear* angular frequency ω_N of the oscillation. By linear approximation, the amplitude $\bar{y}$ in the original variable can be expressed by $\rho \approx \bar{y}^* \approx \bar{y}$, that is, the formula for the angular frequency becomes

$$\omega_N(\bar{y}) = \omega_L \cdot \left(1 + \beta\bar{y}^2 + O^4(\bar{y})\right). \tag{1.41}$$

This formula can also be derived from (1.34) by the method of harmonic balance (see [39], p. 138), which is presented here only concisely. Let us approximate the solutions by

$$y(t) \approx \bar{y} \cdot \cos\left(\omega_N(\bar{y}) \cdot t\right), \tag{1.42}$$

and let us substitute it into (1.34). By Fourier expansion of the resulting expression and by neglecting the terms of the higher frequencies, we get

$$\omega_N(\bar{y}) \approx \sqrt{\frac{4\omega_L^2 + 3c_{03}\bar{y}^2}{4 - c_{21}\bar{y}^2}} = \omega_L \cdot \left(1 + \left(\frac{c_{21}}{8} + \frac{3c_{03}}{8\omega_L^2}\right)\bar{y}^2 + O^4(\bar{y})\right). \tag{1.43}$$

It can be checked from (1.31) and (1.35) that (1.43) gives the same formula as (1.41) with the nonlinearity factor (1.38).

The formula (1.41) gives the angular frequency for oscillations with a finite amplitude $\bar{y}$. Let us call β the *nonlinearity factor* of the system, which expresses the effect of the amplitude on the angular frequency of the oscillations. If $\beta > 0$ then the

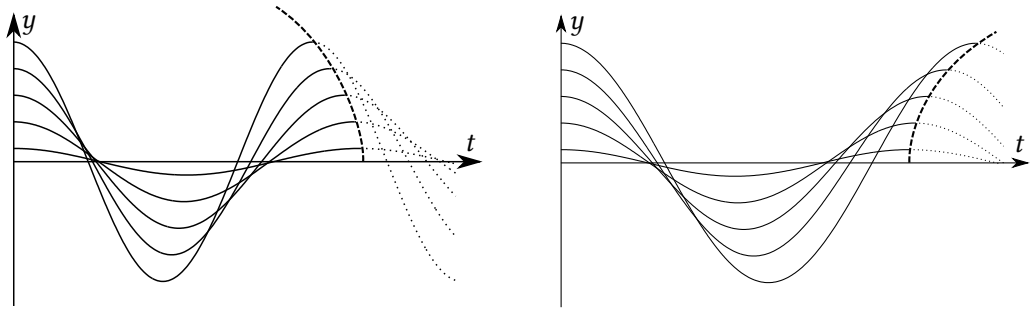

Figure 1.8: The effect on the amplitude on the frequency of the kinematic oscillations. Left panel: $\beta > 0$, the frequency is increasing with the increasing amplitude. Right panel: $\beta < 0$, the frequency is decreasing with the increasing amplitude. A period of oscillation is denoted by continuous lines. The dashed line denotes the parabolic relation (1.44) between the wavelenght (time period) and amplitude.

frequency is *increasing* with the increasing amplitude (see Figure 1.8), and if $\beta < 0$ then the frequency is *decreasing* with the increasing amplitude. These tendencies are valid by assuming *weakly nonlinear approximation*, that is, by considering the amplitude range where the fifth and higher order terms can be neglected in (1.32). Then, the difference between the linear and nonlinear angular frequencies can be approximated by $\omega_N(\bar{y}) - \omega_L \approx \beta\omega_L\bar{y}^2$. That is, the difference is proportional to the square of the amplitude.

From the formula (1.41), we can get expressions also for the wavelength of the oscillation and the equivalent conicity of the system. The wavelength $\lambda(\bar{y})$ for finite amplitude oscillations can be calculated by

$$\lambda_N(\bar{y}) = \frac{2\pi v}{\omega_N(\bar{y})} = \frac{2\pi v}{\omega_L\left(1 + \beta\bar{y}^2 + O^4(\bar{y})\right)} = \lambda_L \cdot \left(1 - \beta\bar{y}^2 + O^4(\bar{y})\right), \tag{1.44}$$

where $\lambda_L = 2\pi v/\omega_L$ is the wavelength for small oscillations. Based on (1.12), the equivalent conicity can be expressed as

$$h_N^*(\bar{y}) = \frac{br}{v^2}\omega_N(\bar{y})^2 = h_L^* \cdot \left(1 + 2\beta\bar{y}^2 + O^4(\bar{y})\right), \tag{1.45}$$

where h_L^* is the equivalent conicity for small oscillations.

Example 1.1. (Nonlinearity factor from numerical data) In this example, the form of (1.44) is validated by the numerical results of Schwab and Meijaard [52]. In Figures 7-8. in [52], the oscillation of the wheelset is plotted against the distance for several amplitudes, which result was obtained by numerical simulation for two different geometries. From these figures, the wavelength of the oscillation can be determined, which is plotted in Figure 1.9 by dots. In both cases, the formula (1.44) can be fitted nicely to the first four data points (see the continuous line in Figure 1.9), and we get the nonlinearity factors $\beta = 0.12$ 1/mm^2 and $\beta = 0.0021$ 1/mm^2, respectively. The deviation of the

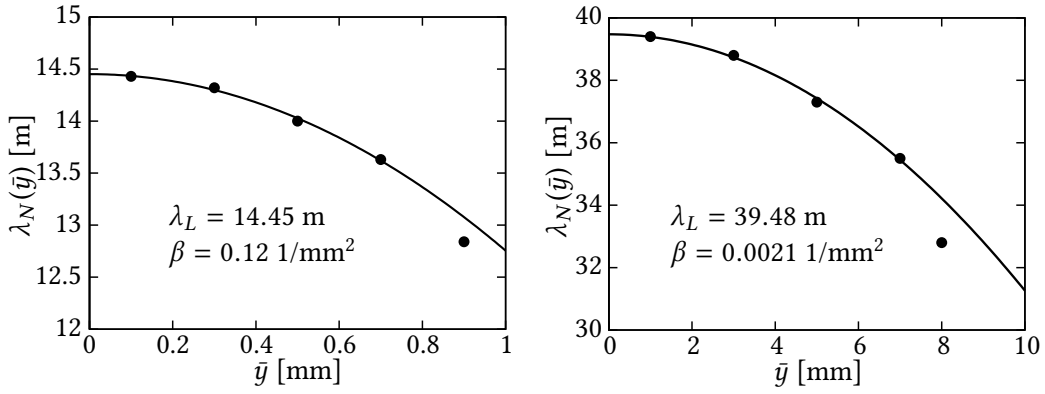

Figure 1.9: The fitting of (1.44) to the numerical results of Schwab and Meijaard [52]. Left panel: the data points are from Figure 7 of [52]. Right panel: the data points are from Figure 8 of [52].

last data points from the fitted curves is probably caused by the higher-order terms in (1.44).

1.5 Determining parameters from the geometry

The application of (1.41) to a given rail and wheel profile requires the values of the linear angular frequency ω_L and the nonlinearity factor β. In this section, analytic formulae of these parameters are determined from the geometry of the profile curves.

1.5.1 Unfolding of the constraints

After performing the calculations, the geometric constraint (1.17) leads to

$$\begin{aligned} -(V_r^\pm - w) + (c_w(U_w^\pm) - r)\cos\psi\sin(V_w^\pm - \varphi) \mp (U_w^\pm + b)\sin\psi = 0,\\ y + \Big((c_w(U_w^\pm) - r)\sin\psi\sin(V_w^\pm - \varphi) \pm (U_w^\pm + b)\cos\psi\Big)\cos\vartheta\\ - (c_w(U_w^\pm) - r)\sin\vartheta\cos(V_w^\pm - \varphi) \mp (U_r^\pm + b) = 0,\\ z + \Big((c_w(U_w^\pm) - r)\sin\psi\sin(V_w^\pm - \varphi) \pm (U_w^\pm + b)\cos\psi\Big)\sin\vartheta\\ + (c_w(U_w^\pm) - r)\cos\vartheta\cos(V_w^\pm - \varphi) - c_r(U_r^\pm) + r = 0, \end{aligned} \tag{1.46}$$

and (1.18) becomes

$$\begin{aligned} c_w'(U_w^\pm)\tan\psi \pm \sin(V_w^\pm - \varphi) = 0,\\ c_w'(U_w^\pm)\,(c_r'(U_r^\pm)\tan\vartheta \pm 1) + \cos(V_w^\pm - \varphi)\cos\psi\,(\tan\vartheta \mp c_r'(U_r^\pm)) = 0. \end{aligned} \tag{1.47}$$

It can be checked that in the central position $q = q_0 = [0, 0, \varphi, w]$, the trivial solution $\hat{q} = [0, 0, 0, 0, w, w, 0, 0, \varphi, \varphi]$ for the dependent variables satisfies (1.51). In the nontrivial case, the dependent variables cannot be expressed explicitly, except for some special geometries (see [12]).

The four independent components of (1.21)-(1.22) can be expressed in the form

$$\begin{aligned}
(W^+Z^- - W^-Z^+)\cdot\dot{w} + (Y^+Z^- - Y^-Z^+)\cdot\dot{y} &= 0,\\
\Big(-(Y^+ - Y^-)\cdot\sin\vartheta + (Z^+ - Z^-)\cdot\cos\vartheta\Big)\cdot\dot{w} + (Y^+Z^- - Y^-Z^+)\cdot\dot{\psi} &= 0,\\
\Big((Z^+ - Z^-)\cdot\sin\vartheta + (Y^+ - Y^-)\cdot\cos\vartheta\Big)\cdot\dot{w} + (Y^+Z^- - Y^-Z^+)\cdot\cos\psi\cdot\dot{\varphi} &= 0,\\
\dot{w} - v &= 0,
\end{aligned} \tag{1.48}$$

where

$$\begin{bmatrix} W^\pm \\ Y^\pm \\ Z^\pm \end{bmatrix} = \begin{bmatrix} 1 & 0 & 0 \\ 0 & \cos\vartheta & -\sin\vartheta \\ 0 & \sin\vartheta & \cos\vartheta \end{bmatrix} \cdot \begin{bmatrix} \cos\psi & -\sin\psi & 0 \\ \sin\psi & \cos\psi & 0 \\ 0 & 0 & 1 \end{bmatrix} \cdot \mathbf{f}_w^\pm(U_w^\pm, V_w^\pm - \varphi) \tag{1.49}$$

is a shorthand notation for the location of the contact points. From (1.48), we can express

$$\begin{aligned}
\dot{y} &= \tilde{f}_y(\psi, \vartheta, \varphi, U_w^\pm, V_w^\pm) = \frac{Z^+W^- - Z^-W^+}{Y^+Z^- - Y^-Z^+},\\
\dot{\psi} &= \tilde{f}_\psi(\psi, \vartheta, \varphi, U_w^\pm, V_w^\pm) = \frac{(Y^+ - Y^-)\cdot\sin\vartheta - (Z^+ - Z^-)\cdot\cos\vartheta}{Y^+Z^- - Y^-Z^+}.
\end{aligned} \tag{1.50}$$

As the geometric constraints (1.46)-(1.47) cannot be expressed in an explicit form, transformation of (1.50) cannot be carried out into the full nonlinear form of $f_y(y,\psi)$ and $f_\psi(y,\psi)$. However, implicit differentiation can be used to expand the constraints into Taylor series in the form (1.28) or (1.32).

1.5.2 Angular frequency of linear oscillations

The geometric constraints (1.46)-(1.47) can be written into the form

$$g_i\,(q, \hat{q}) = 0, \quad i = 1 \ldots 10. \tag{1.51}$$

By taking the total derivative of (1.17) with respect to the general coordinate q_k, we get

$$\left(\frac{\partial g_i}{\partial q_k} + \sum_{j=1}^{10} \frac{\partial g_i}{\partial \hat{q}_j}\cdot\frac{\partial \hat{q}_j}{\partial q_k}\right)\mathrm{d}q_k \equiv 0. \tag{1.52}$$

From these equations, the partial derivatives $\partial\hat{q}_j/\partial q_k$ of the dependent variables can be expressed. Then, the first-order Taylor expansion of the dependent variables becomes

$$\begin{aligned}
\vartheta(y,\psi) &= \frac{h}{b-hr}\cdot y && +\mathcal{O}^2(y,\psi),\\
z(y,\psi) &= 0 && +\mathcal{O}^2(y,\psi),\\
U_r^{\pm}(y,\psi) &= \mp\frac{R_r\left(b+R_w\frac{h}{\sqrt{1+h^2}}\right)}{(b-hr)(R_w-R_r)}\cdot y && +\mathcal{O}^2(y,\psi),\\
V_r(y,\psi,w) &= w\mp(b-hr)\cdot\psi && +\mathcal{O}^2(y,\psi),\\
U_w^{\pm}(y,\psi) &= \mp\frac{R_w\left(b+R_r\frac{h}{\sqrt{1+h^2}}\right)}{(b-hr)(R_w-R_r)}\cdot y && +\mathcal{O}^2(y,\psi),\\
V_w^{\pm}(y,\psi,\varphi) &= \varphi\mp h\psi && +\mathcal{O}^2(y,\psi),
\end{aligned} \tag{1.53}$$

where R_w and R_r are the nominal radii of curvature of the wheel and rail profiles, respectively (see Figure 1.5). In the derivation of (1.53), it is taken into consideration that

$$c_r(0)=c_w(0)=0, \qquad c_r'(0)=c_w'(0)=h, \tag{1.54}$$

and that the radii of curvature and the second derivatives of the profile curves are related through

$$c_r''(0)=-\frac{\left(\sqrt{1+h^2}\right)^3}{R_r}, \qquad c_w''(0)=-\frac{\left(\sqrt{1+h^2}\right)^3}{R_w}. \tag{1.55}$$

By substituting (1.53) into (1.50) and by calculating the linear coefficients of (1.28), we get

$$a_{01}=v\cdot\frac{b-hr}{b}, \qquad b_{10}=-v\cdot\frac{hR_w\left(b+R_r\frac{h}{\sqrt{1+h^2}}\right)}{br(b-hr)(R_w-R_r)}, \tag{1.56}$$

thus, the linear angular frequency (1.31) becomes

$$\omega_L=v\sqrt{\frac{h}{br}\cdot\frac{R_w}{R_w-R_r}\cdot\left(1+\frac{R_rh}{b\sqrt{1+h^2}}\right)}. \tag{1.57}$$

This is the same formula as the formula (1.10) of Meijaard. That is, the formula of Meijaard cannot be further improved and it is valid for any differentiable profile curves on a straight track. The present analysis lets the angular frequency ω_L to depend on the *change* of the radius of the curvature, as well, but (1.57) shows that this effect does not modify the angular frequency. The formulae (1.7)-(1.9) can be obtained by the assumption of the small conicity h in the sense $hR_r \ll b$ and $h^2 \ll 1$.

1.5.3 Angular frequency of nonlinear oscillations

By taking the second total derivative of (1.51), we get

$$\left(\frac{\partial^2 g_i}{\partial q_k \partial q_l} + \sum_{j=1}^{10}\left(\frac{\partial^2 g_i}{\partial \hat{q}_j \partial q_l} + \sum_{m=1}^{10}\frac{\partial^2 g_i}{\partial \hat{q}_j \partial \hat{q}_m}\cdot\frac{\partial \hat{q}_m}{\partial q_l}\right)\cdot\frac{\partial \hat{q}_j}{\partial q_k} + \sum_{j=1}^{10}\frac{\partial g_i}{\partial \hat{q}_j}\cdot\frac{\partial^2 \hat{q}_j}{\partial q_k \partial q_l}\right)\mathrm{d}q_k\mathrm{d}q_l \equiv 0, \quad (1.58)$$

and the process can be continued further to the third derivatives. From these equations, we can get the second and third partial derivatives of the dependent variables $\hat{q}$ with respect to the generalised coordinates q. At this point, the analytical calculations become so complicated that it is cumbersome to follow them by hand. Thus, the computer algebra system Maxima was used for the subsequent calculations.

The steps are similar to those of the linear calculations. First, the second and third derivatives of the dependent variables are expressed. Then, the Taylor series expansion (1.53) can be continued up to the third order terms, and it is used for determining the parameters of (1.32) from (1.50). Finally, the nonlinearity factor β is calculated by (1.38).

The resulting full formula for β can be obtained by computer algebra, but it gives an unacceptably long expression. Instead of that, we can consider the *approximate* formula when the conicity h is small in the sense

$$hr \ll b, \qquad hb \ll r, \qquad h^2 \ll 1, \qquad hR_r \ll b, \qquad hR_w \ll b. \quad (1.59)$$

From (1.55), the higher order derivatives of the wheel profile are approximated by

$$\begin{aligned} c_w''(0) &\approx -1/R_w, \\ c_w'''(0) &\approx (R_w' + 3h)/R_w^2, \\ c_w''''(0) &\approx (R_w'' R_w - 2(R_w')^2 - 3)/R_w^2 \end{aligned} \quad (1.60)$$

at the nominal contact point, where R_w' and R_w'' denote the derivatives of the radius of curvature with respect to the axial coordinate U_w. By using a similar notation for the rail profile, the calculations lead to

$$\beta \approx \frac{3r - 4R_w}{16r(R_w - R_r)^2} + \frac{R_w'(R_w - R_r) + 3R_r(R_w' - R_r')}{16h(R_w - R_r)^3} - \frac{R_r(R_w'' R_w - R_r'' R_r)}{16(R_w - R_r)^3}. \quad (1.61)$$

That is, the nonlinearity factor is affected by the wheel and rail profiles up to the *fourth* derivatives of the profile curves, which is related to the second derivatives of the radii of curvature.

Let us consider two special cases of (1.38). For profiles with *constant* curvature, we have $R_w' = R_w'' = R_r' = R_r'' = 0$, and (1.38) becomes

$$\beta \approx \frac{3r - 4R_w}{16r(R_w - R_r)^2}. \quad (1.62)$$

b	r	h	R_w	R'_w	R_r	R'_r	v
0.7 m	0.4 m	0.05	0.5 m	30	0.25 m	0	50 m/s

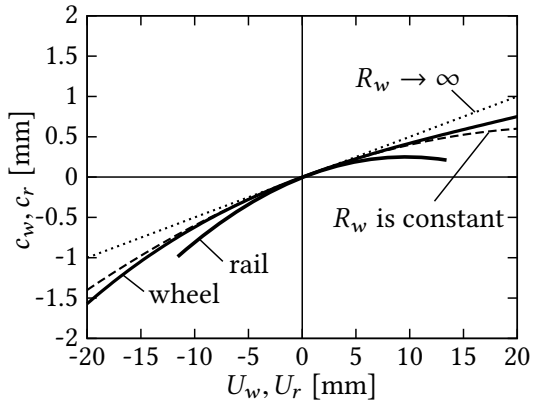

linear frequency ($\bar{y} = 0$)		
Klingel	Heumann	Meijaard
3.363 Hz	4.756 Hz	4.798 Hz

	$\bar{y} = 0$	$\bar{y} = 10$ mm
constant R_w	4.798 Hz	4.797 Hz
varying R_w	4.798 Hz	5.949 Hz

Figure 1.10: The data and the results of Example 1.2. The graph in the middle: the rail and the wheel profiles at the nominal contact point. The constant curvature approximation is denoted by a dashed line (R_w is constant), and the conical approximation is denoted by a dotted line ($R_w \to \infty$). Top table: the parameters of the system. Middle table: the frequency of the small amplitude oscillations according to formulae (1.7),(1.8),(1.10) and (1.57). Bottom table: the change of the frequency for finite amplitudes according to formulae (1.62) and (1.64).

The formula shows that if the profiles are nearly conformal ($R_w \approx R_r$) then not only the linear angular frequency (1.57) becomes high but β increases, too; thus, the angular frequency becomes sensitive to the amplitude of the oscillations. If the profiles are far from being conformal (values of R_w and R_r are far from each other) then the effect of the amplitude is relatively small because in practice, the amplitude $\bar{y}$ is in the range of a few millimetres.

If the curvatures of the profiles are *changing* at the nominal contact point, and the conicity h is small in the sense

$$hr \ll R'_w, \qquad hr \ll R'_r, \qquad hR''_w r \ll R'_r, \qquad hR''_r r \ll R'_r \tag{1.63}$$

then the second term of (1.61) becomes dominant and we get

$$\beta \approx \frac{R'_w(R_w - R_r) + 3R_r(R'_w - R'_r)}{16h(R_w - R_r)^3}. \tag{1.64}$$

The formula shows that if the derivatives R'_r and R'_w of the radii of curvature are not negligible then the nonlinearity factor β can be very large due to the small value of the conicity h in the numerator. That is, the effect of the amplitude on the angular frequency is significant even in the case when R_w and R_r are far from each other.

Example 1.2 (Calculation of the nonlinearity factor from the geometry)**.** The effect of the varying curvature is demonstrated on a numerical example (see Figure 1.10). It is assumed that the rail profile has a constant radius R_r of curvature, but the radius of

curvature of the wheel profile is varying (given by R_w and R'_w). The chosen parameter values in Figure 1.10 are from the physically realistic range. Formulae (1.10) and (1.57) show that the angular frequency for small amplitudes is $\omega_L = 30.15$ 1/s, that is, the frequency is 4.798 Hz. If the variation of the profile is neglected ($R'_w \to 0$) then the nonlinearity factor becomes $\beta \approx -2.0 \cdot 10^{-6}$ 1/mm^2. Then, for the amplitude $\bar{y} = 10$ mm, the frequency changes by only 0.2 per cent. However, by considering the value $R'_w \neq 0$, the nonlinearity factor becomes $\beta \approx 2.4 \cdot 10^{-3}$ 1/mm^2. In this case, the same amplitude $\bar{y} = 10$ mm modifies the frequency by 25 per cent. This example demonstrates that the variation of the curvature can lead to a significant change in the frequency of the kinematic oscillations.

1.6 New results

Thesis Statement 1. Consider the model of a railway vehicle running with a constant speed v along a straight track, where the dynamics of one of its wheelsets is described by the lateral displacement y and the yaw angle ψ. Rolling is assumed between the wheelset and each rail.

i) The nonlinear dynamics of the kinematic oscillations of the wheelset is described by differential equations in the form

$$\dot{y} = a_{01}\psi + a_{03}\psi^3 + a_{21}y^2\psi + O^5(y,\psi),$$
$$\dot{\psi} = b_{10}y + b_{30}y^3 + b_{12}y\psi^2 + O^5(y,\psi),$$

where $O^n()$ denotes the n^{th} or higher order terms, and the coefficients a_{ij} and b_{ij} are determined by the geometry of the surfaces and the speed v of the vehicle.

ii) For a finite amplitude $\bar{y}$ of the kinematic oscillation, the angular frequency is given by

$$\omega_N(\bar{y}) = \omega_L \cdot \left(1 + \beta\bar{y}^2 + O^4(\bar{y})\right),$$

where $\omega_L = \sqrt{-a_{01}b_{10}}$ is the angular frequency of small-amplitude oscillations and β is the nonlinearity factor determined by

$$\beta = \frac{1}{8}\left(\frac{3b_{30}}{b_{10}} + \frac{a_{21}}{a_{01}} - \frac{b_{12}}{a_{01}} - \frac{3a_{03}b_{10}}{a_{01}^2}\right).$$

The distance between the contact points is b, the nominal rolling radius of the wheelset is r, the conicity of the wheelset is h. The radii of curvatures of the wheel

and rail profiles are denoted by R_w and R_r, respectively, and their variations along the axis of the wheelset are described by the derivatives R'_w,R''_w, ... and R'_r,R''_r, ...

iii) The angular frequency of the small-amplitude kinematic oscillations is given by

$$\omega_L = v\sqrt{\frac{h}{br}\cdot\frac{R_w}{R_w - R_r}\cdot\left(1+\frac{R_r h}{b\sqrt{1+h^2}}\right)}.$$

Therefore, the formula of Meijaard is valid also for profiles with varying curvature.

iv) The nonlinearity factor β is determined by the wheel and rail profiles up to the second derivatives of the radii of curvatures. For small conicity h of the wheelset, the approximate value of the nonlinearity factor is

$$\beta \approx \frac{R'_w(R_w - R_r) + 3R_r(R'_w - R'_r)}{16h(R_w - R_r)^3}.$$

The small value h in the denominator of the formula shows that the variation of the curvature of the profiles has a significant effect on the change of the angular frequency for increasing amplitudes.

Related publications: [2], [4], [9], [12].

Chapter 2

Codimension–2 extension of Filippov systems

2.1 Introduction

The theory of *Filippov systems* provides useful mathematical tools when analysing mechanical systems with discontinuities. In a Filippov system, the m dimensional phase space of the dynamics is separated into regions by $m-1$ dimensional surfaces. Inside each region, the dynamics is described by a smooth vector field, while the vector field has a discontinuity at the boundary surfaces.

A concept of such systems was established in the book of Filippov [23], and many results and methods has been developed in the following decades. A throughout overview of the topic with a large number of references can be found in the book of di Bernardo and his co-authors [19].

One of the oldest and most frequent application of Filippov systems is modelling of mechanical systems with Coulomb friction. In case of the two-dimensional contact of two rigid bodies, the tangential contact force has a jump when the direction of the relative velocity at the contact point changes sign during the motion. This effect leads to a Filippov system where the discontinuity surface corresponds to the state where the relative velocity is zero at the contact points of the bodies.

However, when we consider the three-dimensional contact of two rigid bodies, the Coulomb friction becomes discontinuous only when both components of the relative velocity at the contact point becomes zero *at the same time*. This results an $m-2$ dimensional discontinuity manifold in the phase space of the system, which is out of scope of Filippov systems.

The main motivation of this chapter is the following: *How can we extend Filippov systems to include spatial Coulomb friction to the analysis?* The analysis of Filippov systems can be applied for $m-1$ dimensional (codimension-1) discontinuity manifolds, while we require methods for $m-2$ dimensional (codimension-2) discontinuity manifolds. The main ideas of this chapter can be found in a paper of the candidate [11].

	Notation	Filippov systems	extended Filippov systems
discontinuity set	$\mathcal{D} \subset \mathbb{R}^m$	domain of the differential equation	
	Σ	codimension-1 discontinuity manifold	codimension-2 discontinuity manifold
	$H(x)$	function for implicit form of Σ	
	$H_{(1)}(x), H_{(2)}(x)$		functions for implicit form of Σ
	$i \in \{1, 2\}$	indices of two sides of Σ	
	$\phi \in [0, 2\pi)$		direction angle around Σ
	$n_i(x_0)$	unit vector normal to Σ at x_0	
	$n(\phi)(x_0)$		unit vector normal to Σ at x_0
	$n_{(1)}(x_0), n_{(2)}(x_0)$		basis for generating $n(\phi)(x_0)$
discontinuous dynamics	$F(x)$	vector field of the system	
	$F_i^*(x_0) = F_i(x_0)$	limit vector at x_0 from the direction of $n_i(x_0)$	
	$F^*(\phi)(x_0)$		limit vector at x_0 from the direction of $n(\phi)(x_0)$
	$R(\phi)$		component of $F^*(\phi)$ in the direction of $n(\phi)$
	$V(\phi)$		component of $F^*(\phi)$ normal to both Σ and $n(\phi)$
	$\Sigma_{sl}, \Sigma_{cr} \subset \Sigma$	sliding and crossing regions	
sliding	$F_s(x_0)$	sliding vector at x_0	
	$\alpha_i(x_0)$	weight of F_i for the sliding vector at x_0	
	$\alpha(\phi)(x_0)$		weight function for the sliding vector at x_0
	$\overline{F}, F_A, F_B, A(\phi), B(\phi)$		quantities for expressing $F^*(\phi)$ in case of unique sliding
	a, b		weights for expressing F_s from F_A and F_B

Table 2.1: Important notations of Chapter 2. The two columns show the similarities and differences between the concepts of Filippov systems and those of extended Filippov systems.

It is important to distinguish this extension from the case of the intersection of two codimension-1 manifolds in Filippov systems (see [19], p. 404 or [20] and [36] for the most recent results). A possible source of those systems can arise when two planar contact pairs are presented in a mechanical system.

Note that discontinuous dynamics of Coulomb friction can be investigated from a fully different viewpoint of *complementary problems* (see Chapter 10 of [25]). A further approach can be found in [15].

The structure of the chapter is the following: Section 2.2 gives an overview of Filippov systems, and it is organised to establish the necessary basis for extension to the codimension-2 case. The main part of the chapter is Section 2.3, where the fundamental concepts of Filippov systems are extended to codimension-2 discontinuity sets, which results to the theory of *extended Filippov systems.* In Section 2.4, the theory is demonstrated on a mechanical problem. The new results are summarised in Section 2.5.

2.2 Overview of Filippov systems

In this section, an overview of Filippov systems is provided. Sections 2.2 and 2.3 are organised in a similar way to help to follow the extension of the concepts. The most important notations can be found in Table 2.1.

2.2.1 Definition of Filippov systems

Consider a domain $\mathcal{D} \subset \mathbb{R}^m$ and an $m-1$ dimensional smooth manifold $\Sigma \subset \mathcal{D}$. The manifold Σ can be defined as the zero set of a smooth function $H : \mathcal{D} \to \mathbb{R}$ by

$$\Sigma := \{x \in \mathcal{D} : H(x) = 0\}\,. \tag{2.1}$$

This manifold Σ separates the domain $\mathcal{D}$ into two regions,

$$S_1 := \{x \in \mathcal{D} : H(x) > 0\}\,, \qquad S_2 := \{x \in \mathcal{D} : H(x) < 0\}\,, \tag{2.2}$$

and hence, we have $\Sigma \cup S_1 \cup S_2 = \mathcal{D}$. With these notations, we can define the concept of a Filippov system:

Definition 2.1 (Filippov system)**.** *Consider the sets* (2.1)-(2.2) *and the ordinary differential equation*

$$\dot{x} = F(x) \tag{2.3}$$

in the form

$$F(x) = \begin{cases} F_1(x), & x \in S_1 \\ F_2(x), & x \in S_2 \end{cases}, \tag{2.4}$$

where F_1 and F_2 are smooth functions on $S_1 \cup \Sigma$ and $S_2 \cup \Sigma$, respectively. Suppose that for any $x_0 \in \Sigma$, $F_1(x_0) \neq F_2(x_0)$ is satisfied. Then, (2.3) *is called a* ***Filippov system****.*

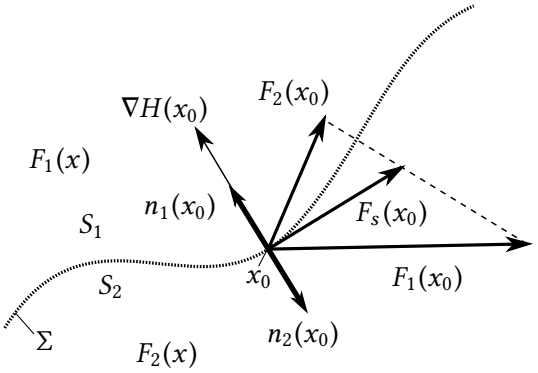

Figure 2.2: Basic concepts of Filippov systems depicted in the phase space of the system.

The set Σ is called the *discontinuity manifold* or *switching manifold* of the system. This manifold separates the phase space into two regions with dynamics described by F_1 and F_2 (see Figure 2.2). The condition $F_1(x_0) \neq F_2(x_0)$ at the discontinuity is called the *uniform degree 1 of smoothness* of the system (see [19], p. 75).

Note that a more general definition of Filippov systems can be found in the literature, where there are more discontinuity manifolds in the phase space (see [19], p. 73). However, the restriction of Definition 2.1 to a single discontinuity manifold is sufficient for the analysis of the present work.

If we require that the gradient $\nabla H(x_0)$ is nonzero for any point $x_0 \in \Sigma$, then

$$n_1(x_0) := \frac{\nabla H(x_0)}{\|\nabla H(x_0)\|}, \qquad n_2(x_0) := -n_1(x_0). \tag{2.5}$$

give the two unit vectors which are normal to Σ at x_0. The symbol $\|.\|$ is used for the usual 2-norm of a vector. Definition 2.1 implicitly includes that the limits of F exist from both sides of Σ, that is,

$$\begin{aligned} F_1^*(x_0) &:= \lim_{\epsilon \to 0^+} F\Big(x_0 + \epsilon n_1(x_0)\Big) = F_1(x_0), \\ F_2^*(x_0) &:= \lim_{\epsilon \to 0^+} F\Big(x_0 + \epsilon n_2(x_0)\Big) = F_2(x_0). \end{aligned} \tag{2.6}$$

2.2.2 Definition of sliding and crossing regions

The discontinuity manifold Σ has two typical regions (see Figure 2.3):

Definition 2.2 (Sliding region)**.** *The subset $\Sigma_{sl} \subset \Sigma$ satisfying*

$$\langle F_1, n_1 \rangle (x_0) \cdot \langle F_2, n_2 \rangle (x_0) > 0 \tag{2.7}$$

*for any $x_0 \in \Sigma_{sl}$ is called the **sliding region** of Σ.*

Definition 2.3 (Crossing region)**.** *The subset $\Sigma_{cr} \subset \Sigma$ satisfying*

$$\langle F_1, n_1 \rangle (x_0) \cdot \langle F_2, n_2 \rangle (x_0) < 0 \tag{2.8}$$

*for any $x_0 \in \Sigma_{cr}$ is called the **crossing region** of Σ.*

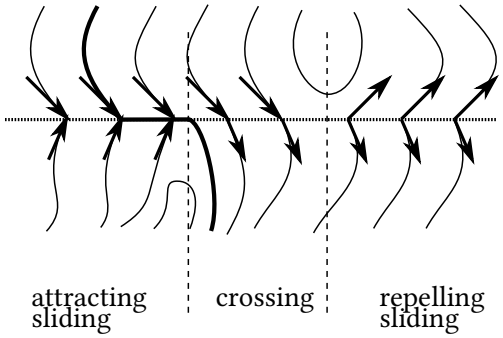

Figure 2.3: Crossing and sliding regions in the phase space of a Filippov system. The arrows denote the vector field at the discontinuity set, and the thin lines denote some typical trajectories. The thick line shows a trajectory which reaches the discontinuity set Σ in the attracting sliding region. Then, the trajectory evolves inside Σ until it reaches the tangency point at the boundary of the sliding and crossing regions. Then, the trajectory leaves the discontinuity set.

In the definitions, $\langle .,. \rangle$ denotes the usual scalar product of vectors. In the sliding region, the vector field F either points towards Σ on both sides or points away from Σ on both sides. These cases are called *attracting sliding* and *repelling sliding*, respectively. In the crossing region, the vector field points towards Σ on the one side and it points away from Σ on the other side. In the special case when $\langle F_1, n_1 \rangle (x_0) \cdot \langle F_2, n_2 \rangle (x_0) = 0$, the point x_0 is called *tangency point* of Σ.

Let us introduce the concept of *limit trajectories* which is used for generalising the concept of sliding and crossing regions to the codimension-2 case.

Definition 2.4 (α-trajectory)**.** *Consider a point $x_0 \in \Sigma$. A trajectory $\gamma : (t_0, t_1) \to \mathcal{D}$ with $\lim_{t \to t_0} \gamma(t) = x_0$, and $\lim_{t \to t_0} \langle F(\gamma(t)), n_1(x_0) \rangle \neq 0$ is called an **α-trajectory** of x_0 with respect to F.*

Definition 2.5 (ω-trajectory)**.** *Consider a point $x_0 \in \Sigma$. A trajectory $\gamma : (t_0, t_1) \to \mathcal{D}$ with $\lim_{t \to t_1} \gamma(t) = x_0$, and $\lim_{t \to t_1} \langle F(\gamma(t)), n_1(x_0) \rangle \neq 0$ is called an **ω-trajectory** of x_0 with respect to F.*

That is, α- and ω-trajectories tend to the points of Σ transversally in backward and forward direction of time, respectively. We refer α- and ω-trajectories together as *limit trajectories*. In the sliding and crossing regions, each point x_0 has exactly two limit trajectories, because a trajectory of both F_1 and F_2 can be found going through x_0. As Definitions 2.2 and 2.3 determine the direction of the vector field on the two sides of Σ, we can state the following proposition:

Proposition 2.6 (Limit trajectories in the sliding and crossing regions)**.** *In the sliding region, a point has either two α-trajectories (repelling sliding) or two ω-trajectories (attracting sliding). In the crossing region, a point has exactly one α- trajectory and one ω-trajectory.*

2.2.3 Construction of sliding dynamics

In the case of crossing, trajectories of F_1 and F_2 can be connected together at the discontinuity set Σ, and thus, a trajectory of F crosses Σ. However, in the case of sliding, the trajectories cannot be continued through Σ in either forward or backward direction of time, and they get stuck into Σ. Then, the dynamics can be extended to the discontinuity set by constructing the *sliding vector field* being tangent to Σ.

At a point $x_0 \in \Sigma_{sl}$, the simplest construction for the sliding vector field F_s is the convex combination of F_1 and F_2. That is, we consider the sliding vector field in the form

$$F_s = \alpha_1 F_1 + \alpha_2 F_2 = \sum_{i=1}^{2} \alpha_i F_i \tag{2.9}$$

with $\alpha_1, \alpha_2 \in \mathbb{R}$ and $\alpha_1 + \alpha_2 = 1$, and we require $\langle F_s, n_1 \rangle = 0$ for the tangency between F_s and Σ. These conditions lead to

$$\alpha_1(x_0) = \frac{\langle F_2, n_2 \rangle}{\langle F_1, n_1 \rangle + \langle F_2, n_2 \rangle}(x_0), \qquad \alpha_2(x_0) = \frac{\langle F_1, n_1 \rangle}{\langle F_1, n_1 \rangle + \langle F_2, n_2 \rangle}(x_0). \tag{2.10}$$

The formulae (2.10) show that the sliding vector exists uniquely except for the case when both F_1 and F_2 are tangent to Σ. However, the sliding vector field (2.9) is valid only in the sliding region.

This convex construction of the sliding vector is called *Filippov's convex method.* A more general construction is Utkin's non-convex *equivalent control method* [68], which is out of the scope of this thesis.

Example 2.7 (Mechanical example with Coulomb friction)**.** Consider a disk *slipping* on a rough horizontal surface, where the centre of the disk is connected to a fixed support by a spring (see the left panel of Figure 2.4). The mass of the disk is denoted by m, the gravitational acceleration is denoted by g, and the stiffness of the spring is k. The state of the disk is described by the position w and the velocity v of its centre of gravity, and by the velocity u of the contact point. By assuming Coulomb model with a friction coefficient μ, the dynamics of the variables $x = [w, v, u]$ is described by the vector field

$$F(x) = \begin{bmatrix} v \\ -k/m \cdot w - \mu g \operatorname{sgn} u \\ -k/m \cdot w - 3\mu g \operatorname{sgn} u \end{bmatrix}. \tag{2.11}$$

The discontinuity set Σ is defined by $H(x) = u = 0$. Then, (2.11) is a Filippov system with

$$F_1(x) = \begin{bmatrix} v \\ -k/m \cdot w - \mu g \\ -k/m \cdot w - 3\mu g \end{bmatrix}, \quad F_2(x) = \begin{bmatrix} v \\ -k/m \cdot w + \mu g \\ -k/m \cdot w + 3\mu g \end{bmatrix}, \quad n_1 = -n_2 = \begin{bmatrix} 0 \\ 0 \\ 1 \end{bmatrix}. \tag{2.12}$$

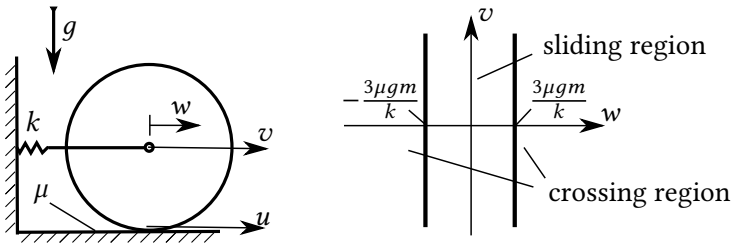

Figure 2.4: A mechanical example of Filippov system. Left panel: the sketch of the system with a slipping disk. Right panel: the sliding and crossing regions in the discontinuity set Σ.

The weights (2.10) of the sliding vector are given by $\alpha_1 = -k/(6\mu mg) \cdot w + 1/2$ and $\alpha_2 = k/(6\mu mg) \cdot w + 1/2$, and thus, the sliding vector (2.9) results in

$$F_s(x) = \begin{bmatrix} v \\ -2/3 \cdot k/m \cdot w \\ 0 \end{bmatrix}. \tag{2.13}$$

From Definition 2.2, the condition $\langle F_1, n_1 \rangle \cdot \langle F_2, n_2 \rangle > 0$ of the sliding region leads to $|w| < 3\mu gm/k$, hence, the sliding region is an infinite strip in the plane Σ (see the right panel of Figure 2.4). It can be checked that (2.13) is exactly the vector field that describes the dynamics of the disk in case of *rolling*. Moreover, by assuming the same coefficient μ for the static and the dynamic friction, the condition $|w| < 3\mu gm/k$ of the sliding region coincides with the dynamic condition of slipping from the contact forces.

2.3 Generalisation to the codimension–2 case

In this section, the main ideas of Filippovs theory are extended to those systems where there is a codimension–2 discontinuity set in the phase space. For this new concept of *extended Filippov systems*, we use similar notations to those of the Filippov systems (see Table 2.1). The analogies and differences from simple Filippov systems are emphasised along the section.

2.3.1 Definition of extended Filippov systems

Let us consider a domain $\mathcal{D} \in \mathbb{R}^m$ and an $m-2$ dimensional smooth manifold Σ. The manifold can be defined by

$$\Sigma := \left\{ x \in \mathcal{D} : H_{(1)}(x) = 0 \text{ and } H_{(2)}(x) = 0 \right\}, \tag{2.14}$$

where $H_{(1)}$ and $H_{(2)}$ are smooth real-valued functions on $\mathcal{D}$. We require that for any $x_0 \in \Sigma$, the gradients of $H_{(1)}$ and $H_{(2)}$ are nonzero and $\left\langle \nabla H_{(1)}(x_0), \nabla H_{(2)}(x_0) \right\rangle = 0$. Then,

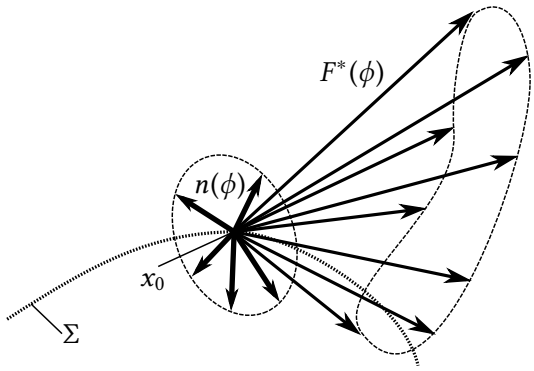

Figure 2.5: Behaviour of the vector field of an extended Filippov system at a point x_0 of the codimension–2 discontinuity set. The set $n(\phi)$ of the unit normal vectors forms a unit circle and the limit vector fiels $F^*(\phi)$ results in a closed curve in $\mathbb{R}^m$.

by defining

$$n_{(1)}(x_0) := \frac{\nabla H_{(1)}(x_0)}{\|\nabla H_{(1)}(x_0)\|}, \qquad n_{(2)}(x_0) := \frac{\nabla H_{(2)}(x_0)}{\|\nabla H_{(2)}(x_0)\|}, \tag{2.15}$$

we get an orthonormal basis $(n_{(1)}, n_{(2)})(x_0)$ for expressing vectors normal to Σ at x_0. The corresponding *unit* vectors can be expressed by

$$n(\phi)(x_0) := \cos(\phi)\, n_{(1)}(x_0) + \sin(\phi)\, n_{(2)}(x_0). \tag{2.16}$$

At a given point $x_0 \in \Sigma$, $n(\phi)$ maps the interval $[0, 2\pi)$ onto the set of the unit vectors normal to Σ. The meaning of ϕ is the angle of $n(\phi)$ measured from $n_{(1)}$. In the codimension-1 case, we had only the two directions n_1 and n_2 to approach a point x_0 of the discontinuity set. However, in the codimension-2 case, there are *continuously many* directions to approach Σ (see Figure 2.5), which are parametrised by the angle $\phi \in [0, 2\pi)$.

Now, we can state the definition of the extension of Filippov systems to the codimension-2 case which is the centre concept of this chapter:

Definition 2.8 (Extended Filippov system)**.** *Consider the manifold* (2.14) *and the differential equation*

$$\dot{x} = F(x), \tag{2.17}$$

where F is a vector field $\mathcal{D} \setminus \Sigma \to \mathbb{R}^m$. Suppose that the following conditions are satisfied:

(a) The vector field F is smooth on $\mathcal{D} \setminus \Sigma$.

(b) The limit

$$F^*(\phi)(x_0) := \lim_{\epsilon \to 0^+} F\left(x_0 + \epsilon n(\phi)(x_0)\right) \tag{2.18}$$

exists for all $x_0 \in \Sigma$ and $\phi \in [0, 2\pi)$.

(c) For all $x_0 \in \Sigma$, there exist $\phi_1, \phi_2 \in [0, 2\pi)$ for that $F^*(\phi_1) \neq F^*(\phi_2)$.

Then, the system (2.17) *is called an* ***extended Filippov system****.*

Condition (a) of Definition 2.8 requires the vector field to be smooth outside the discontinuity manifold Σ. Condition (b) states that at the discontinuity Σ, the limit vector F^* exists from any direction ϕ. Condition (c) ensures that there is indeed a discontinuity at any $x_0 \in \Sigma$. Conditions (b)-(c) are analogous to the uniform degree 1 of smoothness of the discontinuity manifold of Filippov systems. Thus, Definition 2.8 is a natural extension of Filippov systems to the codimension-2 case.

We call Σ a *codimension-2 discontinuity manifold*. To emphasize the difference from the concept in [36], it can be specified that Σ is an *isolated* discontinuity manifold and it is not connected to lower codimensional discontinuities.

Note that extended Filippov systems defined in Definition 2.8 are *not* piecewise smooth systems, and their discontinuity manifolds are not switching manifolds. In piecewise smooth systems, there are two regions of smooth dynamics separated by Σ. However, in extended Filippov systems, the region $\mathcal{D} \setminus \Sigma$ of smooth dynamics is a single simple connected set (compare Figures 2.2 and 2.5).

A consequence of Definition 2.8 is that at any point $x_0 \in \Sigma$, we get a *limit vector field* $F^*(x_0) : [0, 2\pi) \to \mathbb{R}^m$. This is analogous to (2.6) at Filippov systems, when there were two limit vectors $F_1^*(x_0)$ and $F_2^*(x_0)$ at any point $x_0 \in \Sigma$. However, at the extended Filippov systems, $F^*(\phi)(x_0)$ provides *continuously many* limit vectors at a point $x_0 \in \Sigma$. Due to the smoothness of F around Σ, the limit vector field $F^*(x_0)$ is a smooth 2π-periodic function of the direction angle ϕ. These results are demonstrated on an example:

Example 2.9 (Extended Filippov system)**.** Consider the system defined by

$$\dot{x} = F(x), \qquad F(x) = \begin{bmatrix} -\frac{x_1}{\sqrt{x_1^2+x_2^2}} + x_3 \\ -\frac{x_2}{\sqrt{x_1^2+x_2^2}} \\ -\frac{x_1}{\sqrt{x_1^2+x_2^2}} - x_3 \end{bmatrix}, \qquad x = \begin{bmatrix} x_1 \\ x_2 \\ x_3 \end{bmatrix} \in \mathcal{D} = \mathbb{R}^3. \tag{2.19}$$

The discontinuity set Σ is the line $x_1^2 + x_2^2 = 0$, which is a codimension-2 submanifold of $\mathbb{R}^3$. The discontinuity set can be generated simply by $H_{(1)}(x) = x_1$ and $H_{(2)}(x) = x_2$. Then, for $x_0 = [0, 0, x_3] \in \Sigma$, we get

$$n_{(1)} = \begin{bmatrix} 1 \\ 0 \\ 0 \end{bmatrix}, \quad n_{(2)} = \begin{bmatrix} 0 \\ 1 \\ 0 \end{bmatrix}, \quad n(\phi) = \begin{bmatrix} \cos\phi \\ \sin\phi \\ 0 \end{bmatrix}, \quad F^*(\phi)(x_0) = \begin{bmatrix} -\cos\phi + x_3 \\ -\sin\phi \\ -\cos\phi - x_3 \end{bmatrix}. \tag{2.20}$$

The limit vector field $F^*(\phi)(x_0)$ satisfies Definition 2.8, thus, (2.19) is an extended Filippov system.

2.3.2 Definition of sliding and crossing regions

Let us extend Definitions 2.2 and 2.3 to preserve the properties in Proposition 2.6 for extended Filippov systems. The concept of limit trajectories is extended by the following definitions:

Definition 2.10 (α-trajectory). *Consider a point $x_0 \in \Sigma$. A trajectory $\gamma : (t_0, t_1) \to \mathcal{D}$ with $\lim_{t\to t_0} \gamma(t) = x_0$ and*

$$\lim_{t\to t_0} \left\langle F(\gamma(t)), n_{(1)}(x_0) \right\rangle^2 + \lim_{t\to t_0} \left\langle F(\gamma(t)), n_{(2)}(x_0) \right\rangle^2 \neq 0 \tag{2.21}$$

*is called an **α-trajectory** of x_0 with respect to F.*

Definition 2.11 (ω-trajectory). *Consider a point $x_0 \in \Sigma$. A trajectory $\gamma : (t_0, t_1) \to \mathcal{D}$ with $\lim_{t\to t_1} \gamma(t) = x_0$, and*

$$\lim_{t\to t_1} \left\langle F(\gamma(t)), n_{(1)}(x_0) \right\rangle^2 + \lim_{t\to t_1} \left\langle F(\gamma(t)), n_{(2)}(x_0) \right\rangle^2 \neq 0 \tag{2.22}$$

*is called an **ω-trajectory** of x_0 with respect to F.*

The conditions (2.21) and (2.22) exclude the degenerate case when the trajectories are tangent to Σ at x_0. The α- and ω- trajectories together are called *limit trajectories*, as those of the simple Filippov systems. By using the concept of limit trajectories, we can define the sliding and crossing regions of extended Filippov systems:

Definition 2.12 (Sliding region of an extended Filippov system). *A point $x_0 \in \Sigma$ corresponds to the **sliding region** $\Sigma_{sl} \subset \Sigma$ if and only if it satisfies:*

(a) The limit trajectories of x_0 are either all α-trajectories or all ω-trajectories, and

(b) $\left\langle F^*(\phi)(x_0), n_{(1)}(x_0) \right\rangle^2 + \left\langle F^*(\phi)(x_0), n_{(2)}(x_0) \right\rangle^2 \neq 0$ for any $\phi \in [0, 2\pi)$.

Definition 2.13 (Crossing region of an extended Filippov system). *A point $x_0 \in \Sigma$ corresponds to the **crossing region** $\Sigma_{cr} \subset \Sigma$ if and only if x_0 has at least one α-trajectory and at least one ω-trajectory.*

Condition (b) of Definition 2.12 excludes the degenerate case when there exists an angle $\phi_1 \in [0, 2\pi)$ for that $F^*(\phi)$ is tangent to Σ at x_0. This case can be defined as a *tangency point* of an extended Filippov system, because it is on the boundary between sliding and crossing.

Let us now derive a theorem to provide a direct method to determine the sliding and crossing regions. Consider the system

$$\dot{r} = R(\phi), \qquad \dot{\phi} = V(\phi)/r, \tag{2.23}$$

where

$$R(\phi) := \langle F^*(\phi), n(\phi) \rangle (x_0), \qquad V(\phi) := \langle F^*(\phi), n(\phi + \pi/2) \rangle (x_0). \tag{2.24}$$

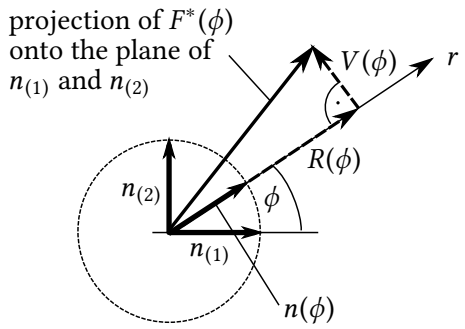

Figure 2.6: The definition of the functions $R(\phi)$ and $V(\phi)$.

In the vicinity of $x_0 \in \Sigma$, the system (2.23) describes the asymptotic behaviour of F projected into the plane orthogonal to Σ at x_0. The parameters r and ϕ provide polar coordinates on this plane spanned by the basis vectors $n_{(1)}(x_0)$ and $n_{(2)}(x_0)$ (see Figure 2.6). The coordinate $r > 0$ measures the distance from the discontinuity set, and the limit case $r = 0$ corresponds to x_0 for any angle ϕ. That is, (2.23) preserves the discontinuity of (2.17) and the limit trajectories of (2.17) tending to x_0 are related to the trajectories of (2.23) tending to $r = 0$.

Definition 2.14 (Attracting and repelling limit directions of a point x_0)**.** *Consider a point $x_0 \in \Sigma$ and the functions R and V in (2.24). A direction $\phi_0 \in [0, 2\pi)$ is called a **limit direction** of x_0 if $V(\phi_0) = 0$. The direction is called **attracting** when $R(\phi_0) < 0$, it is called **repelling** when $R(\phi_0) > 0$ and it is called **neutral** if $R(\phi_0) = 0$.*

Theorem 2.15. *Suppose that a point $x_0 \in \Sigma$ posesses $k > 0$ limit directions. Then, the following statements hold:*

(a) The point x_0 is located in the sliding region Σ_{sl} if and only if either all limit directions are attracting or all limit directions are repelling.

(b) The point x_0 is located in the crossing region Σ_{cr} if and only if x_0 has both attracting and repelling limit directions.

Proof. Let us denote the k limit directions by $\phi_i \in [0, 2\pi)$, $V(\phi_i) = 0$, $i = 1 \dots k$. Firstly, let us prove that each limit direction corresponds to a limit trajectory. For a chosen $i \in \{1 \dots k\}$, consider the initial condition $r(0) = \hat{r}$, $\phi(0) = \phi_i$. Then, the solution of (2.23) is $r(t) = \hat{r} + R(\phi_i) \cdot t$ and $\phi(t) \equiv \phi_i$. If $R(\phi_i) \neq 0$ then the trajectory tends to $r = 0$ when $t \to -\hat{r}/R(\phi_i)$. That is, this trajectory is a limit trajectory.

Secondly, let us prove that each limit trajectory corresponds to a limit direction ϕ_i. If a trajectory tends to $\bar{\phi} \in [0, 2\pi)$ when $r \to 0$ then $\bar{\phi} = \phi_i$, otherwise $\dot{\phi}$ diverges at $r \to 0$. The case when the limit trajectory does not tend to any $\bar{\phi}$ is possible only when V does not have zeroes, which case is excluded in the Theorem.

The sign of $R(\phi_i)$ decides the type of the limit trajectory. Hence, the presence of an α-trajectory is equivalent to the existence of a repelling limit direction and the presence of an ω-trajectory is equivalent to the existence of an attracting limit direction. Then, the Theorem follows directly from Definitions 2.12 and 2.13. □

Note that this theorem does not contain the case when x_0 possesses *no* limit directions. Still, there can exist spiral-shaped limit trajectories around x_0. Including this case into Theorem 2.15 would need further analysis.

Theorem 2.15 provides a direct method to decide if a point corresponds to the sliding or crossing region. The steps are the following: at any point x_0, the quantities $F^*(\phi)(x_0)$, $V(\phi)$ and $R(\phi)$ can be determined. Then, the limit directions can be obtained from the zeroes of V, and the type of the limit directions decides if the point lays in the sliding or crossing region. Let us demonstrate it on our previous example:

Example 2.16 (Application of Theorem 2.15)**.** Consider the extended Filippov system in Example 2.9. From the limit vector field F^* in (2.20), we get

$$R(\phi) = -1 + x_3 \cos\phi, \qquad V(\phi) = -x_3 \sin\phi. \tag{2.25}$$

The limit directions are $\phi_1 = 0$ and $\phi_2 = \pi$, which results $R(\phi_1) = -1 + x_3$ and $R(\phi_2) = -1 - x_3$. That is, the (attracting) sliding region of Σ is $|x_3| < 1$ and the crossing region is $|x_3| > 1$.

2.3.3 Construction of sliding dynamics

In (2.9), the sliding vector field was constructed as a convex combination of the two vector fields. In the codimension-2 case, there are continuously many limit vectors, thus, the convex combination can constructed as an integral average of the limit vector field in the form

$$F_s = \int_0^{2\pi} \alpha(\phi) \cdot F^*(\phi)\, \mathrm{d}\phi, \tag{2.26}$$

where $\alpha(\phi)$ is a $[0, 2\pi) \to \mathbb{R}$ function with

$$\int_0^{2\pi} \alpha(\phi)\, \mathrm{d}\phi = 1. \tag{2.27}$$

Hence, instead of the discrete weights α_i at (2.9), we have a weight function $\alpha(\phi)$ on the domain $[0, 2\pi)$.

In case of Filippov systems, formulae (2.10) provide a unique sliding vector field from convex combination. However, in the codimension-2 case, the uniqueness of F_s is not provided. In general, (2.26) results continuously many sliding vectors which are tangent to Σ, which is a similar problem to that of the intersecting codimension-1 discontinuity sets [36]. It is still an open question if there is a „most natural" choice of the sliding vector to eliminate this ambiguity.

However, if at a point x_0, the image $F^*(\phi)$ is located in a 2D subspace of $\mathbb{R}^m$, then F_s is provided uniquely by (2.26). This is stated in the following theorem:

Theorem 2.17. *Suppose that at a point x_0, the limit vector field $F^*(\phi)(x_0)$ can be written into the form*

$$F^*(\phi) = \overline{F} + A(\phi) \cdot F_A + B(\phi) \cdot F_B, \tag{2.28}$$

where

$$\overline{F} := \int_0^{2\pi} F^*(\phi) \mathrm{d}\phi, \tag{2.29}$$

$F_A, F_B \in \mathbb{R}^m$ and $A(\phi), B(\phi)$ are $[0, 2\pi) \to \mathbb{R}$ functions with

$$\int_0^{2\pi} A(\phi) \mathrm{d}\phi = 0, \qquad \int_0^{2\pi} B(\phi) \mathrm{d}\phi = 0. \tag{2.30}$$

Moreover, suppose that

$$\left\langle F_A, n_{(1)} \right\rangle \cdot \left\langle F_B, n_{(2)} \right\rangle - \left\langle F_A, n_{(2)} \right\rangle \cdot \left\langle F_B, n_{(1)} \right\rangle \neq 0. \tag{2.31}$$

Then, the construction (2.26) *provides a unique sliding vector F_s.*

Proof. By the substitution of (2.28) into (2.26), we get

$$F_s = \overline{F} + \int_0^{2\pi} \alpha(\phi) A(\phi) \mathrm{d}\phi \cdot F_A + \int_0^{2\pi} \alpha(\phi) B(\phi) \mathrm{d}\phi \cdot F_B = \overline{F} + a\, F_A + b\, F_B, \tag{2.32}$$

where

$$a := \int_0^{2\pi} \alpha(\phi) A(\phi) \mathrm{d}\phi, \qquad b := \int_0^{2\pi} \alpha(\phi) B(\phi) \mathrm{d}\phi. \tag{2.33}$$

As the sliding vector field is tangent to Σ, the conditions $\left\langle F_s, n_{(1)} \right\rangle = 0$ and $\left\langle F_s, n_{(2)} \right\rangle = 0$ provide two scalar equations for a and b. It can be proved by direct calculation, that except for the degenerate case (2.31), a and b are determined uniquely, that is, F_s is determined uniquely. □

Although, the Theorem ensures the uniqueness only for a special case, this class of systems has a practical importance in many mechanical systems with Coulomb friction lead to the form (2.28). Let us now demonstrate the results on our previous example:

Example 2.18 (Construction of the sliding vector)**.** Consider our extended Filippov system in Examples 2.9 and 2.16. The limit vector field F^* can be written into the form (2.28) with

$$\overline{F} = \begin{bmatrix} x_3 \\ 0 \\ -x_3 \end{bmatrix}, \quad F_A = \begin{bmatrix} -1 \\ 0 \\ -1 \end{bmatrix}, \quad F_B = \begin{bmatrix} 0 \\ -1 \\ 0 \end{bmatrix}, \quad A(\phi) = \cos\phi, \quad B(\phi) = \sin\phi. \tag{2.34}$$

Then, from the tangency condition, we get $a = x_{30}$, $b = 0$, and the sliding vector field becomes

$$F_s(x) = \begin{bmatrix} 0 \\ 0 \\ -2x_3 \end{bmatrix}. \tag{2.35}$$

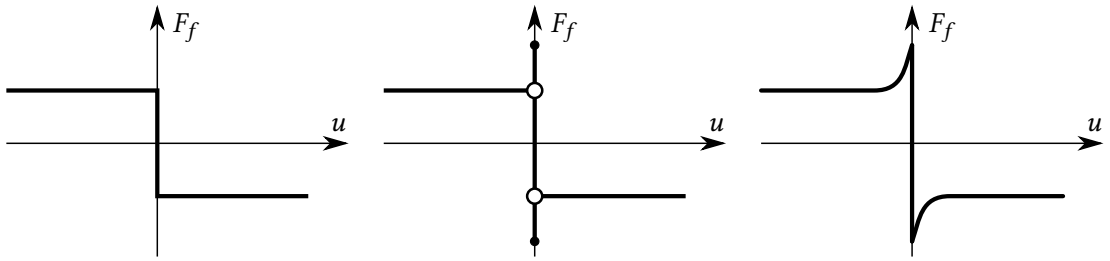

Figure 2.7: Characteristic curves of the different types of Coulomb models, where the friction force F_f is plotted against the relative velocity u of the surfaces at the contact point. In case of the simple Coulomb model (left panel) and the Stribeck model (right panel), the static friction force can be obtained as a limit of the dynamic friction force when the relative velocity tends to zero. These cases can be modelled appropriately with Filippov systems. In the case of the sticktion model (middle panel), the choice of the static friction is *inconsistent* with the limit of the dynamic friction at zero relative velocity, which causes problems during the modelling by a Filippov system. These properties of the model are essentially the same at extended Filippov systems with three-dimensional friction.

2.4 Application to mechanical problems

Mechanical problems with a single two-dimensional contact with Coulomb friction often lead to Filippov systems. A simple system can be found in Example 2.7 (see [5] for a more detailed analysis), and many other examples can be found in the literature (see e.g. [19] and its references). In those systems, the rolling or sticking state of the bodies corresponds to the sliding dynamics on the codimension-1 discontinuity set (switching surface). The two vector fields F_1 and F_2 are related to the mechanical slipping of the surfaces to the two directions. Moreover, if we use a friction model with a *consistent* static and dynamic friction (see the left and right panels of 2.7) then the boundary of the sliding and crossing regions corresponds to the boundary when the rolling/sticking behaviour ceases to exist (see Example 2.7).

The definition of extended Filippov systems was motivated by the desire to have a similar framework that can be applied to model mechanical systems with *three-dimensional* Coulomb friction. Now, the application is demonstrated on a simple mechanical example. More complicated applications can be found in Chapters 4 and 5 of this thesis.

2.4.1 Example: ball on the bottom of the pool

Consider a homogeneous ball rolling and slipping on the bottom of the pool (see Figure 2.8). We assume that there is Coulomb friction between the bottom of the ball and the bottom of the pool and there is a viscous force between the ball and the surrounding liquid. Of course, more complicated models could be used but we restrict ourselves to a simple model to focus on the application of the mathematical methods.

We use the following notations: m is the mass of the ball, r is the radius of the ball, μ is the friction coefficient of the Coulomb model, K is the linear viscous coefficient

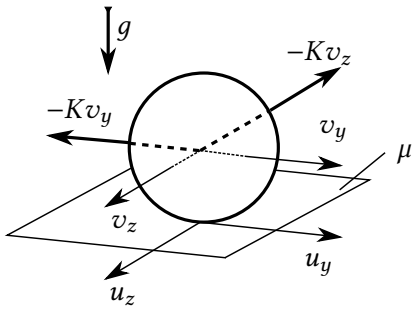

Figure 2.8: The mechanical model of the ball rolling on the bottom of a pool. The effect of the liquid is modelled by the viscous force components $-Kv_y$ and $-Kv_z$, and the Coulomb friction is acting at the bottom of the ball.

between the ball and the liquid, and g is the gravity.

The state of the ball is described by the coordinates v_y and v_z of the velocity of the centre of the ball and the coordinates u_y and u_z of the velocity of the bottom point of the ball. The components Ω_y and Ω_z of the angular velocity of the ball are expressed by

$$\Omega_y = \frac{1}{r}(u_z - v_z) \qquad\qquad \Omega_z = -\frac{1}{r}(u_y - v_y) \tag{2.36}$$

In the case when the ball is *slipping* on the ground, the relevant components of the Newton-Euler equations become

$$\begin{aligned} m\dot{v}_y &= -Kv_y + F_{Cy}, \\ m\dot{v}_z &= -Kv_z + F_{Cz}, \\ \frac{2}{5}mr^2 \cdot \frac{1}{r}(\dot{u}_z - \dot{v}_z) &= rF_{Cz}, \\ \frac{2}{5}mr^2 \cdot \frac{1}{r}(\dot{v}_y - \dot{u}_y) &= -rF_{Cy}, \end{aligned} \tag{2.37}$$

where the components of the Coulomb friction force are

$$F_{Cy} = -\mu mg\frac{u_y}{\sqrt{u_y^2+u_z^2}}, \qquad\qquad F_{Cz} = -\mu mg\frac{u_z}{\sqrt{u_y^2+u_z^2}}. \tag{2.38}$$

The dynamics of the slipping ball can be described by the extended Filippov system

$$\dot{x} = F(x), \qquad F(x) = \begin{bmatrix} -\frac{7}{2}\mu g\frac{u_y}{\sqrt{u_y^2+u_z^2}} - \frac{K}{m}v_y \\ -\frac{7}{2}\mu g\frac{u_z}{\sqrt{u_y^2+u_z^2}} - \frac{K}{m}v_z \\ -\mu g\frac{u_y}{\sqrt{u_y^2+u_z^2}} - \frac{K}{m}v_y \\ -\mu g\frac{u_z}{\sqrt{u_y^2+u_z^2}} - \frac{K}{m}v_z \end{bmatrix}, \qquad x = \begin{bmatrix} u_y \\ u_z \\ v_y \\ v_z \end{bmatrix} \in \mathcal{D} = \mathbb{R}^4. \tag{2.39}$$

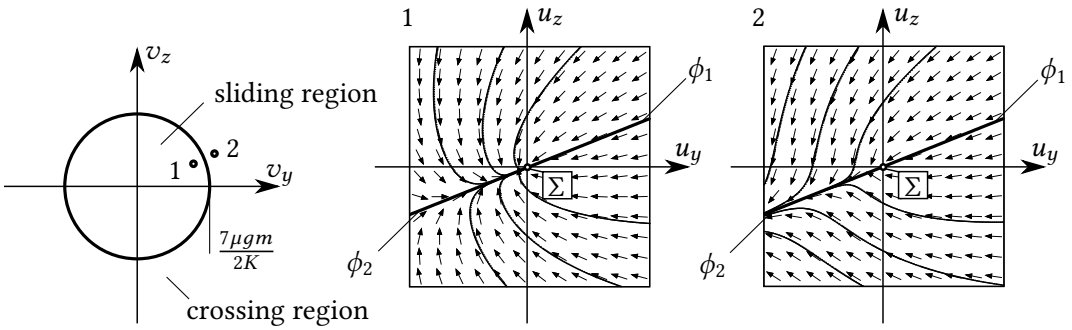

Figure 2.9: The sliding and crossing behaviour of the system (2.39). Left panel: the sliding and crossing regions in the discontinuity set Σ. Middle panel: a typical phase portrait of the system in the vicinity of x_0 in the *sliding* region. The phase portrait is projected into the plane of $n_{(1)}$ and $n_{(2)}$, that is, into the plane of coordinates u_y and u_z. In this case, the ball starts rolling in finite time. Right panel: a typical phase portrait of the system in the vicinity of x_0 in the *crossing* region. In this case, no rolling can occur.

In the 4D phase space, the discontinuity manifold Σ is the hyperplane $u_y = u_z = 0$, which corresponds to the case when the relative velocity at the contact point disappears. Let us choose $H_{(1)}(x) = u_y$ and $H_{(2)} = u_z$. Then, at a chosen point $x_0 = [0, 0, v_y, v_z] \in \Sigma$, we obtain

$$n_{(1)} = \begin{bmatrix} 1 \\ 0 \\ 0 \\ 0 \end{bmatrix}, \quad n_{(2)} = \begin{bmatrix} 0 \\ 1 \\ 0 \\ 0 \end{bmatrix}, \quad n(\phi) = \begin{bmatrix} \cos\phi \\ \sin\phi \\ 0 \\ 0 \end{bmatrix}, \quad F^*(\phi) = \begin{bmatrix} -\frac{7}{2}\mu g\cos\phi - \frac{K}{m}v_y \\ -\frac{7}{2}\mu g\sin\phi - \frac{K}{m}v_z \\ -\mu g\cos\phi - \frac{K}{m}v_y \\ -\mu g\sin\phi - \frac{K}{m}v_z \end{bmatrix}. \tag{2.40}$$

In this example, the angle ϕ has also a physical meaning: it expresses the direction of the velocity of the bottom point of the ball. Thus, the limit vector field $F^*(\phi)$ describes the dynamics of the ball for the different directions of the infinitesimally small slipping velocities.

For determining the slipping velocities, let us calculate the functions R and V according to (2.24):

$$R(\phi) = -\tfrac{7}{2}\mu g - \tfrac{K}{m}\left(v_y\cos\phi + v_z\sin\phi\right), \quad V(\phi) = -\tfrac{K}{m}\left(v_z\cos\phi - v_y\sin\phi\right). \tag{2.41}$$

By calculating the limit directions, we get $\phi_1 = \arctan(v_z, v_y)$ and $\phi_2 = \phi_1 + \pi$. That is, the limit directions correspond to the case when the slipping velocity of the bottom of the ball is parallel to the velocity of the centre of the ball. We get

$$R(\phi_1) = -\tfrac{7}{2}\mu g - \tfrac{K}{m}\sqrt{v_y^2 + v_z^2}, \qquad R(\phi_2) = -\tfrac{7}{2}\mu g + \tfrac{K}{m}\sqrt{v_y^2 + v_z^2}. \tag{2.42}$$

As $R(\phi_1)$ is always negative, ϕ_1 is always an attracting direction (see Figure 2.9). However, ϕ_2 is attracting only if

$$\sqrt{v_y^2 + v_z^2} < \frac{7\mu g m}{2K} =: v_{\text{crit}}. \tag{2.43}$$

That is, as the magnitude of the velocity of the centre of the ball is larger than the critical velocity v_{crit}, the bottom point of the ball starts slipping instantaneously into the direction ϕ_2, which is *opposite* to the velocity of the centre of the ball. The corresponding sliding and crossing regions are determined by (2.43), the boundary is a circle in the discontinuity set Σ (see Figure 2.9).

Inside the sliding region, the sliding dynamics can be defined which corresponds to mechanical rolling. The limit vector field (2.40) has the form of (2.28) by considering

$$\overline{F} = \begin{bmatrix} -\frac{K}{m}v_y \\ -\frac{K}{m}v_z \\ -\frac{K}{m}v_y \\ -\frac{K}{m}v_z \end{bmatrix}, \quad F_A = \begin{bmatrix} -\frac{7}{2}\mu g \\ 0 \\ -\mu g \\ 0 \end{bmatrix}, \quad F_B = \begin{bmatrix} 0 \\ -\frac{7}{2}\mu g \\ 0 \\ -\mu g \end{bmatrix}, \quad A(\phi) = \cos\phi, \quad B(\phi) = \sin\phi. \tag{2.44}$$

By requiring that the sliding vector in (2.28) is tangent to Σ, we get $a = -2Kmv_y/(7\mu g)$, $b = -2Kmv_z/(7\mu g)$, and the sliding vector field becomes

$$F_s(x) = \begin{bmatrix} 0 \\ 0 \\ -\frac{5K}{7m}v_y \\ -\frac{5K}{7m}v_z \end{bmatrix}. \tag{2.45}$$

By taking the rolling constraint $u_y \equiv u_y \equiv 0$, and applying the Newton-Euler equations for the rolling case, we get the *same* dynamics as F_s in (2.45). Moreover, by checking the maximum admissible static friction force in the rolling case, we get the same boundary as the condition (2.43) of the sliding region. Hence, the example demonstrates that the theory of extended Filippov system provides consistent results to our mechanical expectations when modelling three-dimensional Coulomb friction.

2.5 New results

Thesis Statement 2. By introducing the definition of *extended Filippov systems*, the concept of Filippov systems is generalised to vector fields that are discontinuous in an isolated codimension-2 manifold. In these systems, the directional limit of the vector field at the discontinuity set takes continuously many values. From the resulting *limit vector field*, the sliding and crossing regions of the discontinuity manifold are defined by using the concept of *limit trajectories*. In the sliding region, the sliding dynamics is defined by taking the convex combination of the limit vector field.

Related publications: [5], [11].

Chapter 3

Rolling-slipping transitions of dual-point rolling bodies

3.1 Introduction

In Chapter 1, the motion of a railway wheelset was analysed, which is rolling on the two rails. By generalising the arrangement of this mechanical system, we can consider a rigid body which is moving subjected to normal contacts with two *fixed* rigid surfaces. At each contact point, rolling or slipping can occur, which leads to 4 different kinematic situations. Besides the case when the body is rolling at both contact points (dual-point rolling), the body can slip at either one of the contact points (rolling-slipping) or even at both contact points (dual-point slipping).

During the motion of the body, the dynamics may switch between these four kinematic cases. Conditions of the slipping and sticking of the contact points are determined by the friction properties of the surfaces. The common feature of Coulomb friction and many other friction models is that the conditions of the slipping are expressed depending on the normal and tangential forces at the contact points (for a through overview of the different friction models, see recent review papers [55] and [51]). By using these models, the decision whether a contact point starts slipping requires determining the contact forces. This is not always possible in the scope of rigid body dynamics.

It can be checked that the contact forces are undetermined when a rigid body is in *rolling* contact with *both* rigid surfaces (dual-point rolling case), which is a similar problem to the indeterminacy of the reaction forces of a beam with two pin supports. As the contact forces are unknown, the condition of the slipping cannot be determined by applying the inequalities depending on the normal and tangential components of the contact forces. A possible method to treat this indeterminacy is to give up the rigid body model and model the deformation of the surfaces at least in the vicinity of the contact points.

But based on the results of Chapter 2, a different method can be developed which remains in the scope of rigid body motion. With the concepts of sliding and crossing re-

	Notation	Meaning
geometry	C	centre of the gravity of the moving body
	P^+, P^-	contact points (of the moving body)
	$\mathbf{r}^+, \mathbf{r}^-$	location of P^+ and P^- measured from C
	$\mathbf{n}^+, \mathbf{n}^-$	unit vectors normal to the surfaces at the contact points
	$\mathbf{t}_1^+, \mathbf{t}_2^+, \mathbf{t}_1^-, \mathbf{t}_2^-$	unit vectors in the tangent plane at the contact points
	$\mathbf{a}$	unit vector parallel to $\mathbf{r}^+ - \mathbf{r}^-$
kinematics	$\mathbf{v}^+, \mathbf{v}^-$	velocity of P^+ and P^-
	$u_1^+, u_2^+, u_1^-, u_2^-$	velocity components of the contact points
	v_a	velocity component of $\mathbf{v}^+$ and $\mathbf{v}^-$ in the direction of $\mathbf{a}$
	$\mathbf{v}_C$	velocity of C
	$\boldsymbol{\Omega}$	angular velocity of the body
	Ω_a	velocity component of $\boldsymbol{\Omega}$ in the direction of $\mathbf{a}$
	q	vector of generalised coordinates
	s	vector of quasi-velocities
equation of motion	$\mathbf{F}_e, \mathbf{M}_e$	resultant of the external loads
	$\mathbf{F}^+, \mathbf{F}^+$	contact forces at P^+ and P^-
	N^+, N^-	normal force components
	$T_1^+, T_2^+, T_1^-, T_2^-$	tangential force components
	m	mass of the body
	$\mathbf{J}(q)$	mass moment of inertia of the body
	μ	friction coefficient of Coulomb model (both static and dynamic)
nonsmooth dynamics	$\mathcal{D} \subset \mathbb{R}^8$	phase space
	$x = (q, s) \in \mathcal{D}$	state vector of the system
	$F_{\mathrm{SS}}(x)$	vector field for the slipping-slipping case (extended Filippov system)
	$F_{\mathrm{SR}}(x)$	vector field for the slipping-rolling case (Filippov system)
	$F_{\mathrm{RS}}(x)$	vector field for the rolling-slipping case (Filippov system)
	$F_{\mathrm{RR}}(x)$	vector field for the rolling-rolling case (smooth system)
	Σ_{SR}	discontinuity set of F_{SS} at rolling at P^-
	Σ_{RS}	discontinuity set of F_{SS} at rolling at P^+
	Σ_{RR}	double discontinuity in the intersection if Σ_{SR} and Σ_{RS} at dual-point rolling
	ϕ^+, ϕ^-	angle measured in the phase space about Σ_{RS} and Σ_{SR}
	$n^+(\phi^+), n^-(\phi^-)$	unit vectors normal to Σ_{RS} and Σ_{SR}, respectively
	$F_{\mathrm{SS}}^{*+}(\phi^+), F_{\mathrm{SS}}^{*-}(\phi^-)$	limit vector fields of F_{SS} at Σ_{RS} and Σ_{SR}, respectively
	$\hat{n}(\phi^+, \phi^-)$	unit vectors normal to Σ_{RR}
	$\hat{F}_{\mathrm{SS}}^*(\phi^+, \phi^-)$	limit vector field at the double discontinuity Σ_{RR}
	$\hat{R}$	components of $\hat{F}_{\mathrm{SS}}^*$ in the direction of $\hat{n}$
	$\hat{V}^+, \hat{V}^-$	component of $\hat{F}_{\mathrm{SS}}^*$ in directions normal to both $\hat{n}$ and Σ_{RR}

Table 3.1: Important notations of Chapter 3. For the other notations about extended Filippov systems, see Table 2.1.

gions, theory of Filippov systems provides a natural method to determine condition of slipping, which is valid for friction models where static and dynamic friction models fit consistently (see Figure 2.7). In Chapter 2, we introduced the concept of extended Filippov systems, which makes it possible to find sliding and crossing regions in mechanical systems containing *spatial* Coulomb friction. In that way, conditions of slipping can be determined from purely the differential equations for the *slipping* cases, and thus, we can avoid calculating the contact forces in case of the dual-point rolling motion of a body.

The motivations behind analysing bodies in dual-point contact were the applications in the subsequent chapters. In Chapter 4, the model of a special flowmeter is analysed where a ball is in dual-point contact with a cylindrical vessel and rolling-slipping transitions can occur. In Chapter 5, the railway wheelset is analysed from the point of view of slipping on the rails. References about these applications can be found in the related chapters. A further application area may be the motion of the rolling element in tapered roller bearings [76] or in angular contact ball bearings [13, 54].

The structure of the chapter is the following: In Section 3.2, the kinematic description of the body is presented with introducing an appropriate choice of variables. In Section 3.3, the structure of the differential equations is derived for the four kinematic cases by using the concepts of Filippov systems and extended Filippov systems. In Section 3.4, the trajectories of slipping dynamics are used to determine the conditions of the slipping in the case of dual-point rolling. The new results are summarised in Section 3.5.

3.2 Kinematics of a body with dual-point contact

Consider a rigid body which is in contact with two fixed rigid surfaces. The rigid body without constraints has 6 degrees of freedom, and the contact conditions with the two supporting bodies result in 2 independent scalar geometric constraints. Thus, the body with dual-point contact has 4 degrees of freedom, and hence, at least locally, the geometric state can be described by the generalised coordinates

$$q = [q_1, q_2, q_3, q_4]. \tag{3.1}$$

In practice, the generalised coordinates are usually chosen intuitively (see (1.19)).

3.2.1 Geometry

The centre of gravity of the body is denoted by C and the two contact points are denoted by P^+ and P^- (see Figure 3.2). The loci of the contact points are denoted by $\mathbf{r}^+$ and $\mathbf{r}^-$, which are measured from the centre C of gravity. The unit normal vectors at the contact points are denoted by $\mathbf{n}^+$ and $\mathbf{n}^-$, respectively. During this chapter, it is assumed that $\mathbf{r}^+(q)$, $\mathbf{r}^-(q)$, $\mathbf{n}^+(q)$ and $\mathbf{n}^-(q)$ depend smoothly on q in a neighbourhood

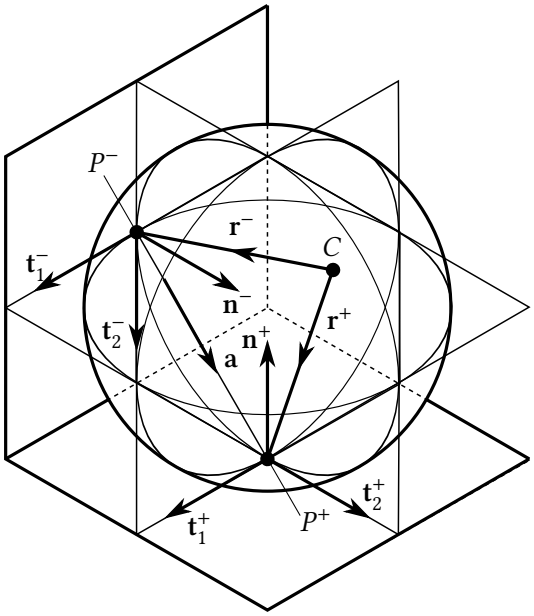

Figure 3.2: The definition of the local coordinate systems at the contact points. The figure shows an example of a ball rolling between two perpendicular planes, but the analysis is valid for arbitrary geometries. The centre C of the gravity is chosen *not* at the geometric centre of the ball to demonstrate that $\mathbf{n}^+$ and $\mathbf{n}^-$ do not necessarily lay in the plane spanned by $\mathbf{r}^+$ and $\mathbf{r}^-$.

of an initial position $q = 0$. For that, it is required that the surfaces of the contacting bodies are smooth and it is excluded that further contact points appear. In practice, the explicit dependence of these vectors on q can be quite complicated, but it can be determined locally by the parametric description of the surfaces (see Section 1.5).

Let us construct some coordinate systems at the contact points in the following way. Let

$$\mathbf{a} := \frac{\mathbf{r}^+ - \mathbf{r}^-}{\|\mathbf{r}^+ - \mathbf{r}^-\|} \tag{3.2}$$

be the unit vector in the direction of the axis between the contact points. Then, let

$$\mathbf{t}_1^+ := \frac{\mathbf{a} \times \mathbf{n}^+}{\|\mathbf{a} \times \mathbf{n}^+\|}, \qquad \mathbf{t}_1^- := \frac{\mathbf{a} \times \mathbf{n}^-}{\|\mathbf{a} \times \mathbf{n}^-\|} \tag{3.3}$$

be the unit vectors which are tangent to the surfaces at the corresponding contact point and which are perpendicular to $\mathbf{a}$. The unit vectors of the other tangent direction can be obtained by

$$\mathbf{t}_2^+ := \mathbf{n}^+ \times \mathbf{t}_1^+, \qquad \mathbf{t}_2^- := \mathbf{n}^- \times \mathbf{t}_1^- \tag{3.4}$$

which unit vectors point to the direction of the projection of $\mathbf{r}^+ - \mathbf{r}^-$ onto the tangent planes at the contact points. If special cases $\mathbf{t}_1^+ = \mathbf{0}$ and $\mathbf{t}_1^- = \mathbf{0}$ are excluded from the analysis then $(\mathbf{n}^+, \mathbf{t}_1^+, \mathbf{t}_2^+)$ and $(\mathbf{n}^-, \mathbf{t}_1^-, \mathbf{t}_2^-)$ form orthonormal bases at the corresponding contact points (see Figure 3.2).

3.2.2 Kinematics

After choosing the generalised coordinates, the trivial description of the kinematic state of the body is to use the time derivatives $\dot{q} = [\dot{q}_1, \dot{q}_2, \dot{q}_3, \dot{q}_4]$. However, it is more convenient to describe the velocity state by variables by which the rolling constraints can be expressed easier. For that, the velocities of the contact points are used to express the velocity state of the body.

In the coordinate systems at the contact points, the velocities of the contact points can be written into the form

$$\begin{aligned} \mathbf{v}^+ &:= u_1^+ \mathbf{t}_1^+ + u_2^+ \mathbf{t}_2^+, \\ \mathbf{v}^- &:= u_1^- \mathbf{t}_1^- + u_2^- \mathbf{t}_2^-, \end{aligned} \tag{3.5}$$

where $u_1^+, u_1^-, u_2^+, u_2^-$ are the components of $\mathbf{v}^+$ and $\mathbf{v}^-$ in the corresponding tangent directions and the normal components are zero due to the geometric constraints.

The velocities $\mathbf{v}^+$ and $\mathbf{v}^-$ cannot be chosen fully independently, because the rigid body motion results the relation

$$\mathbf{v}^+ - \mathbf{v}^- = \Omega \times (\mathbf{r}^+ - \mathbf{r}^-), \tag{3.6}$$

where Ω is the *angular velocity* of the body. By taking the scalar product of (3.6) by the vector $\mathbf{a}$, we get

$$\langle \mathbf{v}^+, \mathbf{a} \rangle - \langle \mathbf{v}^-, \mathbf{a} \rangle = \langle \Omega \times (\|\mathbf{r}^+ - \mathbf{r}^-\| \cdot \mathbf{a}), \mathbf{a} \rangle = 0. \tag{3.7}$$

Substitution of (3.5) into (3.7) leads to

$$u_2^+ \langle \mathbf{t}_2^+, \mathbf{a} \rangle - u_2^- \langle \mathbf{t}_2^-, \mathbf{a} \rangle = 0. \tag{3.8}$$

This condition can be satisfied by introducing a new variable u_a with

$$u_a := u_2^+ \langle \mathbf{t}_2^+, \mathbf{a} \rangle = u_2^- \langle \mathbf{t}_2^-, \mathbf{a} \rangle \tag{3.9}$$

which is the common velocity component of the contact points in the direction of the axis $\mathbf{r}^+ - \mathbf{r}^-$. Then, the velocities of the contact points can be written in the form

$$\begin{aligned} \mathbf{v}^+ &= u_1^+ \mathbf{t}_1^+ + u_a / \langle \mathbf{t}_2^+, \mathbf{a} \rangle \mathbf{t}_2^+, \\ \mathbf{v}^- &= u_1^- \mathbf{t}_1^- + u_a / \langle \mathbf{t}_2^-, \mathbf{a} \rangle \mathbf{t}_2^-. \end{aligned} \tag{3.10}$$

Therefore, the velocity of the contact points can be expressed by the variables u_1^+, u_1^- and u_a. The velocity state of the body is still not fully determined by these three variables. The cross product of $\mathbf{a}$ and (3.6) leads to

$$\mathbf{a} \times (\mathbf{v}^+ - \mathbf{v}^-) = \|\mathbf{r}^+ - \mathbf{r}^-\| \cdot \Omega - \|\mathbf{r}^+ - \mathbf{r}^-\| \cdot \langle \mathbf{a}, \Omega \rangle \cdot \mathbf{a}. \tag{3.11}$$

A new scalar variable Ω_a is defined by

$$\Omega_a := \langle \mathbf{a}, \Omega \rangle, \tag{3.12}$$

which is the component of the angular velocity $\boldsymbol{\Omega}$ in the direction of the axis $\mathbf{a}$, and whose value can be chosen independently from the velocities of the contact points. By substituting (3.12) into (3.11), the angular velocity becomes

$$\boldsymbol{\Omega} = \Omega_a \cdot \mathbf{a} + \mathbf{a} \times \frac{\mathbf{v}^+ - \mathbf{v}^-}{\|\mathbf{r}^+ - \mathbf{r}^-\|}. \tag{3.13}$$

Finally, we have four scalar variables u_1^+, u_1^-, u_a and Ω_a, which determine the velocity of the contact points and the angular velocity by (3.10) and (3.13). Then, the velocity state of the body is described by these four variables; they are called *quasi-velocities* ([26], p. 254) and are denoted by

$$s = [s_1, s_2, s_3, s_4] = [u_1^+, u_1^-, u_a, \Omega_a]. \tag{3.14}$$

The advantage of choosing this set of quasi-velocities is the simple expression of the rolling constraints. If the body is rolling at P^+ then $\mathbf{v}^+ = \mathbf{0}$, which is equivalent to

$$u_1^+ = u_a = 0. \tag{3.15}$$

If the body is rolling at P^- then $\mathbf{v}^- = \mathbf{0}$ leads to

$$u_1^- = u_a = 0. \tag{3.16}$$

Note that the rolling constraints (3.15) and (3.16) are not fully independent, and there are only three independent constraints in the case of dual-point rolling (see also (1.48)).

As the quasi-velocities fully describe the velocity state through (3.10) and (3.13), the time derivatives of the generalised coordinates can be expressed as a linear combination of the quasi-velocities in the form

$$\dot{q} = K(q) \cdot s, \tag{3.17}$$

where $K(q)$ is a 4 by 4 matrix possibly depending on q.

The analysis of this chapter follows the choice (3.14) of quasi-velocities, but the derivations leaves open the possibility for some modifications (see (4.10) and (5.18)). The variables u_1^+, u_1^- and u_a can be modified by a constant multiplier, and Ω_a can be replaced by any quasi-velocity for which $\dot{q}$ can be expressed in the form (3.17).

3.3 Discontinuous dynamics

3.3.1 Equations of motion

At the contact points, let us denote the contact forces by $\mathbf{F}^+$ and $\mathbf{F}^-$, respectively, which consist of normal forces and friction forces in the form

$$\begin{aligned} \mathbf{F}^+ &= N^+\mathbf{n}^+ + T_1^+\mathbf{t}_1^+ + T_2^+\mathbf{t}_2^+, \\ \mathbf{F}^- &= N^-\mathbf{n}^- + T_1^-\mathbf{t}_1^- + T_2^-\mathbf{t}_2^-. \end{aligned} \tag{3.18}$$

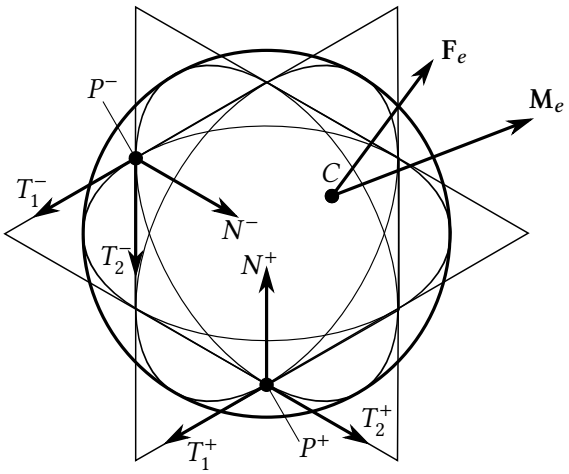

Figure 3.3: Force system acting on the moving body.

It is assumed that the resultant of all other forces acting on the body is given as a force $\mathbf{F}_e$ acting at C and a torque $\mathbf{M}_e$ (see Figure 3.3). Let m denote the mass of the body and let $\mathbf{J}(q)$ denote the mass moment of inertia which possibly depends on q. Then, the Newton-Euler equations of the body become

$$\begin{aligned} m\dot{\mathbf{v}}_C &= \mathbf{F}^+ + \mathbf{F}^- + \mathbf{F}_e, \\ \mathbf{J}(q)\dot{\Omega} + \Omega \times (\mathbf{J}(q)\Omega) &= \mathbf{r}^+ \times \mathbf{F}^+ + \mathbf{r}^- \times \mathbf{F}^- + \mathbf{M}_e, \end{aligned} \tag{3.19}$$

where $\mathbf{v}_C$ is the velocity of the centre C of gravity given by

$$\mathbf{v}_C = \mathbf{v}^+ - \Omega \times \mathbf{r}^+. \tag{3.20}$$

Note that the kinematic quantities $\mathbf{v}_C$ and Ω can be expressed by the quasi-velocities s.

It is assumed that there is Coulomb friction at both contact points with a uniform μ coefficient of friction for both static and dynamic case. In the dynamic case when the body is slipping at P^+ or P^-, the contact forces become

$$\begin{aligned} \mathbf{F}^+ &:= N^+\mathbf{n}^+ - \mu N^+ \frac{\mathbf{v}^+}{\|\mathbf{v}^+\|}, \\ \mathbf{F}^- &:= N^-\mathbf{n}^- - \mu N^- \frac{\mathbf{v}^-}{\|\mathbf{v}^-\|}, \end{aligned} \tag{3.21}$$

respectively. In the case of rolling at P^+ or P^-, the inequalities

$$\begin{aligned} \|\mathbf{F}^+ - N^+\mathbf{n}^+\| &\leq \mu N^+, \\ \|\mathbf{F}^- - N^-\mathbf{n}^-\| &\leq \mu N^- \end{aligned} \tag{3.22}$$

kinematic case	acronym	constraints				free variables	
		u_1^+	u_1^-	u_a	Ω_a	in s	in q
slipping-slipping	SS					4	4
slipping-rolling	SR		0	0		2	4
rolling-slipping	RS	0		0		2	4
rolling-rolling	RR	0	0	0		1	4

Table 3.4: The four kinematic cases of the body with the corresponding kinematic constraints. The first and second letter of the acronym corresponds to the slipping (S) or rolling (R) state of the contact point P^+ and P^-, respectively. These acronyms are used along Chapters 3-5.

ensure the dynamic condition of rolling.

According to the slipping or rolling state of the two contact points, there are four *kinematic cases* of the body, which are denoted by the two-letter acronyms SS, SR, RS, and RR (see Table 3.4). In each case, the dynamics can be expressed as a set of first-order differential equations in the form

$$\begin{aligned} \dot{q} &= K(q) \cdot s, \\ \dot{s} &= f(q, s), \end{aligned} \tag{3.23}$$

where the first equation is given by (3.17) and the second equation can be calculated from the dynamic equations (3.19) and the corresponding appropriate conditions from (3.15), (3.16) and (3.21) (see Table 3.5). The full state space of the body can be described by the 8 dimensional vector

$$x = (q, s) = [q_1, q_2, q_3, q_4, u_1^+, u_1^-, u_a, \Omega_a], \tag{3.24}$$

and then, (3.23) can be written into the form

$$\dot{x} = F(x) = (K(q) \cdot s, f(q, s)). \tag{3.25}$$

In the presence of additional constraints of the cyclic coordinates, some variables from (3.24) can be excluded (see (4.23) and (5.31)).

Example 3.1 (Kinematic oscillations of railway wheelsets)**.** In Chapter 1, the chosen generalised coordinates were $q = [y, \psi, \varphi, w]$ (see (1.19)). Instead of Ω_a, it is more convenient to choose s_4 with $\dot{w} = s_4$, because of the additional kinematic constraint of constant speed of the train (1.22). The kinematic oscillations correspond to the dual-point rolling (RR) case, that is, the quasi-velocities are $s = [u_1^+, u_1^+, u_a, s_4] = [0, 0, 0, s_4]$. Then, by taking

$$K(q) = \begin{bmatrix} 0 & 0 & 0 & f_y(y, \psi)/v \\ 0 & 0 & 0 & f_\psi(y, \psi)/v \\ 0 & 0 & 0 & f_\varphi(y, \psi)/v \\ 0 & 0 & 0 & 1 \end{bmatrix} \tag{3.26}$$

	SS	**SR**	**RS**	**RR**
time derivatives of the quasi-velocities ($\dot{s}$)	4			
components of $\mathbf{F}^+$ and $\mathbf{F}^-$	6			
total number of unknowns	**10**			
dynamic equations (3.19)	6			
kinematic constraints (3.15)-(3.16)	0	2	2	3
Coulomb friction (3.21)	4	2	2	0
total number of equations	**10**	**10**	**10**	**9**
missing equations	0	0	0	1

Table 3.5: The number of the unknowns and the equations in the different kinematic cases. It can be seen that in Cases SS, SR and RS, there are enough equations to determine the differential equations and the contact forces. However, in Case RR, the number of equations is less than the unknowns which leads to indeterminacy in the contact forces.

from (1.24), by taking $f(q,s) = [0,0,0,0]$ and by choosing the initial conditions $s(0) = [0,0,0,v]$, the equations (3.23) provide the same dynamics as (1.24). The slipping cases of the railway wheelset are investigated in Chapter 5.

3.3.2 Dynamics of the different cases

In each kinematic case, we get a different vector field $F(x)$, which are denoted by $F_{\mathrm{SS}}(x), F_{\mathrm{SR}}(x), F_{\mathrm{RS}}(x)$ and $F_{\mathrm{RR}}(x)$. Because of the constraints and discontinuities, these four vector fields are valid in different subsets of the domain $\mathcal{D} \ni x$ of the phase space.

Case SS The discontinuities of the system F_{SS} are caused by the Coulomb friction (3.21) for slipping. By substituting (3.10) into (3.21), we get

$$T_1^+ = -\mu N^+ \frac{u_1^+}{\sqrt{(u_1^+)^2 + u_a^2 \left\langle \mathbf{t}_2^+, \mathbf{a} \right\rangle}}, \qquad T_2^+ = -\mu N^+ \frac{u_a \left\langle \mathbf{t}_2^+, \mathbf{a} \right\rangle}{\sqrt{(u_1^+)^2 + u_a^2 \left\langle \mathbf{t}_2^+, \mathbf{a} \right\rangle^2}}, \tag{3.27}$$

$$T_1^- = -\mu N^+ \frac{u_1^-}{\sqrt{(u_1^-)^2 + u_a^2 \left\langle \mathbf{t}_2^-, \mathbf{a} \right\rangle}}, \qquad T_2^- = -\mu N^- \frac{u_a \left\langle \mathbf{t}_2^-, \mathbf{a} \right\rangle}{\sqrt{(u_1^-)^2 + u_a^2 \left\langle \mathbf{t}_2^-, \mathbf{a} \right\rangle^2}}. \tag{3.28}$$

The discontinuities of (3.27) and (3.28) appear in the vector field F_{SS}. The contact force (3.27) becomes discontinuous if $u_1^- = u_a = 0$, which corresponds to Case SR (see Table 3.4). Therefore, we can define the set

$$\Sigma_{\mathrm{SR}} = \left\{ x \in \mathcal{D} : u_1^- = 0 \text{ and } u_a = 0 \right\}, \tag{3.29}$$

which is a *codimension–2 discontinuity set* of F_{SS} (see Definition 2.8). Similarly, the contact force (3.28) is discontinuous when $u_1^+ = u_a = 0$, which corresponds to Case RS. Then, we obtain the set

$$\Sigma_{RS} = \{x \in \mathcal{D} : u_1^+ = 0 \text{ and } u_a = 0\}, \tag{3.30}$$

which is a codimension–2 discontinuity set of F_{SS}. That is, the vector field F_{SS} is an *extended Filippov system* (see Definition 2.8) with discontinuity sets Σ_{SR} and Σ_{RS}. These discontinuity sets intersect each other at $u_1^+ = u_1^- = u_a = 0$, which defines the set

$$\Sigma_{RR} = \{x \in \mathcal{D} : u_1^+ = 0 \text{ and } u_1^- = 0 \text{ and } u_a = 0\}, \tag{3.31}$$

that is,

$$\Sigma_{RR} = \Sigma_{SR} \cup \Sigma_{RS}. \tag{3.32}$$

In the 8 dimensional phase space of F_{SS}, Σ_{RR} is a 5 dimensional (codimension–3) hyperplane in the intersection of the 6 dimensional (codimension–2) hyperplanes Σ_{RS} and Σ_{SR} (see Figure 3.6). This results a similar situation to the intersection of codimension–1 discontinuity sets in simple Filippov systems (see [20] and [36]). In the phase space, the unit vectors related to the variables u_1^+, u_1^- and u_a are denoted by e_1^+, e_1^- and e_a, respectively (see Figure 3.6).

Consider the codimension-2 discontinuity set Σ_{SR}. By comparing (3.29) and (2.14), we have $H_{(1)} = u_1^-$ and $H_{(2)} = u_a$, and thus, (2.16) becomes

$$n^-(\phi^-) = \cos\phi^- e_1^- + \sin\phi^- e_a. \tag{3.33}$$

Then, the corresponding limit vector field is

$$F_{SS}^{*-}(\phi^-)(x_0) := \lim_{\epsilon \to 0^+} F_{SS}\left(x_0 + \epsilon n^-(\phi^-)\right). \tag{3.34}$$

We can define the function $R^-(\phi^-)$ and $V^-(\phi^-)$ according to (2.24).

Note that as there are two discontinuity sets, the notations n^-, ϕ^- and n^+, ϕ^+ are used correspondingly to the discontinuity sets Σ_{SR} and Σ_{RS}, respectively. For the discontinuity set Σ_{RS}, we get the unit vectors

$$n^+(\phi^+) = \cos\phi^+ e_1^+ + \sin\phi^+ e_a, \tag{3.35}$$

and the limit vector field

$$F_{SS}^{*+}(\phi^+)(x_0) := \lim_{\epsilon \to 0^+} F_{SS}\left(x_0 + \epsilon n^+(\phi^+)\right). \tag{3.36}$$

The corresponding functions $R^+(\phi^+)$ and $V^+(\phi^+)$ are defined according to (2.24).

Case SR The dynamics of F_{SR} corresponds to the case $u_1^- = u_a = 0$, that is, F_{SR} can be restricted to Σ_{SR}. Then, (3.28) is no more valid and (3.27) becomes

$$T_1^+ = -\mu N^+ \operatorname{sgn} u_1^+, \qquad T_2^+ = 0. \tag{3.37}$$

That is, F_{SR} has a discontinuity at $u_1^+ = 0$, which corresponds to Σ_{RR}. Hence, F_{SR} restricted to Σ_{SR} is a *Filippov system* with the codimension–1 discontinuity set Σ_{RR} (see Definition 2.1).

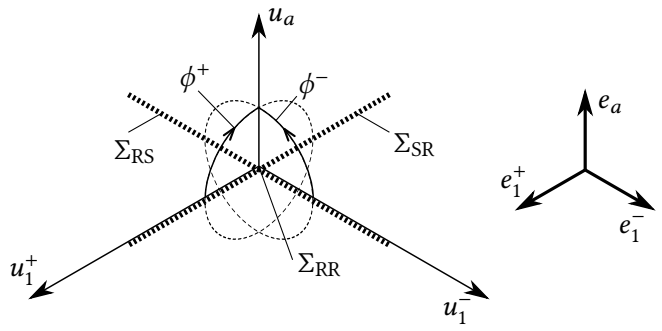

Figure 3.6: The discontinuity sets of the system. Among the 8 dimensions of $x = (q, s)$), only u_1^+, u_1^- and u_a are shown in the figure. The codimension-3 (5 dimensional) discontinuity set Σ_{RR} is located in the intersection of the codimension-2 (6 dimensional) discontinuity sets Σ_{SR} and Σ_{RS}.

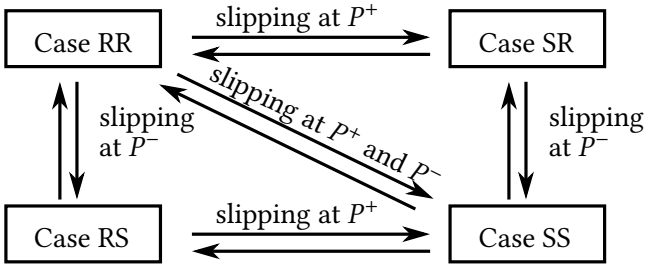

Figure 3.7: The sketch of the transitions between the different kinematic cases of the body.

Case RS In the slipping-rolling case, the vector field F_{RS} can be restricted to Σ_{RS}. Then, (3.27) is not valid and (3.28) becomes

$$T_1^- = -\mu N^- \operatorname{sgn} u_1^-, \qquad T_2^- = 0. \tag{3.38}$$

The set Σ_{RR} is a codimension−1 discontinuity set of F_{RS}, and hence, F_{RS} is a Filippov system.

Case RR In the rolling-rolling case, there is no need for the slipping Coulomb friction law (3.21) (see Table 3.5). That is, the discontinuities of (3.27) and (3.28) do not appear in F_{RR}. Thus, F_{RR} is a smooth vector field restricted to the set Σ_{RR}.

3.3.3 Indeterminacy of the contact forces

If we want to check the condition of the slipping of the body when switching between the different kinematic cases (see Figure 3.7), conditions (3.21) of the static Coulomb friction can be applied. For that, the components of the contact forces $\mathbf{F}^+$ and

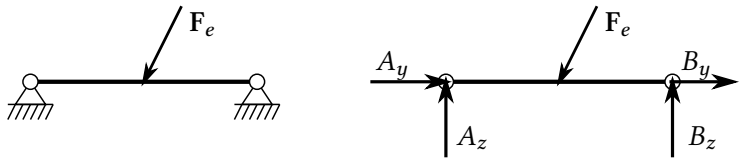

Figure 3.8: Static indeterminacy of the reaction forces at a beam with two pin supports. The components A_z and B_z still can be determined from the external force $\mathbf{F}_e$, but the components A_y and B_y are undetermined. A similar problem occurs at a body which is rolling on two surfaces (Case RR). Then, the *velocity* is constrained to zero at P^+ and P^- and the contact force components in the direction of $\mathbf{r}^+ - \mathbf{r}^-$ are undetermined in the scope of rigid body mechanics.

$\mathbf{F}^-$ should be known. The system of equations (3.15), (3.16), (3.19) and (3.21) provides a unique solution for these contact forces in Cases SS, SR and RS (see Table 3.5).

However, there are not enough independent equations in Case RR, and thus, the contact forces cannot be fully determined (this is a similar problem to that of the beam with two pin supports, see Figure 3.8). Consequently, the condition (3.22) cannot be checked directly.

One possibility to resolve this uncertainty of the contact forces is modelling the elastic properties of the body and the supports, which would lead to many complications in the model. However, by using the results of Chapter 2, a solution can be found in the scope of the present model of rigid body dynamics, as well. *The idea is that there is no need to calculate the contact forces in case of rolling, but the condition of slipping can be determined from the attracting or repelling properties of the vector field of the slipping case (see the example in Subsection 2.4.1).*

3.4 Conditions of slipping in case of dual-point rolling

To avoid the calculation of the contact forces in Case RR, we use the concept of limit trajectories of Filippov systems and extended Filippov systems to determine whether the slipping vector field pulls away or pushes back the trajectories to the discontinuity sets.

To carry out that, first we have to express the conditions whether the vector fields of the slipping cases SS, SR and RS generate the sliding dynamics compatibly to the related lower dimensional vector fields. Then, we have to investigate limit trajectories at Σ_{RR}, which are located in the intersection of *two* codimension-2 discontinuity sets. Then, the conditions of slipping can be determined by categorizing the possible scenarios of the limit trajectories.

3.4.1 Compatibility of the dynamics of the different cases

By using the theory of Filippov systems (Section 2.2), the sliding dynamics of F_{SR} and F_{RS} can be determined in Σ_{RR}. For F_{SS}, the theory of extended Filippov systems (Section 2.3) can be applied to determine the sliding dynamics in Σ_{SR} and Σ_{RS}, which are possibly not unique. To check the validity of the modelling by Filippov systems and extended Filippov systems, we have to ensure that the four vector fields $F_{\mathrm{SS}}, F_{\mathrm{SR}}, F_{\mathrm{RS}}$ and F_{RR} are compatible in the sense of calculating the sliding dynamics:

Definition 3.2 (Compatibility of the dynamics of the kinematic cases)**.** *The vector fields F_{SS}, F_{RS}, F_{SR} and F_{RR} are called **compatible** if the following requirements are satisfied:*

(a) The sliding dynamics of the extended Filippov system F_{SS} is uniquely defined in Σ_{SR}, and this sliding vector field equals to the vector field F_{SR}.

(b) The sliding dynamics of the extended Filippov system F_{SS} is uniquely defined in Σ_{RS}, and this sliding vector field equals to the vector field F_{RS}.

(c) The sliding vector field generated by the Filippov system F_{SR} in Σ_{RR} equals to the vector field F_{RR}.

(d) The sliding vector field generated by the Filippov system F_{RS} in Σ_{RR} equals to the vector field F_{RR}.

This property of the compatibility implies that the vector fields of the four kinematic cases are not independent from each other but the vector fields of Cases SR, RS and RR are generated by the dynamics of Case SS. The conjuncture of the author is that the compatibility is always ensured in the case of the Coulomb friction model. But in the lack of the exact proof, the compatibility conditions of Definition 3.2 should be checked in applications.

3.4.2 Double discontinuity at the intersection of discontinuites

Both the limit vector fields F_{SS}^{*+} and F_{SS}^{*-} are discontinuous in Σ_{RR}, where the two codimension-2 discontinuities Σ_{SR} and Σ_{RS} intersect each other. Instead of elaborating the theory of this degenerate case in details, only those concepts are presented briefly which are necessary for the subsequent analysis of this chapter.

We need the set of directions in the 3D space spanned by e_1^+, e_2^+ and e_a. Let us construct the set of unit vectors $\hat{n}(\phi^+, \phi^-)$ defined by

$$\begin{aligned} \langle \hat{n}(\phi^+, \phi^-), n(\phi^+ + \pi/2) \rangle &\equiv 0, \\ \langle \hat{n}(\phi^+, \phi^-), n(\phi^- + \pi/2) \rangle &\equiv 0, \\ \|\hat{n}(\phi^+, \phi^-)\| &\equiv 1, \end{aligned} \tag{3.39}$$

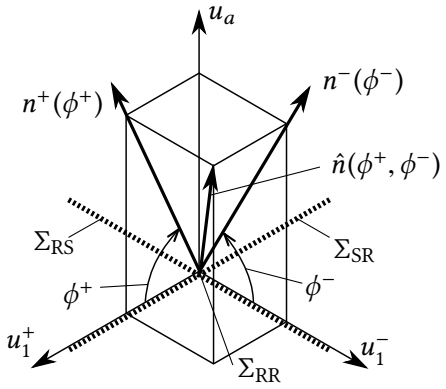

Figure 3.9: The definition of the set $\hat{n}(\phi^+, \phi^-)$ of unit vectors which are normal to Σ_{RR}. In the subspace of u_1^+, u_1^- and u_a, the vector $\hat{n}(\phi^+, \phi^-)$ gives the space diagonal of a cuboid whose face diagonals are parallel to $n^+(\phi^+)$ and $n^-(\phi^-)$.

where the ranges of the variables are

$$|\phi^+| \in (0, \pi), \qquad |\phi^-| \in (0, \pi), \qquad \operatorname{sgn} \sin \phi^+ = \operatorname{sgn} \sin \phi^-. \tag{3.40}$$

By this construction, the projection unit vector $\hat{n}(\phi^+, \phi^-)$ onto the plane spanned by e_1^+ and e_a is parallel to $n(\phi^+)$, and its projection onto the plane spanned by e_1^- and e_a is parallel to $n(\phi^-)$ (see Figure 3.9). In the special cases, we get

$$\hat{n}(\phi^+, \operatorname{sgn} \sin \phi^+ \cdot \pi/2) = n(\phi^+), \qquad \hat{n}(\operatorname{sgn} \sin \phi^- \cdot \pi/2, \phi^-) = n(\phi^-). \tag{3.41}$$

The constraint between the signs in (3.40) is required because (3.33) and (3.35) both have components in the direction e_a. The image of $\hat{n}$ on the domain (3.40) covers the unit sphere in the space spanned by e_1^+, e_1^- and e_a, except for the directions $\pm e_1^+$ and $\pm e_1^-$, which correspond to the directions of the discontinuity sets Σ_{RS} and Σ_{SR}, respectively.

As we did (2.18), we can define a *limit vector field* $\hat{F}^*_{SS}(\phi^+, \phi^-)$ in a point $x_0 \in \Sigma_{RR}$ by

$$\hat{F}^*_{SS}(\phi^+, \phi^-)(x_0) := \lim_{\epsilon \to 0^+} F_{SS}\left(x_0 + \epsilon \hat{n}^-(\phi^+, \phi^-)\right). \tag{3.42}$$

In a similar way as we did in (2.24), we can define

$$\begin{aligned} \hat{R}(\phi^+, \phi^-) &:= \left\langle \hat{F}^*_{SS}(\phi^+, \phi^-), \hat{n}(\phi^+, \phi^-) \right\rangle, \\ \hat{V}^+(\phi^+, \phi^-) &:= \left\langle \hat{F}^*_{SS}(\phi), n^+(\phi^+ + \pi/2) \right\rangle, \\ \hat{V}^-(\phi^+, \phi^-) &:= \left\langle \hat{F}^*_{SS}(\phi), n^-(\phi^- + \pi/2) \right\rangle. \end{aligned} \tag{3.43}$$

By considering the orthogonality conditions (3.40), the pair (ϕ_1^+, ϕ_1^-) is called a *limit direction* if $\hat{V}^+(\phi_1^+, \phi_1^-) = \hat{V}^-(\phi_1^+, \phi_1^-) = 0$, that is, if $\hat{F}^*_{SS}$ is parallel to $\hat{n}$. For a limit direction (ϕ_1^+, ϕ_1^-), the sign of $\hat{R}(\phi_1^+, \phi_1^-)$ determines if the limit direction is attracting or repelling. It can be shown that the attracting and repelling limit directions are related

to ω- and α-trajectories, respectively. As we defined in Definitions 2.12 and 2.13, the *sliding* and *crossing* behaviour can be discriminated and the boundary points are called the *tangency points*.

In the parametrisation (3.40), values 0 and π are missing, which correspond to the directions $\pm e_1^+$ and $\pm e_1^-$. These directions are tangent to the discontinuity sets Σ_{SR} and Σ_{RS}, and thus, they are related to slipping at only one of the contact points. To check these cases, the sliding or crossing properties of F_{SR} and F_{RS} are need to be investigated at Σ_{RR}, too.

3.4.3 Conditions of slipping and rolling

For systems which are compatible in the sense of Definition 3.2, we can state the following proposition, which summarises the possible types of behaviour according to the limit trajectories at Σ_{RR}:

Proposition 3.3. *Consider a mechanical system described by the vector fields F_{SS}, F_{SR}, F_{RS} and F_{RR} and a point $x_0 \in \Sigma_{RR}$. The evolution of the mechanical system from x_0 is determined*

(a) by F_{SS} if and only if x_0 possesses an α-trajectory with respect to F_{SS}, that is, there exists a repelling limit direction (ϕ_1^+, ϕ_1^-) with $\hat{V}^+(\phi_1^+, \phi_1^-) = \hat{V}^+(\phi_1^+, \phi_1^-) = 0$ and $\hat{R}(\phi_1^+, \phi_1^-) > 0$;

(b) by F_{SR} if and only if x_0 possesses an α-trajectory with respect to F_{SR} denoted by $\gamma : (0, t_1] \to \mathbb{R}^8$ with $\lim_{t\to 0^+} = x_0$; and there exists $0 < t_2 \leq t_1$ for that , $\gamma(t)$ is located in the attracting sliding region of Σ_{SR} with respect to F_{SS} for any $0 < t \leq t_2$;

(c) by F_{RS} if and only if x_0 possesses an α-trajectory with respect to F_{SR} denoted by $\gamma : (0, t_1] \to \mathbb{R}^8$ with $\lim_{t\to 0^+} = x_0$; and there exists $0 < t_2 \leq t_1$ for that , $\gamma(t)$ is located in the attracting sliding region of Σ_{RS} with respect to F_{SS} for any $0 < t \leq t_2$;

(d) by F_{RR}, otherwise.

In cases (a)-(c), the conditions of α-trajectories simply require the existence of trajectories that start from Σ_{RR} and escape to higher dimensional cases SR, RS or SS. In cases (b)-(c), condition of attracting sliding is required to exclude the cases when the body starts slipping at the other contact point, too. The compatibility conditions of Definition 3.2 guarantee that the vector fields are not independent and there are no ambiguous cases when more than one from (a)-(c) occurs at the same time. Case (d) shows that the dual-point rolling occurs only when there is no possibility for instantaneous slipping either at one of the contact points or at both contact points.

3.5 New results

Thesis Statement 3. Consider a rigid body in normal contact with two rigid surfaces by assuming Coulomb friction. At both contact points, slipping or rolling can occur, which leads to four kinematic cases of the body: dual-point slipping, dual-point rolling and two mixed slipping-rolling cases. In the case of dual-point rolling, the rolling constraints at the two contact points are not independent. Consequently, the contact forces are undetermined in the scope of rigid body dynamics, and thus, the conditions of slipping cannot be determined from the contact forces.

i) In case of dual-point slipping, the dynamics of the body leads to an extended Filippov system with two intersecting codimension-2 discontinuity manifolds. In each of the mixed slipping-rolling cases, the dynamics is given by a Filippov system, and it is restricted to one of these discontinuity sets. In case of dual-point rolling, the dynamics is restricted to the intersection of the two discontinuity manifolds.

Assume that the dynamics of the four kinematic cases of the body are compatible to each other in the sense that the dynamics of each lower dimensional system coincides with the sliding dynamics generated from the corresponding higher dimensional system.

ii) The analysis of the limit trajectories of slipping cases at the dual-point rolling submanifold shows whether there is a possibility to the transition from dual-point rolling to slipping cases. Therefore, the condition of slipping can be determined in the scope of the rigid body dynamics without the calculation of the contact forces.

Related publications: [3], [6], [7], [8], [10].

Chapter 4

Bifurcations of a rotating ball flowmeter

4.1 Introduction

One of the possible principles of flow rate measurement is placing a body into the fluid flow and measure the effect of the flow on the body. A possible construction of this idea is called *rotating ball flowmeter*, *cyclonic flowmeter* [21], or *orbital ball flowmeter* [57], which can be found in several accepted patents. The sketch of this flowmeter can be seen in Figure 4.2. The idea of the operation is the following: the fluid flow goes through a vessel, where the swirling of the flow is created by using e.g. tilted blades at the inlet. The swirling flow makes a metal ball move around the edge of the vessel with a dual-point rolling motion. The speed of the ball can be measured from outside the vessel by using e.g. an inductive sensor. After calibration, the device can be used for measuring the flow rate through the vessel.

The first appearance of this idea can be found in the patent of Kearsley [42] from 1950. Since then, many similar patents have been submitted (see [24, 34, 62, 75, 16, 21] and the recent patents of Peters [56, 57]). The usage of these devices are not widespread, they can be useful in highly contaminating environments (see [70], p. 165), because the motion of the ball provides a self-cleaning of the surfaces.

The dynamics of the ball in these flowmeters has not been investigated in the literature. In this chapter, the motivation is to determine the conditions of the slipping of the ball at the contact points and to analyse the consequences for the operation of the flowmeter. The objective of this project is not to obtain an accurate quantitative description of the device but to explore and understand the rolling-slipping transitions by analysing the simplest relevant model. For this purpose, the methods of Chapter 3 are applied because the ball is in a dual-point contact with the vessel, and slipping can occur at both contact points. The analysis of this chapter is based on the recently published paper of the candidate [7]. Similar analysis was presented in the conference papers [3] and [6].

	Notation	Meaning
model parameters	r	radius of the ball
	$d + r$	inner radius of the vessel
	m	mass of the ball
	$j \cdot m \cdot r^2$	mass moment of inertia of the ball ($j = 2/5$ for a solid sphere)
	g	reduced gravitational acceleration (including buoyancy)
	μ	friction coefficient between the ball and the vessel
	v_f	velocity of the flow around the circumference of the vessel
	$c \cdot m$	linear coefficient of drag force between the ball and the fluid
variables	v	velocity of the centre of the ball around the vessel
	u_1^+	slipping velocity at P^+ in the direction of the motion of the ball
	u_1^-	slipping velocity at P^- in the direction of the motion of the ball
	u_2	slipping velocities at P^+ and P^- perpendicular to the direction of the motion of the ball
bifurcations	$X_{\mathrm{RR}}, X_{\mathrm{RR}}, X_{\mathrm{RR}}, X_{\mathrm{RR}}$	stationary solutions in the four kinematic cases
	$v_{f,\mathrm{RR/SR}}$	value v_f at the transition between X_{RR} and X_{SR}
	$v_{f,\mathrm{RR/SS}}$	value v_f at the transition between X_{RR} and X_{SS}
	$v_{f,\mathrm{SR/SS}}$	value v_f at the transition between X_{SR} and X_{SS}
	$v_{f,\mathrm{fold}}$	value v_f at the fold bifurcation of X_{SS}
	μ_{fold}	value μ where the fold bifurcation disappears

Table 4.1: Important notations of Chapter 4. For further notations, see also Tables 2.1 and 3.1.

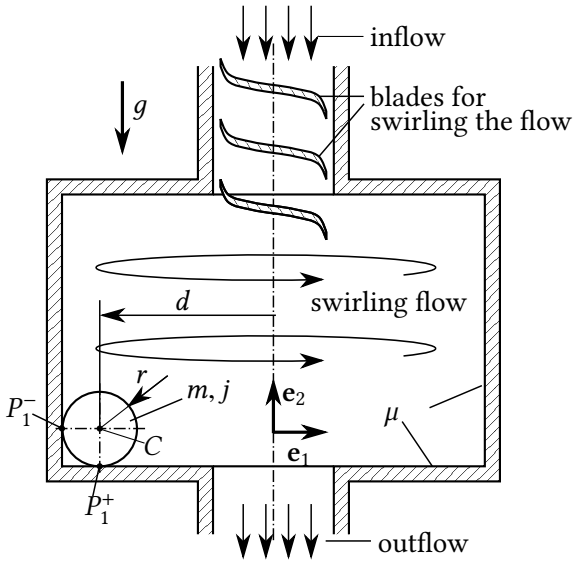

Figure 4.2: The sketch of a possible arrangement of the rotating ball flowmeter.

The structure of the chapter is the following: In Section 4.2, the mechanical model of the flowmeter is introduced and the equations of motion are derived. In Section 3.3, the dynamics of the possible slipping and rolling cases are presented and the nonsmooth system is investigated by using the tools of Chapter 3. In Section 4.4, the stationary solutions of the dynamical system are determined in the different kinematic cases, and the effect of the parameters are investigated. The new results are summarised in Section 4.5.

4.2 Mechanical model

Consider one of the simplest geometric arrangements of the rotating ball flowmeter when the ball is rolling along the edge of a cylindrical vessel (see Figure 4.2). This construction can be found e.g. in [21]. The radius of the ball is denoted by r, and the inner radius of the vessel is denoted by $d + r$. During the subsequent calculations, we apply the methods and notations presented in Chapter 3. The centre C of gravity is located in the geometric centre of the ball, P^+ denotes the contact point at the bottom of the vessel, and P^- refers to the contact point on the wall of the vessel.

4.2.1 Kinematics

For the description of the components of the vectors, we use a steady *reference system* fixed to the vessel, but a rotating *coordinate system* defined by the basis vectors $\mathbf{e}_1, \mathbf{e}_2$ and $\mathbf{e}_3$ (see Figures 4.2-4.3). The basis vector $\mathbf{e}_2$ is fixed and it points upwards into the direction of the axis of the vessel, while $\mathbf{e}_1$ and $\mathbf{e}_3$ are co-rotating with the motion of the centre of gravity of the ball. In this coordinate system, the location vectors $\mathbf{r}^+$, $\mathbf{r}^-$ of the contact points and the normal vectors $\mathbf{n}^+$, $\mathbf{n}^-$ do not depend on the state of the ball and they can be expressed in a simple form:

$$\mathbf{r}^+ = \begin{bmatrix} 0 \\ -r \\ 0 \end{bmatrix}, \qquad \mathbf{r}^- = \begin{bmatrix} -r \\ 0 \\ 0 \end{bmatrix}, \qquad \mathbf{n}^+ = \begin{bmatrix} 0 \\ 1 \\ 0 \end{bmatrix}, \qquad \mathbf{n}^- = \begin{bmatrix} 1 \\ 0 \\ 0 \end{bmatrix}. \tag{4.1}$$

The unit vector pointing to the direction of $\mathbf{r}^+ - \mathbf{r}^-$ becomes

$$\mathbf{a} = \begin{bmatrix} \sqrt{2}/2 \\ -\sqrt{2}/2 \\ 0 \end{bmatrix}. \tag{4.2}$$

Then, according to (3.3)-(3.4), the tangential unit vectors at the contact points P^+ and P^- become

$$\mathbf{t}_1^+ = \begin{bmatrix} 0 \\ 0 \\ 1 \end{bmatrix}, \qquad \mathbf{t}_2^+ = \begin{bmatrix} 1 \\ 0 \\ 0 \end{bmatrix}, \tag{4.3}$$

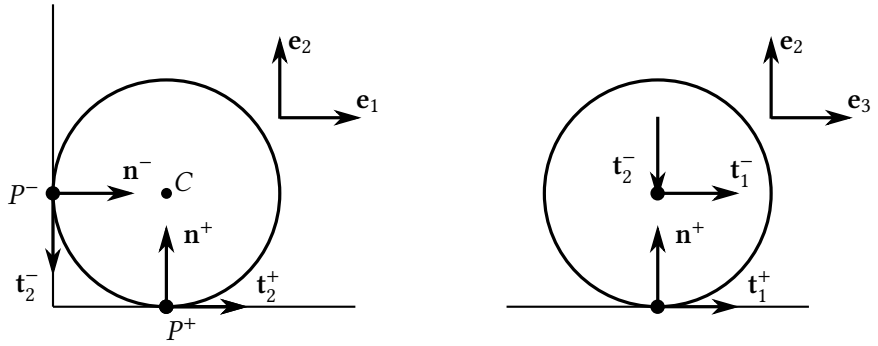

Figure 4.3: The basis vectors of the local coordinate systems at the contact points. Left panel: front view. Right panel: side view.

and

$$\mathbf{t}_1^- = \begin{bmatrix} 0 \\ 0 \\ 1 \end{bmatrix}, \qquad \mathbf{t}_2^- = \begin{bmatrix} 0 \\ -1 \\ 0 \end{bmatrix}, \tag{4.4}$$

respectively (see Figure 4.3).

The formula (3.8) gives $u_2^+ = u_2^-$, because we have $\left\langle \mathbf{t}_2^+, \mathbf{a} \right\rangle = \left\langle \mathbf{t}_2^-, \mathbf{a} \right\rangle = \sqrt{2}/2$. That is, there is no need for separate notations for u_2^+ and u_2^-, and we can introduce

$$u_2 := u_2^+ = u_2^-. \tag{4.5}$$

Then, the velocities of the contact points become

$$\mathbf{v}^+ = \begin{bmatrix} u_2 \\ 0 \\ u_1^+ \end{bmatrix}, \qquad \mathbf{v}^- = \begin{bmatrix} 0 \\ -u_2 \\ u_1^- \end{bmatrix}. \tag{4.6}$$

Due to the contact constraints, the velocity $\mathbf{v}_C$ of the centre C of gravity has a component only in the direction $\mathbf{e}_3$, which is denoted by v, and which shows the speed of the ball along the circumference of the vessel. The components of the angular velocity $\boldsymbol{\Omega}$ of the ball are denoted by Ω_w, Ω_y and Ω_z. Then, the velocity state of the ball is given by

$$\mathbf{v}_C = \begin{bmatrix} 0 \\ 0 \\ v \end{bmatrix}, \qquad \boldsymbol{\Omega} = \begin{bmatrix} \Omega_w \\ \Omega_y \\ \Omega_z \end{bmatrix}. \tag{4.7}$$

From these quantities, the velocities of the contact points can be expressed through

$$\begin{aligned} \mathbf{v}^+ &= \mathbf{v}_C + \boldsymbol{\Omega} \times \mathbf{r}^+, \\ \mathbf{v}^- &= \mathbf{v}_C + \boldsymbol{\Omega} \times \mathbf{r}^-. \end{aligned} \tag{4.8}$$

By comparing (4.6) and (4.8), the components of the angular velocity become

$$\Omega_w = \frac{v - u_1^+}{r}, \qquad \Omega_y = -\frac{v - u_1^-}{r}, \qquad \Omega_z = \frac{u_2}{r}. \tag{4.9}$$

Instead of the choice (3.14) of quasi-velocities in Chapter 3, we choose the variable set

$$s = [s_1, s_2, s_3, s_4] = [u_1^+, u_1^-, u_2, v], \tag{4.10}$$

because it provides simpler expressions in this model. According to (3.9) and (3.12), the relationship between the variables is determined by

$$u_a = \frac{\sqrt{2}}{2} u_2, \qquad \Omega_a = \frac{\sqrt{2}\, v}{r} - \frac{\sqrt{2}}{2r}(u_1^+ + u_1^-), \tag{4.11}$$

and the two sets of quasi-velocities are related by the linear transformation

$$\begin{bmatrix} u_1^+ \\ u_1^- \\ u_a \\ \Omega_a \end{bmatrix} = \begin{bmatrix} 1 & 0 & 0 & 0 \\ 0 & 1 & 0 & 0 \\ 0 & 0 & \sqrt{2}/2 & 0 \\ -\sqrt{2}/(2r) & -\sqrt{2}/(2r) & 0 & \sqrt{2}/r \end{bmatrix} \cdot \begin{bmatrix} u_1^+ \\ u_1^- \\ u_2 \\ v \end{bmatrix}. \tag{4.12}$$

Note that in [7], a further set of quasi-velocities is used, which is determined by (4.10) through

$$\begin{bmatrix} \Omega_{w,\mathrm{slip}} \\ \Omega_{y,\mathrm{slip}} \\ \Omega_z \\ v \end{bmatrix} = \begin{bmatrix} -1/r & 0 & 0 & 0 \\ 0 & 1/r & 0 & 0 \\ 0 & 0 & 1/r & 0 \\ 0 & 0 & 0 & 1 \end{bmatrix} \cdot \begin{bmatrix} u_1^+ \\ u_1^- \\ u_2 \\ v \end{bmatrix}. \tag{4.13}$$

The *slipping angular velocities* $\Omega_{w,\mathrm{slip}} := \Omega_w - v/r$ and $\Omega_{y,\mathrm{slip}} := \Omega_y + -v/r$ show the deviation of the components from dual-point rolling (compare (4.6) and (4.9)).

To derive the accelerations of the ball, the time derivations have to be carried out in the rotating coordinate system. For that, we need the angular velocity of the coordinate system, which is

$$\boldsymbol{\Omega}_{\mathrm{CS}} = \begin{bmatrix} 0 \\ v/d \\ 0 \end{bmatrix}, \tag{4.14}$$

because the centre of the ball is moving with a speed v along a circular path with a radius R (see Figure 4.2). The acceleration of the centre C of gravity becomes

$$\dot{\mathbf{v}}_C = \begin{bmatrix} 0 \\ 0 \\ \dot{v} \end{bmatrix} + \boldsymbol{\Omega}_{\mathrm{CS}} \times \mathbf{v}_C = \begin{bmatrix} v^2/d \\ 0 \\ \dot{v} \end{bmatrix}, \tag{4.15}$$

and the angular acceleration of the ball is

$$\dot{\boldsymbol{\Omega}} = \begin{bmatrix} \dot{\Omega}_w \\ \dot{\Omega}_y \\ \dot{\Omega}_z \end{bmatrix} + \boldsymbol{\Omega}_{\mathrm{CS}} \times \boldsymbol{\Omega} = \frac{1}{r} \cdot \begin{bmatrix} \dot{v} - \dot{u}_1^+ + v u_2/d \\ -\dot{v} + \dot{u}_1^- \\ \dot{u}_2 - v^2/d + v u_1^+/d \end{bmatrix}. \tag{4.16}$$

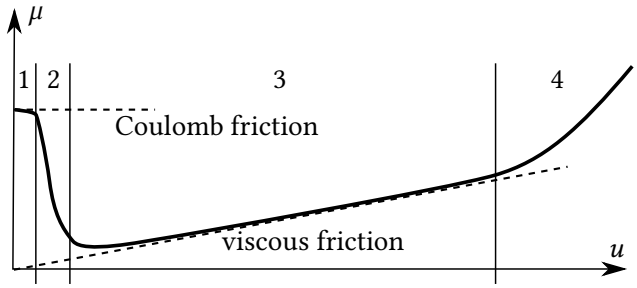

Figure 4.4: The friction coefficient plotted against the relative velocity in the presence of a lubricant. The figure is reproduced from [48], p. 761. The typical regimes of the curve are: 1: boundary lubrication, 2: mixed lubrication, 3: hydrodynamic lubrication, 4: superlaminar flow. Although the friction coefficient decreases due to the presence of the lubricant, the Coulomb friction model is still applicable for small relative velocities for determining the rolling-slipping transitions. Note that even for $u \to 0$, the *lubricated friction coefficient* can be significantly smaller than the friction coefficient without lubrication.

4.2.2 Dynamics

Assume that the mass of the ball is m and its mass moment of inertia is jmd^2. The value of the dimensionless mass moment of inertia j is $2/5$ for a solid sphere and its value is in the range $0 < j < 2/3$ for a non-homogeneous spherical symmetric mass distribution (e.g. if the ball has a core from a different material). By using the Newton-Euler equations, the equations of motions of the ball become

$$\begin{aligned} m\dot{\mathbf{v}}_C &= \mathbf{F}^+ + \mathbf{F}^- + \mathbf{F}_g + \mathbf{F}_{\text{fluid}}, \\ jmr^2\dot{\boldsymbol{\Omega}} &= \mathbf{r}^+ \times \mathbf{F}^+ + \mathbf{r}^- \times \mathbf{F}^- + \mathbf{M}_{\text{fluid}}, \end{aligned} \tag{4.17}$$

where $\mathbf{F}_g$ is the resultant force from gravity and buoyancy, $\mathbf{F}_{\text{fluid}}$ and $\mathbf{M}_{\text{fluid}}$ are the resultant force and torque from the effect of the fluid, and

$$\mathbf{F}^+ = \begin{bmatrix} T_2^+ \\ N^+ \\ T_1^+ \end{bmatrix}, \qquad \mathbf{F}^- = \begin{bmatrix} N^- \\ -T_2^- \\ T_1^- \end{bmatrix} \tag{4.18}$$

are the contact forces at P^+ and P^-, respectively (see (3.18)).

If the axis of the vessel is parallel to the direction of the gravity of the Earth then $\mathbf{F}_g$ becomes

$$\mathbf{F}_g = \begin{bmatrix} 0 \\ -mg \\ 0 \end{bmatrix} \tag{4.19}$$

where the g is the *reduced* gravitational acceleration including the buoyancy effect.

For modelling the contact between the ball and the vessel, Coulomb model (3.21)-(3.22) is assumed with a friction coefficient μ, which is a suitable assumption if the measured fluid is a gas. In case of liquids, the friction coefficient varies significantly with

the relative velocity of the surfaces, because the liquid behaves as a lubricant between the bodies (see Figure 4.4). However, the assumption of the Coulomb friction model is still valid for the regime of small relative velocities between the surfaces, which is called the state of *boundary lubrication* (see [48], p. 761). Hence, although the Coulomb friction model is inaccurate when modelling substantial slipping velocities in a liquid, it is appropriate when analysing the transitions between slipping and rolling.

The effect of the moving fluid on the ball is complicated and its accurate description would require the modelling of the flow field (see e.g. [61] and [46]). Instead, let us choose the simplest relevant model for the qualitative analysis of the problem. We consider the case when the fluid flows though the vessel with a constant mass flow rate. Then, it can be assumed that at a distance d from the centre of the vessel, the fluid is moving around the circumference with a constant speed v_f. That is, the velocity of the fluid at C is

$$\mathbf{v}_{C,\text{flow}} = \begin{bmatrix} 0 \\ 0 \\ v_f \end{bmatrix}. \tag{4.20}$$

Then, the effect of the fluid on the ball is modelled by a linear drag law in the form

$$\mathbf{F}_{\text{fluid}} = -c \cdot m \cdot (\mathbf{v}_C - \mathbf{v}_{C,\text{flow}}) = \begin{bmatrix} 0 \\ 0 \\ -cm(v - v_f) \end{bmatrix}. \tag{4.21}$$

This model contains several simplifications. The linear drag law is valid in case of a laminar flow, and it should be extended by adding a second-order term for high Reynolds numbers (see [59], p. 452). The resultant torque of the fluid (see [28], p. 42) and the force from the rotation of the ball (called *Magnus effect*, see [59], p. 474) is neglected, as well. For an accurate quantitative analysis of the flowmeter, these effects should be included in the model. However, the objective of the present analysis is to explore the rolling-slipping transitions caused by the Coulomb friction at the two contact points. *For this purpose, it is enough to assume that the drag force tries to eliminate the relative velocity between the ball and the flow.* It is important to emphasise that the effect of the fluid flow will appear explicitly only in (4.70), (4.71) and (4.74). All the other results are not affected by the choice of the model (4.21).

With these assumptions, the equation of motion (4.17) can be written in the form

$$\begin{aligned} mv^2/d &= T_2^+ + N^-, \\ 0 &= N^+ - T_2^- - mg, \\ m\dot{v} &= T_1^+ + T_1^- - cm(v - v_f), \\ jm\dot{v} - jm\dot{u}_1^+ + jmvu_2/d &= -T_1^+, \\ -jm\dot{v} + jm\dot{u}_1^- &= T_1^-, \\ jm\dot{u}_2 - jmv^2/d + jmvu_1^+/d &= T_2^+ + T_2^-. \end{aligned} \tag{4.22}$$

For the different kinematic cases, (4.22) is coupled to the corresponding rolling constraints (3.15)-(3.16) and the equations (3.21) of Coulomb friction (see Table 3.5).

4.3 Nonsmooth dynamics

4.3.1 Differential equations for the different cases

In the kinematic description, no generalised coordinates were introduced, and the dynamic equations (4.22) do not contain the location and the orientation of the ball. This is caused by the cylindrical symmetry of the system about the axis of the vessel and by the spherical symmetry of the ball. A set of appropriate generalised coordinates could be introduced, but they would be *cyclic* coordinates and they would not affect the dynamics of the other variables.

That is, the dynamics of the quasi-velocities can be analysed independently from the geometric state, and instead of the 8 dimensional state space (3.24), we consider the 4 dimensional state space

$$x = s = [u_1^+, u_1^-, u_2, v] \tag{4.23}$$

of quasi-velocities. As the variables u_a and u_2 differs only in a constant multiplier (see (4.11)), the discontinuity sets Σ_{SR}, Σ_{RS} and Σ_{RR} are the same as in Section 3.3.

Case SS In case of dual-point slipping, the expressions (3.27)-(3.28) of the tangential contact forces become

$$T_1^+ = -\mu N^+ \frac{u_1^+}{\sqrt{(u_1^+)^2 + u_2^2}}, \qquad T_2^+ = -\mu N^+ \frac{u_2}{\sqrt{(u_1^+)^2 + u_2^2}}, \tag{4.24}$$

and

$$T_1^- = -\mu N^- \frac{u_1^-}{\sqrt{(u_1^-)^2 + u_2^2}}, \qquad T_2^- = -\mu N^- \frac{u_2}{\sqrt{(u_1^-)^2 + u_2^2}}. \tag{4.25}$$

Then, the solution of (4.22) for the normal contact forces is

$$N^+ = m \cdot \frac{g - v^2/d \cdot \frac{\mu u_2}{\sqrt{(u_1^-)^2+u_2^2}}}{1 + \frac{\mu u_2}{\sqrt{(u_1^+)^2+u_2^2}} \cdot \frac{\mu u_2}{\sqrt{(u_1^-)^2+v_2^2}}}, \qquad N^- = m \cdot \frac{v^2/d + g \cdot \frac{\mu u_2}{\sqrt{(u_1^+)^2+v_2^2}}}{1 + \frac{\mu u_2}{\sqrt{(u_1^+)^2+v_2^2}} \cdot \frac{\mu u_2}{\sqrt{(u_1^-)^2+v_2^2}}}, \tag{4.26}$$

and the vector field becomes

$$F_{\mathrm{SS}}(x) = \begin{bmatrix} -c(v - v_f) + vu_2/d + \frac{1+j}{j} \cdot \frac{T_1^+}{m} + \frac{T_1^-}{m} \\ -c(v - v_f) + \frac{1+j}{j} \cdot \frac{T_1^-}{m} + \frac{T_1^+}{m} \\ v(v - u_1^+)/d + \frac{1}{j} \cdot \frac{T_2^+}{m} + \frac{1}{j} \cdot \frac{T_2^-}{m} \\ -c(v - v_f) + \frac{T_1^+}{m} + \frac{T_1^-}{m}. \end{bmatrix}. \tag{4.27}$$

The vector field F_{SS} is discontinuous in the codimension-2 discontinuity sets Σ_{SR} defined by $u_1^- = u_2 = 0$ and Σ_{RS} defined by $u_1^+ = u_2 = 0$. That is, (4.27) is an extended Filippov system.

Case SR If the ball is rolling on the wall, but it is slipping at the bottom of the vessel then the constraint $u_1^- = u_2 = 0$ is satisfied (see (3.15)). Then, (4.25) is not valid, and (4.24) becomes

$$T_1^+ = -\mu N^+ \operatorname{sgn} u_1^+, \qquad T_2^+ = 0. \tag{4.28}$$

Finally, the solution of (4.22) for the normal forces is

$$N^+ = mg - jmv(v - u_1^+)/d, \qquad N^- = mv^2/d, \tag{4.29}$$

and the dynamics becomes

$$F_{SR}(x) = \begin{bmatrix} -\frac{c}{1+j} \cdot (v - v_f) + \frac{1+2j}{j(1+j)} \cdot \frac{T_1^+}{m} \\ 0 \\ 0 \\ -\frac{c}{1+j} \cdot (v - v_f) + \frac{1}{1+j} \cdot \frac{T_1^+}{m} \end{bmatrix}. \tag{4.30}$$

The vector field F_{SR} restricted to Σ_{SR} is a Filippov system, and it is discontinuous at the codimension-1 discontinuity set Σ_{RR} defined by $u_1^+ = 0$.

Case RS In the rolling-slipping case, the constraint $u_1^+ = u_2 = 0$ causes that (4.24) is not valid and (4.25) becomes

$$T_1^- = -\mu N^- \operatorname{sgn} u_1^-, \qquad T_2^- = 0. \tag{4.31}$$

Then, the solution of (4.22) leads to

$$N^+ = mg, \qquad N^- = m(1 + j)v^2/d, \tag{4.32}$$

$$F_{RS}(x) = \begin{bmatrix} 0 \\ -\frac{c}{1+j} \cdot (v - v_f) + \frac{1+2j}{j(1+j)} \cdot \frac{T_1^-}{m} \\ 0 \\ -\frac{c}{1+j} \cdot (v - v_f) + \frac{1}{1+j} \cdot \frac{T_1^-}{m} \end{bmatrix}. \tag{4.33}$$

The vector field F_{SR} is a Filippov system in Σ_{SR} , and it has a codimension-1 discontinuity set Σ_{RR} defined by $u_1^- = 0$.

Case RR In case of dual-point rolling, the rolling constraints (3.15)-(3.16) are both valid and $u_1^+ = u_1^- = u_2 = 0$. Then, (4.22) leads to

$$F_{\mathrm{RR}}(x) = \begin{bmatrix} 0 \\ 0 \\ 0 \\ -\frac{c}{1+2j} \cdot (v - v_f) \end{bmatrix}, \tag{4.34}$$

The vector field F_{RR} is a smooth dynamical system in Σ_{RR}. Note that in this case, the contact forces are undetermined (see Section 3.3).

4.3.2 Compatibility of the dynamics of the different cases

Let us check if the vector fields for the different kinematic cases are compatible in the sense of Definition 3.2.

Case SR as the sliding dynamics of Case SS Consider the vector field F_{SS} and the discontinuity at $u_1^- = u_2 = 0$ caused by the Coulomb friction between the ball and the bottom of the vessel. Due to the transformation $u_a \to u_2$ in (4.11), the unit vectors in (3.33) become

$$e_1^- = \begin{bmatrix} 0 \\ 1 \\ 0 \\ 0 \end{bmatrix}, \qquad e_2 = \begin{bmatrix} 0 \\ 0 \\ 1 \\ 0 \end{bmatrix}, \tag{4.35}$$

and then, the set of unit vectors normal to Σ_{SR} is given by

$$n^-(\phi^-) = \begin{bmatrix} 0 \\ \cos\phi^- \\ \sin\phi^- \\ 0 \end{bmatrix}. \tag{4.36}$$

When calculating the limit vector field according to (3.34), the discontinuous terms in (4.24)-(4.25) tend to

$$\frac{u_1^+}{\sqrt{(u_1^+)^2 + u_2^2}} \to \operatorname{sgn} u_1^+, \qquad \frac{u_2}{\sqrt{(u_1^+)^2 + u_2^2}} \to 0. \tag{4.37}$$

$$\frac{u_1^-}{\sqrt{(u_1^-)^2 + u_2^2}} \to \cos\phi^-, \qquad \frac{u_2}{\sqrt{(u_1^-)^2 + u_2^2}} \to \sin\phi^-. \tag{4.38}$$

Then, the expressions (4.26) for the normal forces become

$$N^+ = mg - mv^2/d \cdot \mu \sin\phi^-, \qquad N^- = mv^2/d, \tag{4.39}$$

and the limit vector field at a point $x_0 \in \Sigma_{\mathrm{SR}}$ is given by

$$F_{\mathrm{SS}}^{*-}(x_0)(\phi^-) = \begin{bmatrix} -c(v - v_f) + \frac{1+j}{j} \cdot \frac{T_1^+}{m} + \frac{T_1^-}{m} \\ -c(v - v_f) + \frac{1+j}{j} \cdot \frac{T_1^-}{m} + \frac{T_1^+}{m} \\ v(v - u_1^+)/d + \frac{1}{j} \cdot \frac{T_2^-}{m} \\ -c(v - v_f) + \frac{T_1^+}{m} + \frac{T_1^-}{m} \end{bmatrix}, \tag{4.40}$$

where the tangential forces are determined by (4.24)-(4.25) and (4.37)-(4.38).

The limit vector field (4.40) can be written into the form (2.28) with

$$\overline{F} = \begin{bmatrix} -c(v - v_f) - \frac{1+j}{j}\mu g \operatorname{sgn} u_1^+ \\ -c(v - v_f) - \mu g \operatorname{sgn} u_1^+ \\ v(v - u_1^+)/d \\ -c(v - v_f) - \mu g \operatorname{sgn} u_1^+ \end{bmatrix}, \tag{4.41}$$

$$F_A = \begin{bmatrix} -\mu v^2/d \\ -\frac{1+j}{j}\mu v^2/d \\ 0 \\ -\mu v^2/d \end{bmatrix}, \qquad F_B = \begin{bmatrix} \frac{1+j}{j}\mu^2 v^2/d \cdot \operatorname{sgn}(u_1^+) \\ \mu^2 v^2/d \cdot \operatorname{sgn} u_1^+ \\ -\frac{1}{j} \cdot \mu v^2/d \\ \mu^2 v^2/d \cdot \operatorname{sgn} u_1^+ \end{bmatrix}. \tag{4.42}$$

Then, Theorem 2.17 guarantees the uniqueness of the sliding dynamics. By direct calculation, the coefficients of (2.32) proves to be

$$\begin{aligned} a &= \frac{-c(v - v_f) - \mu g \operatorname{sgn} u_1^+ + j\mu v(v - u_1^+) \operatorname{sgn} u_1^+/d}{\frac{1+j}{j}\mu v^2/d}, \\ b &= \frac{v(v - u_1^+)/d}{\frac{1}{j}\mu v^2/d}. \end{aligned} \tag{4.43}$$

Finally, according to (2.32), the sliding vector is given by $F_s = \overline{F} + aF_A + bF_B$. It can be checked that this sliding vector field computed from F_{SS} coincides with the vector field F_{SR} of the sliding-rolling case in (4.30). That is, condition (a) in Definition 3.2 is satisfied.

Case RS as the sliding dynamics of Case SS The condition (b) of Definition 3.2 can be checked by considering the discontinuity $u_1^+ = u_2 = 0$ of F_{SS} caused by the Coulomb friction on the bottom of the vessel. Then, (3.35) gives

$$e_1^+ = \begin{bmatrix} 1 \\ 0 \\ 0 \\ 0 \end{bmatrix}, \qquad e_2 = \begin{bmatrix} 0 \\ 0 \\ 1 \\ 0 \end{bmatrix}, \qquad n^-(\phi^-) = \begin{bmatrix} \cos\phi^+ \\ 0 \\ \sin\phi^+ \\ 0 \end{bmatrix}. \tag{4.44}$$

By calculating the limit in (3.36), the discontinuous terms in (4.24)-(4.25) become

$$\frac{u_1^+}{\sqrt{(u_1^+)^2 + u_2^2}} \to \cos\phi^+, \qquad \frac{u_2}{\sqrt{(u_1^+)^2 + u_2^2}} \to \sin\phi^+. \tag{4.45}$$

$$\frac{u_1^-}{\sqrt{(u_1^-)^2 + u_2^2}} \to \operatorname{sgn} u_1^-, \qquad \frac{u_2}{\sqrt{(u_1^-)^2 + u_2^2}} \to 0, \tag{4.46}$$

and the normal forces (4.26) are given by

$$N^+ = mg, \qquad N^- = mv^2/d + mg\mu\sin\phi^+. \tag{4.47}$$

Then, at a point $x_0 \in \Sigma_{RS}$, we obtain the limit vector field

$$F_{SS}^{*+}(x_0)(\phi^+) = \begin{bmatrix} -c(v - v_f) + \frac{1+j}{j} \cdot \frac{T_1^+}{m} + \frac{T_1^-}{m} \\ -c(v - v_f) + \frac{1+j}{j} \cdot \frac{T_1^-}{m} + \frac{T_1^+}{m} \\ v^2/d + \frac{1}{j} \cdot \frac{T_2^+}{m} \\ -c(v - v_f) + \frac{T_1^+}{m} + \frac{T_1^-}{m} \end{bmatrix}, \tag{4.48}$$

where the tangential forces are given by (4.24)-(4.25) and (4.45)-(4.46). By using similar steps as we did with (4.41), it can be checked by direct calculation that the sliding vector field generated by (4.48) coincides with the vector field (4.33) of Case RS.

Case RR as the sliding dynamics of Cases SR and RS Conditions (c)-(d) can be checked by the methods of Filippov systems. This is presented briefly for the discontinuity Σ_{RR} of F_{SR}.

In (2.10), F_1 and F_2 are equals to F_{SR} in (4.30) by assuming $u_1^+ > 0$ and $u_1^+ < 0$, respectively. The normal vectors are $n_1 = e_1^+$ and $n_2 = -e_1^+$. Then, the weights α_1 and α_2 are given by

$$\begin{aligned} \alpha_1 &= \frac{\frac{c}{1+j} \cdot (v - v_f) - \mu\frac{1+2j}{j(1+j)} \cdot (g - jv^2/d)}{-2\mu\frac{1+2j}{j(1+j)} \cdot (g - jv^2/d)}, \\ \alpha_2 &= \frac{-\frac{c}{1+j} \cdot (v - v_f) - \mu\frac{1+2j}{j(1+j)} \cdot (g - jv^2/d)}{-2\mu\frac{1+2j}{j(1+j)} \cdot (g - jv^2/d)}. \end{aligned} \tag{4.49}$$

Finally, the sliding dynamics from the formula (2.9) coincides with the dynamics (4.34) of the dual-point rolling case.

By carrying out the same calculations, it can be checked, as well, that the sliding dynamics generated by F_{RS} on Σ_{RR} coincides with F_{RR}. That is, all the conditions from Definition 3.2 are satisfied and the vector fields $F_{\mathrm{SS}}, F_{\mathrm{SR}}, F_{\mathrm{RS}}$ and F_{RR} are compatible. Hence, Proposition 3.3 can be used to determine the conditions of slipping in case of dual-point rolling.

4.4 Analysis of stationary solutions

The operation of the flowmeter is based on the stationary states of the ball: It is assumed that for a stationary flow through the flowmeter, the ball should move around the edge of the vessel with a constant speed. In this section, the possible stationary states of the ball are determined, which are the equilibrium points of the vector fields $F_{\mathrm{SS}}, F_{\mathrm{SR}}, F_{\mathrm{RS}}$ and F_{RR} of the four kinematic cases. In these states, the ball is running along the edge of the vessel with a constant speed and its angular velocity is constant in the coordinate system defined by $\mathbf{e}_1, \mathbf{e}_2$ and $\mathbf{e}_3$. We focus on the effect of the parameter v_f of the flow around the circumference of the vessel (see (4.20)), which is related to the mass flow rate through the flowmeter.

4.4.1 Stationary solution of the rolling-rolling case

In case of dual-point rolling, the system (4.34) has a single stationary state $x \equiv X_{\mathrm{RR}}$ with

$$X_{\mathrm{RR}}(v_f) = \begin{bmatrix} 0 \\ 0 \\ 0 \\ v_f \end{bmatrix}. \tag{4.50}$$

In this stationary state, the ball is moving with the same speed v_f as the surrounding flow. It can be checked that X_{RR} is an asymptotically stable equilibrium of F_{RR}, and for any initial condition, the speed v of the ball converges to v_f. This behaviour results in a favourable operation of the flowmeter: for a (slow) change of the parameter v_f, the ball follows the velocity of the flow.

However, this behaviour is not realizable if the ball starts slipping at one or both contact points. The contact forces are undetermined in Case RR, but the conditions of slipping can be determined by Proposition 3.3.

Transition to Case SR To check the case (b) of Proposition 3.3, let us evaluate (4.30) at $x = X_{\mathrm{RR}}$ to determine whether X_{RR} has an α-trajectory of F_{SR}. Then, we obtain

$$F_{\mathrm{SR}}(X_{\mathrm{RR}}) = \begin{bmatrix} -\frac{1+2j}{j(1+j)} \cdot \mu(g - jv_f^2/d)\operatorname{sgn} u_1^+ \\ 0 \\ 0 \\ -\frac{1}{1+j} \cdot \mu(g - jv_f^2/d)\operatorname{sgn} u_1^+ \end{bmatrix}, \tag{4.51}$$

It can be checked from Definition 2.2 that for

$$v_f < v_{f,\mathrm{RR/SR}} := \sqrt{\frac{gd}{j}}, \tag{4.52}$$

the equilibrium X_{RR} is located in the attracting sliding region of Σ_{RR} with no α-trajectories and for $v_f > v_{f,\mathrm{RR/SR}}$, the equilibrium is located in the repelling sliding region of Σ_{RR} with two α-trajectories. In borderline case $v_f = v_{f,\mathrm{RR/SR}}$, the equilibrium becomes

$$X_{\mathrm{RR/SR}} := X_{\mathrm{RR}}(v_{f,\mathrm{RR/SR}}) = \begin{bmatrix} 0 \\ 0 \\ 0 \\ \sqrt{gd/j} \end{bmatrix}. \tag{4.53}$$

That is, for $v_f > v_{f,\mathrm{RR/SR}}$, the ball possibly starts slipping at the point on the bottom of the vessel. To determine if there is no slipping at the other contact point, let us check the second condition of (b) of Proposition 3.3. By direct calculation, we get

$$F^{*-}(X_{\mathrm{RR/SR}})(\phi^-) = \begin{bmatrix} -\frac{1+j}{j} \cdot (g - \mu g/j \cdot \sin\phi^-) \cdot \mu\operatorname{sgn} u_1^+ - \mu g/j \cdot \cos\phi^- \\ -\frac{1+j}{j} \cdot \mu g/j \cdot \cos\phi^- + (g - \mu g/j \cdot \sin\phi^-) \cdot \mu\operatorname{sgn} u_1^+ \\ g/j - \frac{1}{j}\mu g/j \cdot \sin\phi^- \\ (g - \mu g/j \cdot \sin\phi^-) \cdot \mu\operatorname{sgn} u_1^+ - \mu g/j \cdot \cos\phi^- \end{bmatrix}. \tag{4.54}$$

In the general case, the limit directions of (4.54) cannot be determined analytically. However, we can find the neutral limit directions by assuming $R(\phi) = V(\phi) = 0$ (see Definition 2.14). This condition is equivalent to $\left\langle e_1^-, F^{*-}(\phi^-)\right\rangle = \langle e_2, F^{*-}(\phi^-)\rangle = 0$, which leads to

$$\phi^- = \pi/2, \qquad\qquad j = \mu. \tag{4.55}$$

It can be checked, that for $\mu < j$, the point $X_{\mathrm{RR/SR}}$ is located in the crossing region of Σ_{RS}, and thus, the transition from Case RR to Case SR is not possible. However, in the case $\mu > j$, $X_{\mathrm{RR/SR}}$ is in the attracting sliding region, and the conditions of (b) of Proposition 3.3 are satisfied.

One still have to ensure the non-negativeness of the normal forces at the transition. By substituting (4.53) into (4.29), we get $N^+ = 0$ and $N^- > 0$, which is still acceptable. Finally, we can summarise the result in the following statement:

Proposition 4.1. *If $\mu > j$ then the existence of the stationary solution* (4.50) *is limited by the condition $v_f \le \sqrt{gd/j}$ due to the slipping of the ball on the bottom of the vessel.*

Transition to Case RS Case (c) of Proposition 3.3 can be checked by evaluating (4.33) at $x = X_{\mathrm{RR}}$, and we obtain

$$F_{\mathrm{RS}}(X_{\mathrm{RR}}) = \begin{bmatrix} 0 \\ -\frac{1+2j}{j(1+j)} \cdot \mu(1+j)v_f^2/d \cdot \operatorname{sgn} u_1^- \\ 0 \\ -\frac{1}{1+j} \cdot \mu(1+j)v_f^2/d \cdot \operatorname{sgn} u_1^- \end{bmatrix}. \tag{4.56}$$

According to Definition 2.2, it can be calculated that X_{RR} is in the attracting sliding region if

$$v_f^2 > 0, \tag{4.57}$$

and then, there is no α-trajectories of X_{RR}. In the limit case $v_f = 0$, the vector $F_{\mathrm{RS}}(X_{\mathrm{RR}}) = 0$ vanishes, and thus, there is no limit trajectory, again. Consequently, there is no possibility for transition from Case RR to Case RS when the ball is in the stationary state X_{RR}.

Transition to Case SS Consider case (a) of Proposition 3.3 when the ball starts slipping at both contact points. Then, the vector field (3.42) at $x = X_{\mathrm{RR}}$ becomes

$$\hat{F}^*(\phi^+, \phi^-)(X_{\mathrm{RR}}) = \begin{bmatrix} \frac{1+j}{j} \cdot \frac{T_1^+}{m} + \frac{T_1^-}{m} \\ \frac{1+j}{j} \cdot \frac{T_1^-}{m} + \frac{T_1^+}{m} \\ v_f^2/d + \frac{1}{j} \cdot \frac{T_2^+}{m} + \frac{1}{j} \cdot \frac{T_2^-}{m} \\ \frac{T_1^+}{m} + \frac{T_1^-}{m} \end{bmatrix}, \tag{4.58}$$

where the normal forces are

$$N^+ = m \cdot \frac{g - v_f^2/d \cdot \mu \sin\phi^-}{1 + \mu^2 \sin\phi^+ \sin\phi^-}, \qquad N^- = m \cdot \frac{v_f^2/d + g \cdot \mu \sin\phi^+}{1 + \mu^2 \sin\phi^+ \sin\phi^-}, \tag{4.59}$$

and the tangential forces can be calculated according to (4.24)-(4.25), (4.38) and (4.45). The limit directions of (4.58) cannot be expressed analytically, but in the boundary case of neutral limit direction, we can check the condition $\hat{R}(\phi) = \hat{V}^+(\phi) = \hat{V}^-(\phi) = 0$ (see (3.43)). This condition is equivalent to

$$\left\langle e_1^+, \hat{F}^*(\phi^+, \phi^-) \right\rangle = \left\langle e_1^-, \hat{F}^*(\phi^+, \phi^-) \right\rangle = \left\langle e_2, \hat{F}^*(\phi^+, \phi^-) \right\rangle = 0, \tag{4.60}$$

which results in

$$\phi^+ = \phi^- = \pm\pi/2 \tag{4.61}$$

and

$$\frac{v_f^2}{d} - \frac{\mu}{j} \cdot \frac{g \mp v_f^2/d \cdot \mu}{1+\mu^2} - \frac{\mu}{j} \cdot \frac{v_f^2/d \pm g \cdot \mu}{1+\mu^2} = 0. \tag{4.62}$$

The ± sign in (4.62) refers to the two cases of $\phi = \pi/2$ and $\phi = -\pi/2$, respectively, which leads to two different critical values

$$v_{f,\mathrm{RR/SS}} := \sqrt{\frac{gd}{\mu}} \cdot \sqrt{\frac{\mu^2(\mu+1)}{\mu^2(j+1)+j-\mu}} \tag{4.63}$$

and

$$\tilde{v}_{f,\mathrm{RR/SS}} := \sqrt{\frac{gd}{\mu}} \cdot \sqrt{\frac{-\mu^2(\mu-1)}{\mu^2(j+1)+j+\mu}}. \tag{4.64}$$

It can be checked that for $\tilde{v}_{f,\mathrm{RR/SS}} < v_f < v_{f,\mathrm{RR/SS}}$, there is no α-trajectory of F_{SS}, and an α-trajectory appears on the boundaries of the interval in the directions $\phi = \pm\pi/2$.

The requirement of non-negativeness of the contact forces (4.59) gives that for $\tilde{v}_{f,\mathrm{RR/SS}}$, the component N^+ is always negative, that is, this case is irrelevant. For $v_{f,\mathrm{RR/SS}}$ the non-negativeness of N^+ and N^- is ensured for $\mu < j$, and N^+ becomes negative for $\mu > j$. For subsequent calculations, let us define $X_{\mathrm{RR/SS}} := X(v_{f,\mathrm{RR/SS}})$. We can state the following proposition:

Proposition 4.2. *If $\mu < j$ then the existence of the stationary solution* (4.50) *is limited by the condition $v_f \le v_{f,\mathrm{RR/SS}}$ due to the slipping of the ball simultaneuosly at both contact points.*

4.4.2 Stationary solutions of the other cases

Case SR In the slipping-rolling case (4.30), the stationary solution of F_{SR} is

$$X_{\mathrm{SR}}(v_f) := \begin{bmatrix} v_f - \frac{gd}{jv_f} \\ 0 \\ 0 \\ v_f \end{bmatrix}. \tag{4.65}$$

It can be shown by linear stability analysis that (4.65) is asymptotically stable for $v_f > v_{f,\mathrm{RR/SR}}$ and it is unstable for $v_f < v_{f,\mathrm{RR/SR}}$.

In the stationary state X_{SR}, the condition of slipping can be checked either by determining whether X_{SR} has an α-trajectory of F_{SS}, or by checking (3.22) directly. By both methods, we get that there is no transition from Case SR to Case SS if

$$v_f > v_{f,\mathrm{SR/SS}} := \sqrt{\frac{gd}{\mu}}. \tag{4.66}$$

In the limit case, we can define $X_{\mathrm{SR/SS}} := X_{\mathrm{SR}}(v_{f,\mathrm{SR/SS}})$. The results are summarized in the following proposition:

Proposition 4.3. *The existence of the stationary solution* (4.65) *is limited by the condition $v_f \ge \sqrt{gd/\mu}$ due to the slipping of the ball on the wall of the vessel.*

Case RS In the rolling-slipping case (4.33), a stationary solution exists only when $v_f = 0$, and then,

$$X_{\mathrm{RS}} = \begin{bmatrix} 0 \\ u_1^- \\ 0 \\ 0 \end{bmatrix} \tag{4.67}$$

for every $u_1^- \in \mathbb{R}$. That is, for $v_f = 0$, there is not a single stationary solution but a one-parameter family of stationary solutions. In the state of (4.67), there is no fluid flow; the ball is not moving but it is spinning on the bottom of the vessel with a constant angular velocity. It can be checked that (4.67) is stable but not asymptotically stable, and there is a zero eigenvalue with the eigenvector e_1^-. It can be checked from calculating the tangential forces that in the stationary state, there is no transition from Case RS to SS.

Case SS In case of dual-point slipping, the stationary solution of (4.27) exists only if $\mu < j$, and it can be written in the form

$$X_{\mathrm{SS}}(\varphi) = \begin{bmatrix} v_1^+(\varphi) \\ 0 \\ v_2(\varphi) \\ v(\varphi) \end{bmatrix}, \qquad 0 \le \varphi < \pi/2, \tag{4.68}$$

where

$$\begin{aligned} v(\varphi) &= \sqrt{gd\mu}\sqrt{\frac{1+\mu\sin^2\varphi}{\mu^2(1+j\sin^2\varphi)+(j-\mu)\sin\varphi}}, \\ v_1^+(\varphi) &= -\frac{gd\mu^2}{jv(\varphi)} \cdot \frac{-(j-\mu)\cos\varphi}{\mu^2(1+j\sin^2\varphi)+(j-\mu)\sin\varphi} \cdot \cos\varphi, \\ v_2(\varphi) &= -\frac{gd\mu^2}{jv(\varphi)} \cdot \frac{-(j-\mu)\cos\varphi}{\mu^2(1+j\sin^2\varphi)+(j-\mu)\sin\varphi} \cdot \sin\varphi. \end{aligned} \tag{4.69}$$

The velocity v_f of the flow can be expressed by the auxiliary parameter φ in the form

$$v_f(\varphi) = v(\varphi) + \frac{g\mu}{c} \cdot \frac{-(j-\mu)\sin\varphi\cos\varphi}{\mu^2(1+j\sin^2\varphi)+(j-\mu)\sin\varphi}. \tag{4.70}$$

Then (4.69)-(4.70) gives the dependence of (4.68) on v_f, but the explicit dependence $X_{\mathrm{SS}}(v_f)$ cannot be expressed analytically. The special cases of (4.68) give

$$X_{\mathrm{SS}}(-\pi/2) = X_{\mathrm{RR/SS}}, \qquad X_{\mathrm{SR}}(0) = X_{\mathrm{SR/SS}}. \tag{4.71}$$

The function $v_f(\varphi)$ is necessarily monotonous, and there can exist two stationary solutions for some values of v_f. The special point defined by

$$\frac{\mathrm{d}v_f}{\mathrm{d}\varphi}(\varphi_{\mathrm{fold}}) = 0 \tag{4.72}$$

corresponds to a fold (saddle-node) bifurcation, and the corresponding stationary solution is

$$X_{\mathrm{SS,fold}} := X_{\mathrm{SS}}(\varphi_{\mathrm{fold}}) \qquad \text{at} \qquad v_{f,\mathrm{fold}} := v(\varphi_{\mathrm{fold}}). \tag{4.73}$$

The existence of the fold bifurcation depends on the value of μ compared to the critical value

$$\mu_{\mathrm{fold}} := \sqrt[3]{\frac{c^2 d}{4g}}. \tag{4.74}$$

It can be shown that for $\mu < \mu_{\mathrm{fold}}$, there is no fold bifurcation but there is a single stationary solution X_{SS} for all $v_{f,\mathrm{RR/SS}} \le v_f \le v_{f,\mathrm{SR/SS}}$, which is asymptotically stable (see Figure 4.5). In the case $\mu_{\mathrm{fold}} < \mu < j$, there is a single asymptotically stable stationary solution for $v_{f,\mathrm{RR/SS}} \le v \le v_{f,\mathrm{SR/SS}}$ and there is a pair of stable and unstable stationary solutions for $v_{f,\mathrm{SR/SS}} \le v \le v_{f,\mathrm{fold}}$ (see Figure 4.6).

4.4.3 Bifurcation diagrams

From the viewpoint of the operation of the flowmeter, the most important parameter is the velocity v_f of the fluid flow, which is related to the flow rate through the device. Hence, the stationary solutions are analysed by the use of bifurcation diagrams plotted against v_f.

The stationary solutions are located in the 4 dimensional phase space, thus, an appropriate projection is necessary for the visualization in the bifurcation diagrams. Plotting the v component of the solutions would cause overlapping between some branches of solutions (see Figure 4.10). Therefore, consider the variable Ω_w from (4.9), which denotes the angular velocity of the ball around the axis normal to the wall of the vessel.

The value of the friction coefficient μ creates three different cases of bifurcation diagrams, which can be seen in Figures 4.5-4.7. If the stationary solutions are plotted in case of $\mu < \mu_{\mathrm{fold}}$, we get the diagram in Figure 4.5. In this case, the solution X_{RR} of the dual-point rolling exists for low values of v_f. By increasing the flow velocity to $v_{f,\mathrm{RR/SS}}$, there is a transition of the stationary solution to X_{SS}, and the ball starts slipping at both contact points. Based on the term *persistence bifurcation* of Filippov systems (see [19], p. 221), we can call this bifurcation a *codimension-3 persistence bifurcation*, because Σ_{RR} is a codimension-3 discontinuity set of the system. This bifurcation is denoted by P3 in the diagrams. By increasing v_f further to $v_{f,\mathrm{SR/SS}}$, the stationary solution turns into X_{SR}, and the ball starts rolling on the wall while it is still slipping on the bottom of the vessel. This bifurcation is called a *codimension-2 persistence bifurcation* (denoted by P2), because Σ_{SR} is a codimension-2 discontinuity set of F_{SS}.

If the friction coefficient is in the range $\mu_{\mathrm{fold}} < \mu < j$ then we get the diagram in Figure 4.6. The persistence bifurcation (P3) still exists at $v_{f,\mathrm{RR/SS}}$, but there are changes in the diagram due to the appearance of the two co-existing stationary solutions of Case SS. At $v_f = v_{f,\mathrm{fold}}$, there is a simple fold bifurcation between the two branches of X_{SS}

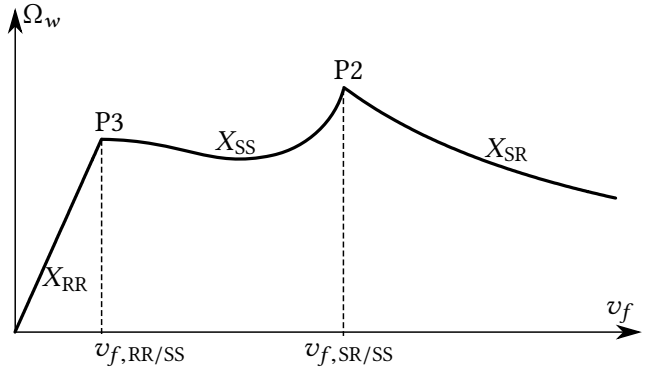

Figure 4.5: Bifurcation diagram of the system for $\mu < \mu_{fold}$.

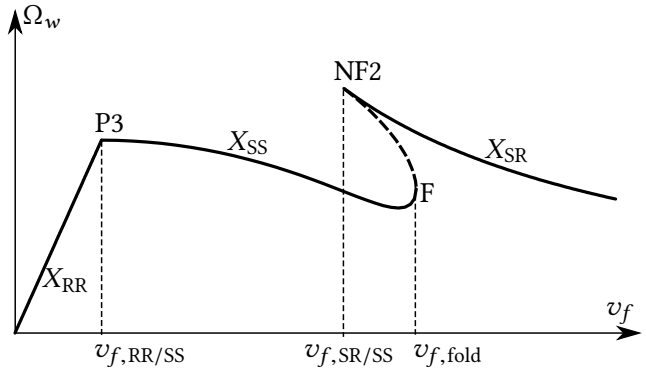

Figure 4.6: Bifurcation diagram of the system for $\mu_{fold} < \mu < j$.

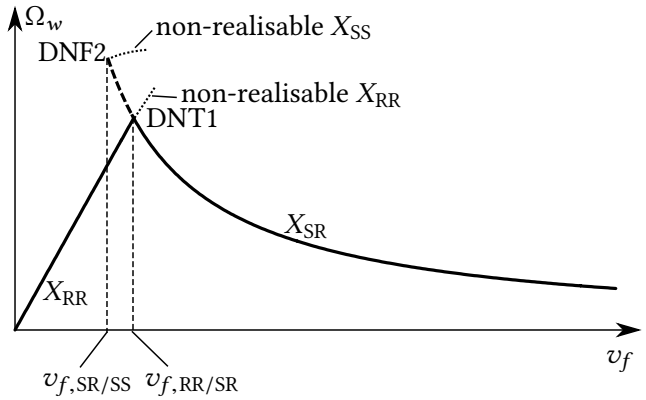

Figure 4.7: Bifurcation diagram of the system for $j < \mu$.

Acronym	Bifurcation	Value of v_f	condition
P3	codimension-3 persistence	$v_{f,\mathrm{RR/SS}}$	$\mu < j$
DNT1	degenerate nonsmooth transcritical bifrucation	$v_{f,\mathrm{RR/SR}}$	$j < \mu$
P2	codimension-2 persistence	$v_{f,\mathrm{SR/SS}}$	$\mu < \mu_{\mathrm{fold}}$
NF2	codimension-2 nonsmooth fold	$v_{f,\mathrm{SR/SS}}$	$\mu_{\mathrm{fold}} < \mu < j$
DNF2	degenerate codimension-2 nonsmooth fold	$v_{f,\mathrm{SR/SS}}$	$j < \mu$
F	fold	$v_{f,\mathrm{fold}}$	$\mu_{\mathrm{fold}} < \mu < j$

Table 4.8: The list of bifurcations of the system (see also Figures 4.5-4.7).

(denoted by F). At $v_{f,\mathrm{SR/SS}}$, there is no more a persistence bifurcation but a *codimension-2 nonsmooth fold* appears (denoted by NF2), where the unstable branch of X_{SS} (denoted by a dashed line) is connected to X_{SR}. These bifurcations lead to a hysteresis effect: if v_f is increasing then the solution X_{SS} turns into X_{SR} at the fold F, but if v_f is decreasing then it turns into X_{SS} at the nonsmooth fold NS2.

In the case $j < \mu$, the diagram changes substantially, which can be seen in Figure 4.7. The dual-point sliding solution X_{SS} is no more present. The dual-point rolling solution X_{SS} turns into X_{SR} at $v_{f,\mathrm{RR/SR}}$, but there is an unstable region of X_{SR} between $v_{f,\mathrm{SR/SS}}$ and $v_{f,\mathrm{RR/SR}}$, as well. The bifurcation structure is odd for the first sight, but it can be understood if some non-realisable stationary solutions are considered, too (see the dotted lines in Figure 4.7). In the case $v_f > v_{f,\mathrm{RR/SR}}$ (4.51), X_{RR} is in the *repelling sliding region*, thus, this would be considered as an *unstable* solution (see Figure 2.3). It can be checked that this solution would result in a *negative* normal force N^+, which is not allowed by the mechanical model. Still, if the bifurcation is completed with this unstable branch at $v_{f,\mathrm{RR/SR}}$, we get a degenerate version of the *nonsmooth transcritical bifurcation* (see [47]) and it is denoted by DNT1. At $v_{f,\mathrm{SR/SS}}$, a stable branch of stationary solution X_{SS} can be found in a similar form to that of (4.68), but it is non-realisable due to the negative normal force N^+. Mathematically, the point $v_{f,\mathrm{SR/RR}}$ is a degenerate version of the non-smooth fold bifurcation (denoted by DNF2).

The notations and properties of the bifurcations in Figures 4.5-4.7 are collected in Table 4.8. By visualising the bifurcation parameters in the plane of the parameters v_f and μ, we get the diagram in Figure 4.9. In this diagram, the bifurcations are denoted by thick lines, which divide the parameter plane into several regions. In each region, the number and type of the stationary solutions are denoted by the usual acronyms. The values $\mu = \mu_{\mathrm{fold}}$ and $\mu = j$ correspond to higher order bifurcations where the bifurcation lines are connected to each other. The arrows show the intersections of the three typical regions of μ, which correspond to Figures 4.5, 4.6 and 4.7, respectively.

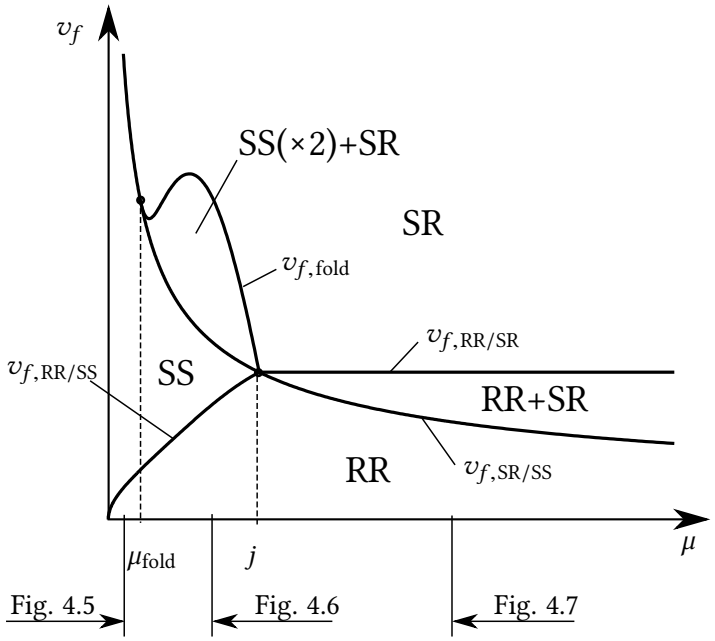

Figure 4.9: Bifurcations of the system plotted on the plane of the parameters v_f and μ.

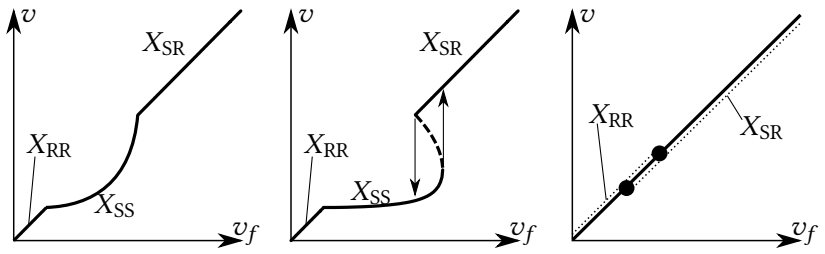

Figure 4.10: The characteristic curves of the ball corresponding to Figures 4.5, 4.6 and 4.7, respectively.

4.4.4 Limitations of the operation of the flowmeter

At a given construction of the flowmeter, the connection between the mass flow rate and the flow velocity v_f in the vessel can be provided by calibration. Thus, the quantity v_f can be considered as the input variable of the device and the output is the stationary velocity v of the ball, which can be measured from the outside of the vessel. Based on the bifurcation diagrams in Figures 4.5-4.7, the characteristic curves between the quantities v_f and v are sketched in Figure 4.10. In each case, limitations appear, which result problems in the practical usage of the flowmeter.

Problems of the case depicted in Figure 4.5 In the case $\mu < \mu_{\mathrm{fold}}$ (see the left panel of Figure 4.10), there is a single stable stationary solution all along the parameter range of v_f, which is favourable for the operation of the flowmeter. However, the

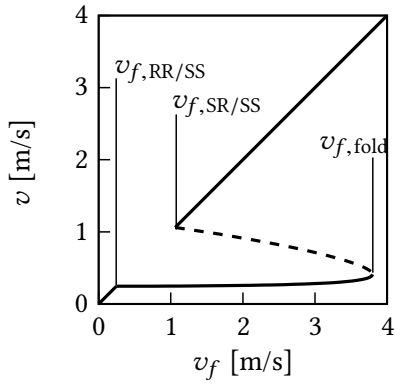

d	r	ρ_b	j
10 cm	1 cm	1.17 g/cm^3	0.4
g_0	ρ_f	ν_f	μ
9.81 m/s^2	1 g/cm^3	$1{\cdot}10^{-6}$ m^2/s	0.12

$v_{f,\mathrm{RR/SS}}$	$v_{f,\mathrm{SR/SS}}$	$v_{f,\mathrm{fold}}$
0.246 m/s	1.062 m/s	3.798 m/s

Figure 4.11: The data and the results of Example 5.2.

formula (4.74) shows that the value of μ_{fold} is in the range of 10^{-2} for physically relevant parameters. That is, the case $\mu < \mu_{\mathrm{fold}}$ cannot be ensured reliably in practice.

Problems of the case depicted in Figure 4.6 In the case $\mu_{\mathrm{fold}} < \mu < j$ (see the middle panel of Figure 4.10), the problem is caused by the hysteresis of the bifurcations NF2 and F. In the region of the hysteresis, it is impossible to use the flowmeter because there are two stable stationary solutions. Moreover, there is a substantial difference between v and v_f (see (4.70)), which reduces the sensitivity of the device also in the lower region of X_{SS}. The flowmeter can be used only for low flow velocities in the range of the dual-point rolling case X_{RR}, which is a substantial limitation of the device.

Problems of the case depicted in Figure 4.7 In the case $\mu > j$ (see the right panel of Figure 4.10), the stationary velocity of the ball equals to the velocity v_f of the fluid along the whole domain of v_f. However, the stationary solutions X_{RR} and X_{SR} overlap each other in a region (see the section between the two dots in Figure 4.10. Although the slipping-rolling solution X_{SR} is unstable in the overlapping region, the vanishing of the normal force N^+ leads to a problems in this region. Perturbation can make the ball to *separate* from the ground of the vessel, which leads to impacts, which are unfavourable for the operation of the flowmeter (see [7] for the detalis).

Example 4.4 (Numerical example)**.** The results are demonstrated on a physically realistic parameter set of the flowmeter. Suppose that the ball is made of polyamide and the fluid is water. The necessary data can be found in Figure 4.11. The *reduced* gravitational acceleration is calculated by $g = (\rho_b - \rho_f)/\rho_b \cdot g_0 = 1.35$ m/s^2, where g_0 is the gravitational acceleration, and ρ_b, ρ_f denote the densities of the ball and the fluid, respectively. The linear coefficient c of the drag force is approximated by Stokes' Law (see e.g. [59], p. 451) in the form

$$c = \frac{9\nu_f}{2r^2} \cdot \frac{\rho_f}{\rho_b} = 0.039 \cdot \mathrm{m/s}^2, \tag{4.75}$$

where v_f is the kinematic viscosity of the water. The critical friction coefficient becomes $\mu_{\text{fold}} = 0.03$, thus, the system corresponds to the case in the middle panel of Figure 4.10. The resulting velocities of the bifurcation points can be found in Figure 4.11. Note that the values of $v_{f,\text{RR/SS}}$ and $v_{f,\text{SR/SS}}$ do not depend on the model of the drag force.

4.5 New results

Thesis Statement 4. Consider the model of the rotating ball flowmeter containing a ball moving along the edge of a cylindrical vessel with vertical axis; the ball is driven by the swirling flow inside the device. The difference between the radii of the vessel and the ball is d, and the dimensionless mass moment of inertia is j. It is assumed that the flow velocity v_f around the vessel is constant, and its effect on the ball is modelled by a linear drag force. The resultant acceleration from gravitation and buoyancy effect is denoted by g. The contact between the ball and the vessel is modelled by Coulomb friction with a uniform coefficient μ for both the static and the dynamic cases.

i) The analysis of the resulting extended Filippov system shows that in the case $\mu < j$, the stationary state of dual-point rolling case exists if

$$v_f < \sqrt{\frac{gd}{\mu}} \cdot \sqrt{\frac{\mu^2(\mu+1)}{\mu^2(j+1)+j-\mu}}.$$

Otherwise, the ball starts slipping at both contact points. In case $\mu > j$, the stationary state of dual-point rolling case exists if

$$v_f < \sqrt{\frac{gd}{j}},$$

otherwise, the ball starts slipping at the contact point on the bottom of the vessel.

By calculating the equilibrium solutions of the slipping cases, as well, the bifurcation diagrams of the system can be created for the bifurcation parameter v_f.

ii) In the system, a fold bifurcation and a degenerate nonsmooth transcritical bifurcation occur, moreover, the variants of nonsmooth fold and persistence bifurcations occur related to the codimension-2 discontinuity manifolds.

The analyses of these bifurcations show significant limitations of the corresponding flowmeter device.

Related publications: [3], [6], [7].

Chapter 5

Nonsmooth contact model of railway wheelsets

5.1 Introduction

In Chapter 1, the kinematic oscillations of railway wheelsets were analysed, where we assumed pure rolling between the wheels and the rails. However, for large contact forces and for large velocities of the railway vehicle, the behaviour of the wheelset can be substantially different from pure rolling. In the literature, this effect is called *creep*.

The Creep effect of rolling elastic bodies was already described by Reynolds [60] in 1875. Large normal forces between the contacting bodies initiate the formation of a finite contact area around the theoretical contact point. Due to the local deformations, the surfaces are sticking in some regions of the contact area but they are slipping on each other in other regions. The resulting motion leads to a deviation from pure rolling, which is characterised by the *creep velocity*, or in other words, by the slipping velocity of the contact point. Several models can be found in the literature for describing the relation between the creep velocities and the tangential forces (also *creep forces*).

A linear creep model was introduced by Carter [17] for the analysis of the contact between the railway wheelsets and the rails. From that model, the critical velocity of a single wheelset can be determined where unstable oscillations of the wheelset appear (see e.g. [66, 53]). The coefficients of the linear model can be approximated from the contact theory of Hertz [30, 31]. For increasing creep velocities, the linear creep model overestimates the forces and the creep forces saturates for large creeps. This effect is described by nonlinear creep models introduced first by Vermeulen and Johnson [69, 38]. A detailed analysis of the sticking and slipping regions of the contact area was analysed by Kalker [40, 37, 41], who developed practical methods to determine the parameters of the creep models. The nonlinearity of the creep models can lead to complicated dynamics of the wheelset (see [44, 33]), and this effect can be combined with nonlinearity from flange contact, too (see [50, 74]). For a more detailed description of the different creep models and for further references, see [35, 14].

	Notation	Meaning
variables	y	lateral displacement of the wheelset
	ψ	yaw angle of the wheelset
	φ	rotation angle of the wheelset about its symmetry axis
	w	location of the wheelset along the track
	u_1^+, u_1^-	slipping velocities at the contact points in the direction of the track
	u_a	transversal slipping velocity at the contact points
	$\Psi = b\psi$	normalized yaw angle
model parameters	b	half-distance between contact points
	r	rolling radius of the wheelset
	v	speed of the wheelset along the track
	a_{01}, b_{10}	linear coefficients of the differential equation of kinematic oscillations
	μ	friction coefficient between the wheels and the rails
	F_{load}	vertical load of the wheelset from the vehicle (axle load)
	m	mass of the wheelset
	J_φ	mass moment of inertia of the wheelset with respect to its symmetry axis
	J_ψ	mass moment of inertia of the wheelset with respect to the axes normal to the symmetry axis
composed parameters	$C = \mu F_{\text{load}}/(2m)$	normalized magnitude of Coulomb friction force
	$\omega_L = \sqrt{-a_{01} \cdot b_{10}}$	angular frequency of small amplitude oscillations
	$\eta = \sqrt{-a_{01}/(b^2 \cdot b_{10})}$	dimensionless geometric factor
	$\alpha_y = \sqrt{k_y/m}$	natural angular frequency from the lateral stiffness
	$\alpha_\psi = \sqrt{k_\psi/J_\psi}$	natural angular frequency from the yaw stiffness
	$M_\psi = mb^2/J_\psi$	dimensionless parameter from J_ψ
	$M_\varphi = mr^2/J_\varphi$	dimensionless parameter from J_φ

Table 5.1: Important notations of Chapter 5. For further notations, see Tables 2.1 and 3.1.

The new idea presented in this chapter is approximating the nonlinear (saturated) creep force model with the Coulomb friction model. Then, instead of the nonlinear description of the creep forces, there is a nonsmooth contact force law including the pure rolling and pure slipping dynamics between the wheelset and the rails. The resulting mechanical system can be analysed by methods introduced in Chapter 3. Hence, we can obtain the conditions of transition between the dual-point rolling and slipping behaviour of the wheelset. Parts of these results has been published in the conference poster [10] of the candidate. In the conference paper [8], a similar problem was analysed with a ball rolling in a trough.

The structure of the chapter is the following: In Section 5.2, the mechanical model of the wheelset is presented by using the linearised kinematics from Chapter 1, but by considering slipping with the Coulomb friction law, too. In Section 5.3, the resulting discontinuous dynamical system is derived and it is analysed by the tools presented in Chapter 3. In Section 5.4, the conditions of slipping are derived in case of dual-point rolling, and hence, the maximum possible amplitude of the oscillations is determined without slipping. The new results are summarised in Section 5.5.

5.2 Mechanical model

In this section, the model of the railway wheelset is derived based on the kinematic model of Chapter 1, but by adding the possibility of slipping at the contact points, as well. The most important notations are summarized in Table 5.1.

5.2.1 Kinematics

In Chapter 1, the dynamics of the dual-point rolling of the wheelset was derived for generalised coordinates

$$q = [y, \psi, \varphi, w], \tag{5.1}$$

and we derived the set

$$\begin{aligned} \dot{y} &= a_{01}\psi + O^3(y,\psi), \\ \dot{\psi} &= b_{10}y + O^3(y,\psi), \\ \dot{\varphi} &= \frac{v}{r} + O^2(y,\psi), \\ \dot{w} &= v \end{aligned} \tag{5.2}$$

of first-order differential equations, which are purely determined by kinematics (see (1.23)-(1.27) and (1.28)). In this chapter, the analysis is restricted to the *linear* case of small amplitudes and thus, the higher order terms are neglected.

At the case when the wheelset starts slipping at one or both contact points, the

structure of the equations (5.2) can be preserved in the form

$$\begin{aligned} \dot{y} &= a_{01}\psi + \dot{y}_{\text{slip}}, \\ \dot{\psi} &= b_{10}y + \dot{\psi}_{\text{slip}}, \\ \dot{\varphi} &= \frac{v}{r} + \dot{\varphi}_{\text{slip}}, \\ \dot{w} &= v, \end{aligned} \tag{5.3}$$

where the terms $\dot{y}_{\text{slip}}, \dot{\psi}_{\text{slip}}$ and $\dot{\varphi}_{\text{slip}}$ denote the deviations of the time derivatives from the dual-point rolling case. These quantities are determined from the velocities of the contact points by using the formulation of Chapter 3.

The centre C of the wheelset and the contact point P^+ and P^- can be seen in Figures 1.2 and 5.2. By using (1.13) and (1.15), the location of the contact points becomes

$$\mathbf{r}^+ = \begin{bmatrix} V_r^+ - w \\ b + U_r^+ - y \\ -r + c_r(U_r^+) - z \end{bmatrix}, \qquad \mathbf{r}^- = \begin{bmatrix} V_r^- - w \\ -b - U_r^- - y \\ -r + c_r(U_r^-) - z \end{bmatrix}. \tag{5.4}$$

The unit normal vectors can be determined from the cross product of partial derivatives of (1.13), and we get

$$\mathbf{n}^+ = \begin{bmatrix} 0 \\ -c_r'(U_r^+) \\ 1 \end{bmatrix}, \qquad \mathbf{n}^- = \begin{bmatrix} 0 \\ c_r'(U_r^-) \\ 1 \end{bmatrix}. \tag{5.5}$$

For an accurate calculation, the expansion (1.53) should be substituted into (5.4) and (5.5), which leads to lengthy formulae. Instead, an *approximate* description is used in the subsequent calculations by considering

$$\mathbf{r}^+ \approx \begin{bmatrix} 0 \\ b \\ -r \end{bmatrix}, \qquad \mathbf{r}^- \approx \begin{bmatrix} 0 \\ -b \\ -r \end{bmatrix}, \tag{5.6}$$

and

$$\mathbf{n}^+ \approx \begin{bmatrix} 0 \\ 0 \\ 1 \end{bmatrix}, \qquad \mathbf{n}^- \approx \begin{bmatrix} 0 \\ 0 \\ 1 \end{bmatrix}. \tag{5.7}$$

These approximations contain not only the assumption linear (small-amplitude) oscillations but the assumption that the limit case $h \to 0$ of the conicity h of the wheels, as well. Note that this assumption is used for calculating only the slipping part of the kinematics and the Newton-Euler equations. However, in the kinematic equations (5.3), it is essential to assume a finite value of h when calculating the coefficients a_{01} and b_{10} of kinematic oscillations.

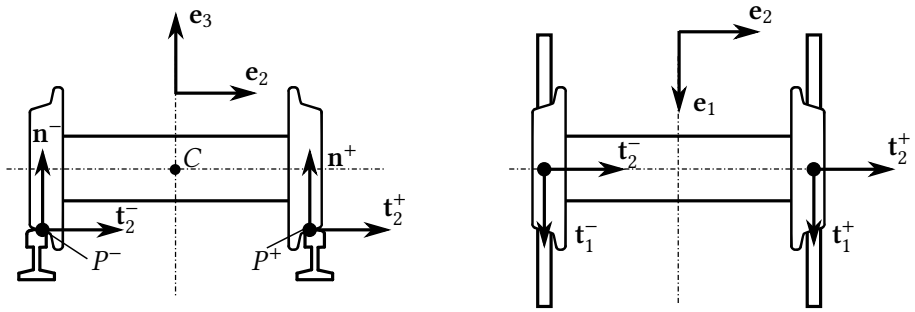

Figure 5.2: The local coordinate systems at the contact points.

From (5.6), we get

$$\mathbf{r}^+ - \mathbf{r}^- \approx \begin{bmatrix} 0 \\ 2b \\ 0 \end{bmatrix}, \qquad \mathbf{a} \approx \begin{bmatrix} 0 \\ 1 \\ 0 \end{bmatrix}, \tag{5.8}$$

and from the formulae (3.3)-(3.4), the tangential unit vectors at the contact points become

$$\mathbf{t}_1^+ \approx \begin{bmatrix} 1 \\ 0 \\ 0 \end{bmatrix}, \qquad \mathbf{t}_2^+ \approx \begin{bmatrix} 0 \\ 1 \\ 0 \end{bmatrix}, \tag{5.9}$$

$$\mathbf{t}_1^- \approx \begin{bmatrix} 1 \\ 0 \\ 0 \end{bmatrix}, \qquad \mathbf{t}_2^- \approx \begin{bmatrix} 0 \\ 1 \\ 0 \end{bmatrix} \tag{5.10}$$

(see Figure 5.2). The formula (3.9) gives $u_a = u_2^+ = u_2^-$, and the approximate velocities of the contact points given by (3.10) become

$$\mathbf{v}^+ \approx \begin{bmatrix} u_1^+ \\ u_a \\ 0 \end{bmatrix}, \qquad \mathbf{v}^- \approx \begin{bmatrix} u_1^- \\ u_a \\ 0 \end{bmatrix}. \tag{5.11}$$

Let

$$\mathbf{v}_{C,\text{slip}} \approx \begin{bmatrix} 0 \\ \dot{y}_{\text{slip}} \\ 0 \end{bmatrix}, \qquad \boldsymbol{\Omega}_{\text{slip}} \approx \begin{bmatrix} 0 \\ \dot{\varphi}_{\text{slip}} \\ \dot{\psi}_{\text{slip}} \end{bmatrix} \tag{5.12}$$

be the slipping part of the velocity $\mathbf{v}_C$ of the centre of gravity and the angular velocity $\boldsymbol{\Omega}$ of the body, respectively. These quantities measure the deviation from the dual-point rolling case, hence, the kinematic relations

$$\begin{aligned} \mathbf{v}^+ &= \mathbf{v}_C + \boldsymbol{\Omega} \times \mathbf{r}^+, \\ \mathbf{v}^- &= \mathbf{v}_C + \boldsymbol{\Omega} \times \mathbf{r}^- \end{aligned} \tag{5.13}$$

can be separated into

$$\begin{aligned} \mathbf{0} &= \left(\mathbf{v}_C - \mathbf{v}_{C,\text{slip}}\right) + \left(\boldsymbol{\Omega} - \boldsymbol{\Omega}_{\text{slip}}\right) \times \mathbf{r}^+, \\ \mathbf{0} &= \left(\mathbf{v}_C - \mathbf{v}_{C,\text{slip}}\right) + \left(\boldsymbol{\Omega} - \boldsymbol{\Omega}_{\text{slip}}\right) \times \mathbf{r}^-, \end{aligned} \tag{5.14}$$

and

$$\begin{aligned} \mathbf{v}^+ &= \mathbf{v}_{C,\text{slip}} + \boldsymbol{\Omega}_{\text{slip}} \times \mathbf{r}^+, \\ \mathbf{v}^- &= \mathbf{v}_{C,\text{slip}} + \boldsymbol{\Omega}_{\text{slip}} \times \mathbf{r}^-. \end{aligned} \tag{5.15}$$

By comparing (5.11) and (5.15), the slipping terms in (5.3) can be expressed by the slipping velocities u_1^+, u_1^- and u_a in the form

$$\dot{y}_{\text{slip}} \approx u_a, \qquad \dot{\psi}_{\text{slip}} \approx -\frac{u_1^+ - u_1^-}{2b}, \qquad \dot{\varphi}_{\text{slip}} \approx -\frac{u_1^+ + u_1^-}{2r}. \tag{5.16}$$

By substituting (5.16) into (5.3), we get the approximate linearised equations

$$\begin{aligned} \dot{y} &= a_{01}\psi + u_a, \\ \dot{\psi} &= b_{10}y - \frac{u_1^+ - u_1^-}{2b}, \\ \dot{\varphi} &= \frac{v}{r} - \frac{u_1^+ + u_1^-}{2r}, \\ \dot{w} &= v. \end{aligned} \tag{5.17}$$

In (5.17), the time derivatives of the generalised coordinates are expressed by the set

$$s = [u_1^+, u_1^-, u_a, \dot{w}] \tag{5.18}$$

of quasi-velocities. From (5.17), the second derivatives of the generalised coordinates become

$$\begin{aligned} \ddot{y} &= a_{01}b_{10}y - a_{01}\frac{u_1^+ - u_1^-}{2b} + \dot{u}_a, \\ \ddot{\psi} &= a_{01}b_{10}\psi + b_{10}u_a - \frac{\dot{u}_1^+ - \dot{u}_1^-}{2b}, \\ \ddot{\varphi} &= -\frac{\dot{u}_1^+ + \dot{u}_1^-}{2r}, \\ \ddot{w} &= 0. \end{aligned} \tag{5.19}$$

5.2.2 Dynamics

The dynamics of the wheelset is analysed by following the steps and notations of Section 3.3. From (3.18), the contact forces become

$$\mathbf{F}^+ \approx \begin{bmatrix} T_1^+ \\ T_2^+ \\ N^+ \end{bmatrix}, \qquad \mathbf{F}^- \approx \begin{bmatrix} T_1^- \\ T_2^- \\ N^- \end{bmatrix}. \tag{5.20}$$

It is assumed that the centre C of the wheelset is connected rigidly to the vehicle in the longitudinal direction $\mathbf{e}_1$, and the corresponding constraint force is denoted by F_{tract} (traction force). In the vertical direction, the axial load F_{load} is acting at C which contains the force from the weight of the vehicle and the weight of the wheelset. The force F_{load} is considered as a known parameter. The wheelset is connected to the vehicle with a resultant lateral stiffness k_y and a resultant yaw stiffness k_ψ. Therefore, the external loads acting on the wheelset become

$$\mathbf{F}_e = \begin{bmatrix} F_{\text{tract}} \\ -k_y y \\ -F_{\text{load}} \end{bmatrix}, \qquad \mathbf{M}_e = \begin{bmatrix} 0 \\ 0 \\ -k_\psi \psi \end{bmatrix}. \tag{5.21}$$

The Newton-Euler equations from (3.19) lead to the algebraic equations

$$\begin{aligned} T_1^+ + T_1^- + F_{\text{tract}} &= 0, \\ N_1^+ + N_1^- - F_{\text{load}} &= 0, \\ b(N^+ - N^-) &= 0, \end{aligned} \tag{5.22}$$

and the equations of motion

$$\begin{aligned} m\ddot{y} + k_y y - (T_2^+ + T_2^-) &= 0, \\ J_\psi \ddot{\psi} + k_\psi \psi + b(T_1^+ - T_1^-) &= 0, \\ J_\varphi \ddot{\varphi} - r(T_1^+ + T_1^-) &= 0. \end{aligned} \tag{5.23}$$

From (5.22), the normal forces become $N^+ = N^- = F_{\text{load}}/2$.

In the literature, the velocity components of the contact points are called creep velocities and the tangential forces are calculated in the form

$$\begin{aligned} T_1^+ &= T_{\text{long}}(u_1^+, u_a), & T_2^+ &= T_{\text{trans}}(u_1^+, u_a), \\ T_1^- &= T_{\text{long}}(u_1^-, u_a), & T_2^- &= T_{\text{trans}}(u_1^-, u_a), \end{aligned} \tag{5.24}$$

where T_{long} and T_{trans} are the characteristic curves of the longitudinal and transversal *creep forces*, respectively. Due to the large normal forces between the wheelset and the rails, the deformation of the surfaces is significant, and *contact areas* are formed around the theoretical contact points.

A typical creep force curve can be seen in Figure 5.3 (denoted by dashed line). For small values of creep velocity, the creep force is nearly proportional to the creep velocity. In this range, the wheelset is slipping in some regions of the contact area and it is sticking in other regions. For larger creep velocities, the curve saturates and the force tends to the value of the Coulomb friction force when the whole contact area starts slipping.

The usual creep model for the linear region was introduced by Carter [17] in the form

$$T_{\text{long}}(u_1^+, u_a) = -\kappa_{\text{long}} \cdot \frac{u_1^+}{v}, \qquad T_{\text{trans}}(u_1^+, u_a) = -\kappa_{\text{trans}} \cdot \frac{u_a}{v}. \tag{5.25}$$

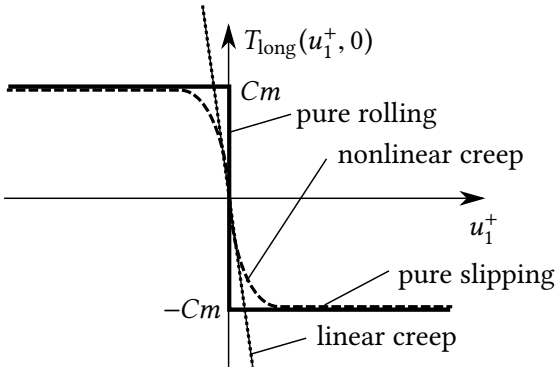

Figure 5.3: The comparison of creep models and the Coulomb model. The nonlinear creep model is denoted by dashed line. For small creep, the curve can be approximated by a linear creep model (denoted by a dotted line). The Coulomb model is an appropriate approximation for large creep in the sense (5.28).

where v is the velocity of the wheelset along the track and κ_{long} and κ_{trans} are the linear creep coefficients (see the dotted line in Figure 5.3). The values of these coefficients are usually determined by the theory of Kalker [40, 41].

The nonlinear region of the creep force curve was described by Johnson and Vermeulen [69, 38] where the saturation is described by a piecewise polynomial model. The modifications of this model are used nowadays in simulations of the wheel-rail contact forces (see [35]). The saturation effect can be described by a single formula, as well, e.g. by the following curve:

$$\begin{aligned} T_{\text{long}}(u_1^+, u_a) &= -Cm\frac{u_1^+}{\sqrt{(u_1^+)^2 + u_a^2}} \tanh\left(\frac{\kappa_{\text{long}}}{Cmv}\sqrt{(u_1^+)^2 + u_a^2}\right), \\ T_{\text{trans}}(u_1^+, u_a) &= -Cm\frac{u_a}{\sqrt{(u_1^+)^2 + u_a^2}} \tanh\left(\frac{\kappa_{\text{trans}}}{Cmv}\sqrt{(u_1^+)^2 + u_a^2}\right), \end{aligned} \tag{5.26}$$

where $C := \mu F_{\text{load}}/(2m)$ is the normalized magnitude of the Coulomb friction force.

If the magnitude of the creep velocity is small in the sense

$$\sqrt{(u_1^+)^2 + u_a^2} \ll \min\left(\frac{\kappa_{\text{long}}}{Cmv}, \frac{\kappa_{\text{trans}}}{Cmv}\right) \tag{5.27}$$

then the model (5.26) tends to the linear creep model (5.25). In the other limit case when the creep velocity is large in the sense

$$\sqrt{(u_1^+)^2 + u_a^2} \gg \max\left(\frac{\kappa_{\text{long}}}{Cmv}, \frac{\kappa_{\text{trans}}}{Cmv}\right) \tag{5.28}$$

then (5.26) tends to the simple Coulomb model

$$\begin{aligned} T_{\text{long}}(u_1^+, u_a) &= -Cm\frac{u_1^+}{\sqrt{(u_1^+)^2 + u_a^2}}, \\ T_{\text{trans}}(u_1^+, u_a) &= -Cm\frac{u_a}{\sqrt{(u_1^+)^2 + u_a^2}}. \end{aligned} \tag{5.29}$$

That is, Coulomb friction model is an appropriate model for wheel-rail contact in the case (5.28), which is satisfied at large creep velocities, large values of the linear coefficients κ_{long} and κ_{trans} or low velocities v of the vehicle (see the thick solid line in Figure 5.3).

In the literature, it is a common implicit assumption that the creep of the wheelset is always symmetric. Then, $u_1^+ \equiv -u_1^-$, and (5.24) leads to $T_1^+ = -T_1^-$ and $T_2^+ = T_2^-$. Hence, the third equation of (5.23) becomes $\ddot{\varphi} \equiv 0$, and the other two equations become a set of two second-order differential equations in the form

$$\begin{aligned} m\ddot{y} + k_y y - 2T_{\text{trans}}(u_1^+, u_a) &= 0, \\ J_\psi \ddot{\psi} + k_\psi \psi + 2bT_{\text{long}}(u_1^+, u_a) &= 0, \end{aligned} \tag{5.30}$$

where the creep velocities from (5.17) are given by $u_a = \dot{y} - a_{01}\psi$ and $u_1^+ = -(\dot{\psi} + b_{10}y)$ (see [66, 53]). In the subsequent calculations, *non-symmetric* slipping of the wheelset is considered, too, where $u_1^+ \neq u_1^-$. That is, the case when the $\dot{\varphi}_{\text{slip}} \neq 0$ is considered, as well (see (5.16)).

5.3 Nonsmooth dynamics

5.3.1 Differential equations for the different cases

From the four generalised coordinates (5.1), the cyclic coordinates φ and w can be separated (see (1.24)) because they do not affect the dynamics of the other variables. To get a simpler form of the equations, let us introduce the normalised yaw angle $\Psi := b\psi$, which has a dimension of length. From the four quasi-velocities (5.18), the velocity v is omitted because it is prescribed as a parameter. Finally, we have the minimal set

$$x = [y, \Psi, u_1^+, u_1^-, u_a] \tag{5.31}$$

of state variables containing variables y and Ψ of the kinematics oscillation and the three slipping velocities u_1^+, u_1^- and u_a.

Let us introduce the linear angular frequency $\omega_L = \sqrt{-a_{01}b_{10}}$ of the kinematic oscillations (see (1.31)) and the geometric factor $\eta := \sqrt{-a_{01}/(b_{10}b^2)}$. By using these notations, the first two equations from (5.17) become

$$\begin{aligned} \dot{y} &= \omega_L \eta \Psi + u_a, \\ \dot{\Psi} &= -\frac{\omega_L}{\eta} y - \frac{u_1^+ - u_1^-}{2}. \end{aligned} \tag{5.32}$$

From (5.23), the derivatives of the slipping velocities can be expressed. By substi-

tuting the accelerations (5.19) into (5.23), we get

$$\begin{aligned} m\left(-\omega_L^2 y - \omega_L \eta \frac{u_1^+ - u_1^-}{2} + \dot{u}_a\right) + k_y y - (T_2^+ + T_2^1) &= 0, \\ \frac{J_\psi}{b^2}\left(-\omega_L^2 \Psi + \frac{\omega_L}{\eta} u_a - \frac{\dot{u}_1^+ - \dot{u}_1^-}{2}\right) + \frac{k_\psi}{b^2}\Psi + (T_1^+ - T_1^-) &= 0, \\ \frac{J_\varphi}{r^2} \cdot \frac{\dot{u}_1^+ + \dot{u}_1^-}{2} - (T_1^+ + T_1^-) &= 0. \end{aligned} \tag{5.33}$$

Let us introduce the following parameters. Let $\alpha_y := \sqrt{k_y/m}$ denote the natural angular frequency of free oscillation of the wheelset in the lateral direction (consider (5.23) without the contact forces). Similarly, let $\alpha_\psi := \sqrt{k_\psi/J_\psi}$ denote the natural angular frequency for the yaw rotation. The dimensionless parameters $M_\psi := mb^2/J_\psi$ and $M_\varphi := mr^2/J_\varphi$ are related to the mass moments of inertia of the wheelset. With these notations, (5.33) can be written in the form

$$\begin{aligned} \dot{u}_a &= -(\alpha_y^2 - \omega_L^2) y - \omega_L \eta \cdot \frac{u_1^+ - u_1^-}{2} + \frac{T_2^+ + T_2^-}{m}, \\ \dot{u}_1^+ &= (\alpha_\psi^2 - \omega_L^2)\Psi - \frac{\omega_L}{\eta} u_a + (M_\varphi + M_\psi) \cdot \frac{T_1^+}{m} + (M_\varphi - M_\psi) \cdot \frac{T_1^-}{m}, \\ \dot{u}_1^- &= -(\alpha_\psi^2 - \omega_L^2)\Psi + \frac{\omega_L}{\eta} u_a + (M_\varphi - M_\psi) \cdot \frac{T_1^+}{m} + (M_\varphi + M_\psi) \cdot \frac{T_1^-}{m}. \end{aligned} \tag{5.34}$$

The time derivatives (5.32) and (5.34) provide the differential equations for the four kinematic cases (see Table 3.5). In the subsequent calculations, the methods and notations from Chapter 3 are used.

Case SS In the case when the wheelset is slipping at both contact points, (5.24) and (5.29) lead to

$$T_1^+ = -Cm \frac{u_1^+}{\sqrt{(u_1^+)^2 + u_a^2}}, \qquad T_2^+ = -Cm \frac{u_a}{\sqrt{(u_1^+)^2 + u_a^2}}, \tag{5.35}$$

$$T_1^- = -Cm \frac{u_1^-}{\sqrt{(u_1^-)^2 + u_a^2}}, \qquad T_2^- = -Cm \frac{u_a}{\sqrt{(u_1^-)^2 + u_a^2}} \tag{5.36}$$

(see also (3.27)-(3.28). Hence, from the equations (5.32) and (5.34), we get the vector field

$$F_{\mathrm{SS}} = \begin{bmatrix} \omega_L \eta \cdot \Psi + u_a \\ -\frac{\omega_L}{\eta} \cdot y - \frac{u_1^+ - u_1^-}{2} \\ (\alpha_\psi^2 - \omega_L^2)\Psi - \frac{\omega_L}{\eta} u_a - (M_\varphi + M_\psi) \cdot \frac{C u_1^+}{\sqrt{(u_1^+)^2 + u_a^2}} - (M_\varphi - M_\psi) \cdot \frac{C u_1^-}{\sqrt{(u_1^-)^2 + u_a^2}} \\ -(\alpha_\psi^2 - \omega_L^2)\Psi + \frac{\omega_L}{\eta} u_a - (M_\varphi - M_\psi) \cdot \frac{C u_1^+}{\sqrt{(u_1^+)^2 + u_a^2}} - (M_\varphi + M_\psi) \cdot \frac{C u_1^-}{\sqrt{(u_1^-)^2 + u_a^2}} \\ -(\alpha_y^2 - \omega_L^2) y - \omega_L \eta \cdot \frac{u_1^+ - u_1^-}{2} - \frac{C u_a}{\sqrt{(u_1^+)^2 + u_a^2}} - \frac{C u_a}{\sqrt{(u_1^-)^2 + u_a^2}} \end{bmatrix}. \tag{5.37}$$

This vector field is an extended Filippov system, it is discontinuous in the codimension-2 discontinuity sets Σ_{SR} defined by $u_1^- = u_a = 0$ and Σ_{RS} defined by $u_1^+ = u_a = 0$.

Case SR If the wheelset is rolling at P^- but it is slipping at P^+ then the constraint $u_1^- = u_a = 0$ is satisfied. Then, (5.36) is not valid and (5.35) becomes

$$T_1^+ = -Cm \operatorname{sgn} u_1^+, \qquad T_2^+ = 0. \tag{5.38}$$

Then, from (5.32) and (5.34), we get the vector field

$$F_{\mathrm{SR}} = \begin{bmatrix} \omega_L \eta \cdot \Psi \\ -\frac{\omega_L}{\eta} \cdot y - \frac{u_1^+}{2} \\ \frac{2M_\psi}{M_\varphi + M_\psi} \cdot (\alpha_\psi^2 - \omega_L^2)\Psi - C \cdot \frac{4M_\psi M_\varphi}{M_\psi + M_\varphi} \cdot \operatorname{sgn} u_1^+ \\ 0 \\ 0 \end{bmatrix}. \tag{5.39}$$

This vector field is a Filippov system in Σ_{SR} and the discontinuity set is Σ_{RR} defined by $u_1^+ = 0$.

Case RS Due to the symmetry of the wheelset and the rails, we get similar results for Case RS to those of Case SR. In the rolling-slipping case, the rolling constraint $u_1^+ = u_a$ is satisfied, and the Coulomb friction (5.36) leads to

$$T_1^- = -Cm \operatorname{sgn} u_1^-, \qquad T_2^- = 0. \tag{5.40}$$

Then, we get the vector field

$$F_{\mathrm{RS}} = \begin{bmatrix} \omega_L \eta \cdot \Psi \\ -\frac{\omega_L}{\eta} \cdot y + \frac{u_1^-}{2} \\ 0 \\ -\frac{2M_\psi}{M_\varphi + M_\psi} \cdot (\alpha_\psi^2 - \omega_L^2)\Psi - C \cdot \frac{4M_\psi M_\varphi}{M_\psi + M_\varphi} \cdot \operatorname{sgn} u_1^+ \\ 0 \end{bmatrix}, \tag{5.41}$$

which is a Filippov system in Σ_{RS} with the discontinuity set Σ_{RR} at $u_1^- = 0$.

Case RR If the wheelset is rolling at both contact points then the kinematic constraints $u_1^+ = u_1^- = u_a = 0$ are satisfied. Then, from (5.32)-(5.34), we obtain the smooth vector field

$$F_{\mathrm{RR}} = \begin{bmatrix} \omega_L \eta \cdot \Psi \\ -\frac{\omega_L}{\eta} \cdot y \\ 0 \\ 0 \\ 0 \end{bmatrix}. \tag{5.42}$$

This is the dynamics of the kinematic oscillations described also by (1.28) and (5.2).

5.3.2 Compatibility of the dynamics of the different cases

In this subsection, the compatibility of the vector fields $F_{\mathrm{SS}}, F_{\mathrm{SR}}, F_{\mathrm{RS}}$ and F_{RR} is checked according to Definition 3.2.

Case SR as the sliding dynamics of Case SS The set Σ_{SR} is a codimension-2 discontinuity set of the vector field F_{SS}. According to (3.33), the set $n^-(\phi^-)$ of unit vectors is given by

$$e_1^- = \begin{bmatrix} 0 \\ 0 \\ 0 \\ 1 \\ 0 \end{bmatrix}, \qquad e_a = \begin{bmatrix} 0 \\ 0 \\ 0 \\ 0 \\ 1 \end{bmatrix}, \qquad n^-(\phi^-) = \begin{bmatrix} 0 \\ 0 \\ 0 \\ \cos\phi^- \\ \sin\phi^- \end{bmatrix}. \tag{5.43}$$

Then, the limit (3.34) leads to

$$F_{\mathrm{SS}}^{*-}(x_0)(\phi^-) = \begin{bmatrix} \omega_L \eta \cdot \Psi \\ -\frac{\omega_L}{\eta} \cdot y - \frac{u_1^+}{2} \\ (\alpha_\psi^2 - \omega_L^2)\Psi - (M_\varphi + M_\psi) \cdot C \operatorname{sgn} u_1^+ - (M_\varphi - M_\psi) \cdot C \cos\phi^- \\ -(\alpha_\psi^2 - \omega_L^2)\Psi - (M_\varphi - M_\psi) \cdot C \operatorname{sgn} u_1^+ - (M_\varphi + M_\psi) \cdot C \cos\phi^- \\ -(\alpha_y^2 - \omega_L^2)y - \omega_L \eta \cdot \frac{u_1^+}{2} - C \sin\phi^- \end{bmatrix}. \tag{5.44}$$

This limit vector field can be written into the form (2.28) by taking

$$\overline{F} = \begin{bmatrix} \omega_L \eta \cdot \Psi \\ -\frac{\omega_L}{\eta} \cdot y - \frac{u_1^+}{2} \\ (\alpha_\psi^2 - \omega_L^2)\Psi - (M_\varphi + M_\psi) \cdot C \operatorname{sgn} u_1^+ \\ -(\alpha_\psi^2 - \omega_L^2)\Psi - (M_\varphi - M_\psi) \cdot C \operatorname{sgn} u_1^+ \\ -(\alpha_y^2 - \omega_L^2)y - \omega_L \eta \cdot \frac{u_1^+}{2} \end{bmatrix}, \tag{5.45}$$

$$F_A = \begin{bmatrix} 0 \\ 0 \\ -C(M_\varphi - M_\psi) \\ -C(M_\varphi + M_\psi) \\ 0 \end{bmatrix}, \qquad F_B = \begin{bmatrix} 0 \\ 0 \\ 0 \\ 0 \\ -C \end{bmatrix}. \tag{5.46}$$

Then, there is an unique sliding dynamics guranteed by Theorem 2.17 and the coefficients of (2.32) become

$$a = \frac{-(\alpha_\psi^2 - \omega_L^2)\Psi - (M_\varphi - M_\psi) \cdot C \operatorname{sgn} u_1^+}{C(M_\varphi + M_\psi)}, \qquad b = \frac{-(\alpha_y^2 - \omega_L^2)y - \omega_L \eta \cdot \frac{u_1^+}{2}}{C}. \tag{5.47}$$

From (2.32), the sliding dynamics on Σ_{SR} can be computed. The resulting vector field coincides with F_{SR}. That is, the vector fields F_{SS} and F_{SR} are compatible in the sense of Definition 3.2.

Case RS as the sliding dynamics of Case SS Due to the symmetry of the system, the compatibility for the Case RS can be proven very similarly to the previous case. The set of the unit vectors corresponding to Σ_{RS} are given by

$$e_1^+ = \begin{bmatrix} 0 \\ 0 \\ 1 \\ 0 \\ 0 \end{bmatrix}, \qquad e_a = \begin{bmatrix} 0 \\ 0 \\ 0 \\ 0 \\ 1 \end{bmatrix}, \qquad n^+(\phi^+) = \begin{bmatrix} 0 \\ 0 \\ \cos\phi^+ \\ 0 \\ \sin\phi^+ \end{bmatrix}, \tag{5.48}$$

and the limit vector field from (3.36) leads to

$$F_{SS}^{*+}(x_0)(\phi^+) = \begin{bmatrix} \omega_L \eta \cdot \Psi \\ -\frac{\omega_L}{\eta} \cdot y + \frac{u_1^-}{2} \\ (\alpha_\psi^2 - \omega_L^2)\Psi - (M_\varphi + M_\psi) \cdot C \cos\phi^+ - (M_\varphi - M_\psi) \cdot C \operatorname{sgn} u_1^- \\ -(\alpha_\psi^2 - \omega_L^2)\Psi - (M_\varphi - M_\psi) \cdot C \cos\phi^+ - (M_\varphi + M_\psi) \cdot C \operatorname{sgn} u_1^- \\ -(\alpha_y^2 - \omega_L^2)y + \omega_L \eta \cdot \frac{u_1^-}{2} - C \sin\phi^+ \end{bmatrix}. \tag{5.49}$$

The following steps are similar to those of Case SR, and we get that the sliding dynamics generated by F_{SS} in Σ_{RS} equals to the vector field F_{RS}.

Case RR as the sliding dynamics of Cases SR and RS Conditions (c)-(d) of Definition 3.2 can be proven. By taking simply $\dot{u}_1^- = \dot{u}_a = 0$ and then $u_1^+ = u_a = 0$, the vector field F_{SR} tends to the rolling dynamics F_{RR}. This is satisfied similarly for F_{RS}.

That is, the vector fields F_{SS}, F_{SR}, F_{RS} and F_{RR} are compatible according to Definition 3.2, and thus, Proposition 3.3 can be applied to determine the conditions of slipping of the dual-point rolling case.

5.4 Analysis of the slipping of the wheelset

5.4.1 Conditions of slipping

Assume that the wheelset is in the state of dual-point-rolling, which corresponds to a point x_0 in the set Σ_{RR} with

$$x_0 = [y, \Psi, 0, 0, 0]. \tag{5.50}$$

In case of dual-point rolling, the contact forces are undetermined (see Table 3.5). That is, the condition of slipping of the wheelset cannot be determined directly from (3.22). Instead, Proposition 3.3 is used to determine whether there is slipping in any state x_0.

Transition to Case SR Let us evaluate F_{SR} at $x = x_0$ to check the condition (b) of Proposition 3.3. Then, we get

$$F_{\mathrm{SR}}(x_0) = \begin{bmatrix} \omega_L \eta \cdot \Psi \\ -\frac{\omega_L}{\eta} \cdot y \\ \frac{2M_\psi}{M_\varphi + M_\psi} \cdot (\alpha_\psi^2 - \omega_L^2)\Psi - C \cdot \frac{4M_\psi M_\varphi}{M_\psi + M_\varphi} \cdot \operatorname{sgn} u_1^+ \\ 0 \\ 0 \end{bmatrix}. \tag{5.51}$$

From this expression, it can be shown by direct calculation that according to Definition 2.2, the point x_0 lays in the attracting sliding region of Σ_{RR} if

$$|\Psi| < \Psi_{\mathrm{sli}} := \frac{2CM_\psi}{\left|\alpha_\psi^2 - \omega_L^2\right|}. \tag{5.52}$$

The α-trajectory of x_0 with respect to F_{SR} appears in the boundary case $\Psi = \pm\Psi_{\mathrm{sli}}$ corresponding to two parallel lines in the plane $y - \Psi$ of the phase space of dual-point rolling (see the dashed lines in Figure 5.4).

In the case $\alpha_\psi > \omega_L$ and $\Psi = +\Psi_{\mathrm{sli}}$, the α-trajectory of x_0 corresponds to $u_1^+ > 0$ (see (5.51)). By substituting these values, the limit vector field (5.44) becomes

$$F_{\mathrm{SS}}^{*-}(y, \Psi_{\mathrm{sli}}, 0, 0, 0)(\phi^-) = \begin{bmatrix} \omega_L \eta \cdot 2CM_\psi / (\alpha_\psi^2 - \omega_L^2) \\ -\frac{\omega_L}{\eta} \cdot y \\ -(M_\varphi - M_\psi) \cdot C \cdot (\cos\phi^- + 1) \\ -(M_\varphi + M_\psi) \cdot C \cdot (\cos\phi^- + 1) \\ -(\alpha_y^2 - \omega_L^2) y - C \sin\phi^- \end{bmatrix}. \tag{5.53}$$

The condition of the neutral limit trajectory is $\left\langle e_1^+, F_{\mathrm{SS}}^{*-} \right\rangle = \left\langle e_a, F_{\mathrm{SS}}^{*-} \right\rangle = 0$, which leads to

$$y = 0, \qquad \phi^- = \pi. \tag{5.54}$$

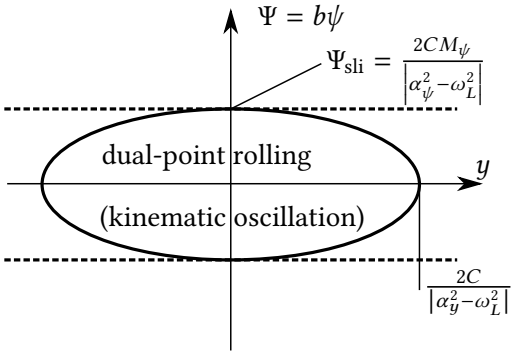

Figure 5.4: The condition of slipping of the wheelset during dual-point rolling motion. The dashed lines denote the condition of slipping at *one* of the contact points (transition to Cases SR or RS), and the ellipse denotes the condition of slipping at *both* contact points (transition to Case SS). As the latter condition is stricter, there is no possibility for slipping at only one of the contact points but slipping occurs at both contact points simultaneously.

It can be checked numerically that for both $y < 0$ and $y > 0$, the point x_0 is in the crossing region of Σ_{SR} with respect to F_{SS}. The same result can be proven for $\alpha_\psi < \omega_L$ and for $\Psi = -\Psi_{\text{sli}}$. Hence, conditions of case (b) of Proposition 3.3 is not satisfied, that is, *there is no possibility for transition of the dynamics from Case RR to Case SR.*

Transition to Case RS Due to the symmetries of the system, there is no fundamental difference between the two contact points. Thus, by carrying out the same calculation as for Case SR, we get that *there is no possibility for transition of the dynamics from Case RR to Case RS.*

Transition to Case SS For case (d) of Proposition 3.3, let us calculate the limit vector field of F_{SS} at the double discontinuity Σ_{RR} (see (3.42)),

$$\hat{F}^*_{\text{SS}}(x_0)(\phi^+, \phi^-) = \begin{bmatrix} \omega_L \eta \cdot \Psi \\ -\frac{\omega_L}{\eta} \cdot y \\ (\alpha_\psi^2 - \omega_L^2)\Psi - (M_\varphi + M_\psi)C\cos\phi^+ - (M_\varphi - M_\psi)C\cos\phi^- \\ -(\alpha_\psi^2 - \omega_L^2)\Psi - (M_\varphi - M_\psi)C\cos\phi^+ - (M_\varphi + M_\psi)C\cos\phi^- \\ -(\alpha_y^2 - \omega_L^2)y - C\sin\phi^+ - C\sin\phi^- \end{bmatrix}. \quad (5.55)$$

The conditions of the neutral limit direction are

$$\begin{aligned} \left\langle e_1^+, \hat{F}^*_{\text{SS}}(x_0)(\phi^+, \phi^-) \right\rangle &= 0, \\ \left\langle e_1^-, \hat{F}^*_{\text{SS}}(x_0)(\phi^+, \phi^-) \right\rangle &= 0, \\ \left\langle e_a, \hat{F}^*_{\text{SS}}(x_0)(\phi^+, \phi^-) \right\rangle &= 0, \end{aligned} \quad (5.56)$$

from which we obtain

$$\phi^+ = \arctan\left(-(\alpha_y^2 - \omega_L^2)y, (\alpha_\psi^2 - \omega_L^2)\Psi/M_\psi\right), \qquad \phi^- = \pi - \phi^+, \tag{5.57}$$

and

$$(\alpha_y^2 - \omega_L^2)^2 y^2 + \frac{(\alpha_\psi^2 - \omega_L^2)^2}{M_\psi^2}\Psi^2 = 4C^2. \tag{5.58}$$

The equation (5.58) determines an ellipse in the $y - \Psi$ plane of Σ_{RR} (see Figure 5.4). In the special case $y = 0$, (5.58) is equivalent to $\Psi = \pm\Psi_{\mathrm{sli}}$, therefore, the lines determined by (5.52) touch the ellipse in the phase plane.

It can be checked numerically that inside the ellipse determined by (5.58), there is no α-trajectory, that is, there is no transition from Case RR to Case SS. Outside the ellipse, there is an α-trajectory, that is, the dynamics switches to Case SS. The results are summarized in the following proposition:

Proposition 5.1. *Consider the wheelset from the initial state $x_0 = [y, \Psi, 0, 0, 0]$ corresponding to the dual-point rolling case. If*

$$(\alpha_y^2 - \omega_L^2)^2 y^2 + \frac{(\alpha_\psi^2 - \omega_L^2)^2}{M_\psi^2}\Psi^2 < 4C^2 \tag{5.59}$$

then the dynamics of the wheelset is described by (5.42)*, and the wheelset is rolling at both contact points, otherwise, the dynamics is described by* (5.37)*, and the wheelset is slipping at both contact points.*

Let us solve the equations (3.39) in the case $\phi^- = \pi - \phi^+$, which corresponds to the boundary case when the α-trajectory appears. For the direction of the limit trajectory, we get

$$\hat{n}(\phi^+, -\phi^+) = \frac{1}{\sqrt{2\cos^2\phi^+ + \sin^2\phi}} \cdot \begin{bmatrix} 0 \\ 0 \\ \cos\phi^+ \\ -\cos\phi^+ \\ \sin\phi^+ \end{bmatrix}. \tag{5.60}$$

This vector lays in the hyperplane $u_1^- = -u_1^+$, which is related to the assumption of the symmetric slip in (5.30). That is, that assumption is valid in the sense that the wheelset *starts* slipping at both contact points with $u_1^- = -u_1^+$. Then, the symmetry in the variables in F_{SS} keeps this assumption valid and the wheelset remains in the state of symmetric slipping. However, if the perturbations of the system create a state of slipping with $u_1^- \neq -u_1^+$, the usage of separate variables for u_1^+ and u_1^- is still necessary.

5.4.2 Velocity dependence of the critical amplitudes

In the previous subsection, we obtained a local condition of the transition from dual-point rolling to dual-point slipping. Let us now consider the condition from the viewpoint of amplitude of kinematic oscillations.

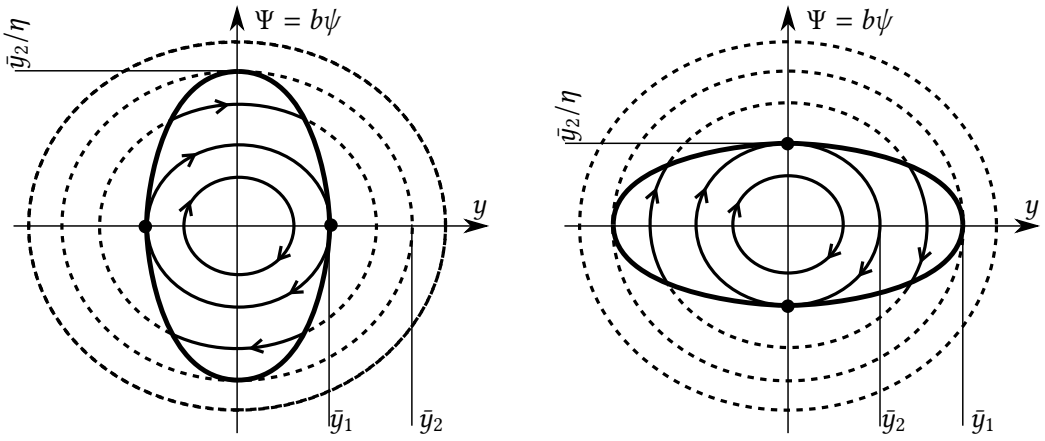

Figure 5.5: The condition of slipping in the phase plane of the kinematic oscillations. Left panel: $\bar{y}_1 < \bar{y}_2$. Right panel: $\bar{y}_1 > \bar{y}_2$. The thick ellipse denotes the condition (5.58) of slipping. Inside the ellipse, the elliptical trajectories of the kinematic oscillations are valid (continuous lines). If a trajectory crosses the boundary ellipse, the wheelset starts slipping at both contact points, and the dynamics leaves the 2D phase plane of the figure. That is, the trajectories denoted by dashed lines are not realizable.

By integrating the vector field (5.42), trajectories of the dual-point rolling case can be written into the form

$$y^2 + \eta^2 \Psi^2 = \bar{y}^2, \tag{5.61}$$

where $\bar{y}$ is the amplitude of the oscillations expressed by the lateral displacement (see also (1.6)). These trajectories are ellipses in the plane $y - \Psi$ of Σ_{RR}. By considering the intersection between these ellipses and the ellipse (5.58), two different typical situations occur depending on the eccentricity of the ellipses.

In the case

$$\eta M_\psi > \left| \frac{\alpha_\psi^2 - \omega_L^2}{\alpha_y^2 - \omega_L^2} \right|, \tag{5.62}$$

the trajectories (5.61) are inside the ellipse (5.58) for $\bar{y} < \bar{y}_1$ (see the left panel of Figure 5.5), where

$$\bar{y}_1 := \frac{2C}{\left| \alpha_y^2 - \omega_L^2 \right|}. \tag{5.63}$$

At the critical amplitude $\bar{y} = \bar{y}_1$, the trajectory touches the ellipse (5.58) of the boundary of the slipping (see the black dots in the figure). Trajectories with larger amplitudes intersect the boundary ellipse transversally, and then, the trajectory leaves Σ_{RR} to the five-dimensional phase space and the wheelset starts slipping.

In the case

$$\eta M_\psi > \left| \frac{\alpha_\psi^2 - \omega_L^2}{\alpha_y^2 - \omega_L^2} \right|, \tag{5.64}$$

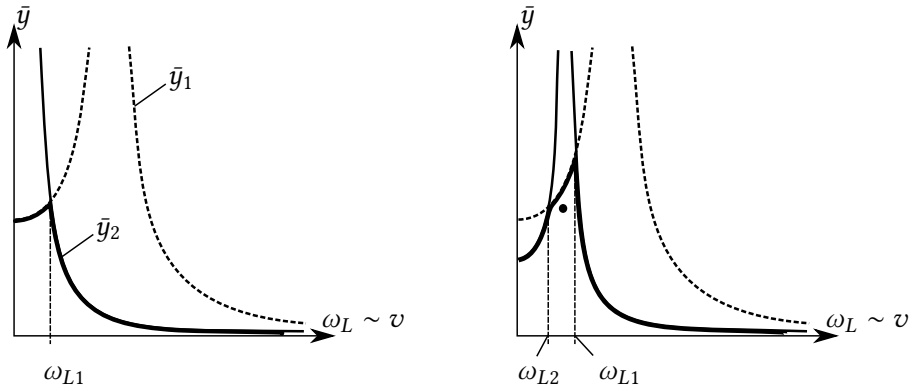

Figure 5.6: The velocity dependence of the maximum amplitudes of oscillation without slipping. Left panel: the case when the value ω_{L2} does not extis. Right panel: the case when both ω_{L1} and ω_{L2} exist. The dashed line in the graphs corresponds to condition (5.63), and the solid line corresponds to condition (5.65). The minimum of these curves are denoted by thick solid line, which is the actual maximal amplitude of the kinematic oscillations.

the trajectories are inside the ellipse (5.58) for $\bar{y} < \bar{y}_2$ (see the right panel of Figure 5.5), where

$$\bar{y}_2 := \frac{2CM_\psi\eta}{\left|\alpha_\psi^2 - \omega_L^2\right|}. \tag{5.65}$$

The trajectory with an amplitude $\bar{y} = \bar{y}_2$ touches the ellipse of the condition of slipping.

Hence, the maximum amplitude of kinematic oscillations without slipping is determined by $\min(\bar{y}_1, \bar{y}_2)$. These quantities are depicted in Figure 5.6 as a function of the angular frequency ω_L of the kinematic oscillations (which is proportional to the velocity v, see (1.57)). In the region which is below both curves, the kinematic oscillation is possible without slipping. The boundary case between (5.62) and (5.64) corresponds to the intersection points of the curves in Figure 5.6. These values are determined by $\bar{y}_1 = \bar{y}_2$, which leads to the angular frequencies

$$\omega_{L1} = \sqrt{\frac{\alpha_\psi^2 + M_\psi\eta\alpha_y^2}{1 + M_\psi\eta}}, \qquad \omega_{L2} = \sqrt{\frac{\alpha_\psi^2 - M_\psi\eta\alpha_y^2}{1 - M_\psi\eta}}. \tag{5.66}$$

The plots in Figure 5.6 show the results for different typical values of parameters. When the angular frequency of the kinematic oscillation is close to one of the natural angular frequencies of the wheelset then the corresponding critical amplitude tends to infinity. This property leads to the existence of some special kinematic oscillations (denoted by a black dot in Figure 5.6) where the wheelset starts slipping if the velocity of the vehicle increases or decreases.

Determining the connection between the effects of the Coulomb model (5.29) and the nonlinear creep model (5.26) would need a further detailed analysis. It can be seen

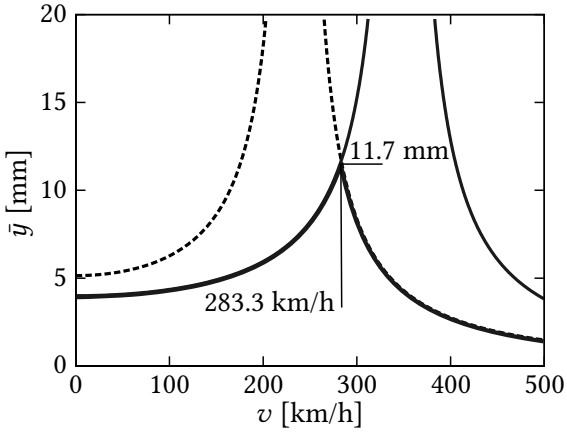

b	r	h^*	F_{load}
0.75 m	0.43 m	0.3	137.2 kN

m	J_ψ	k_y	k_ψ
2000 kg	685 kg m^2	8000 kN/m	6000 kNm

η	μ
1	0.3

Figure 5.7: The data and the results of Example 5.2. The notations of the graph are the same as those of Figure 5.6.

from Figure 5.6 that the nonsmooth Coulomb model does not provide a given critical velocity arising from the linear stability loss of the wheelset. Instead, we get a *velocity-dependent critical amplitude* of the system.

Example 5.2 (Numerical example)**.** The results are demonstrated on a parameter set of a high-speed railway vehicle. In Figure 5.7, the majority of the parameter values originates from the paper of Wu and Chi [74], and parameters μ and η are set to some physically realistic values. From these parameters, we get the natural angular frequencies $\alpha_y = 63.2$ 1/s and $\alpha_\psi = 93.6$ 1/s, and the further composed parameters are $M_\psi = 1.64$ and $C = 10.29$ N/kg. Formulae (5.63)-(5.65) lead to the curves in Figure 5.7. The velocity corresponding to ω_{L1} is $v = 283.3$ km/h, where the two curves intersect each other. This velocity is between the resonance peaks at $v = 236.1$ km/h and $v = 349.3$ km/h, at which values the kinematic oscillation excites the lateral and the yaw motion, respectively.

5.5 New results

Thesis Statement 5. Consider the model of a railway vehicle running with a constant speed along the straight track, where the dynamics of one of its wheelsets is described by the lateral displacement y and the yaw angle ψ. Assume that the linearised differential equations of the kinematics oscillations are written into the form $\dot{y} = \omega_L \eta b \cdot \psi$ and $\dot{\psi} = -\omega_L/(\eta b) \cdot y$, where b is the distance between the contact points on the two rails, η is a dimensionless geometric parameter, and ω_L is the linear angular frequency of the kinematic oscillations.

Assume that the forces acting on the wheelset from the vehicle are modelled by the axle load F_{load} and the elastic forces of effective stiffnesses k_y, k_ψ of the lateral

and yaw suspensions, respectively. The wheelset has a mass m and a mass moment of inertia J_ψ about the vertical axis. The contact between the wheelset and the rails is modelled by Coulomb friction with a uniform coefficient μ for both the static and the dynamic cases.

i) The analysis of the resulting extended Filippov system shows that for small conicity of the wheelset, the dual-point rolling in a state (y, ψ) is realizable if

$$\left(\frac{k_y^2}{m^2} - \omega_L^2\right)^2 y^2 + \left(\frac{k_\psi^2}{J_\psi^2} - \omega_L^2\right)^2 \left(\frac{J_\psi}{m}\right)^2 \psi^2 < \left(\frac{\mu F_{\text{load}}}{m}\right)^2,$$

otherwise, the wheelset starts slipping at both contact points. Moreover, there is no possibility for the slipping of the wheelset at only one of the contact points.

ii) The maximum amplitude of the oscillations without slipping is determined by $\min(\bar{y}_1, \bar{y}_2)$, where

$$\bar{y}_1 = \frac{\mu F_{\text{load}}/m}{\left|k_y^2/m^2 - \omega_L^2\right|}, \qquad \bar{y}_2 = \frac{\eta \mu F_{\text{load}}\, b^2/J_\psi}{\left|k_\psi^2/J_\psi^2 - \omega_L^2\right|}.$$

Related publications: [8], [9], [10].

Conclusion and outlook

In this thesis, the dynamics of a rigid body was investigated with two rolling contacts, which mechanical problem is strongly related to engineering applications, but which has a natural relation to applied mathematics, as well.

In Chapter 1, the analysis of the railway wheelset showed that the kinematic oscillations caused by the dual-point rolling can be quite sensitive to the local geometry of the bodies. The formal dependence of the frequency on the amplitude was determined merely from the structure and the symmetries of the system.

The problem of the indeterminacy of the contact forces at the railway wheelset lead to a different approach of the system, where the conditions of slipping are determined from the trajectories in the phase space. In many cases, the modelling of Coulomb friction by a Filippov system provides an *alternative* method for checking the condition of slipping without calculating the contact forces. In case of dual-point rolling, this *alternative* becomes a *necessary* approach, because the contact forces are undetermined.

For the three-dimensional problem of a dual-point rolling body, it was necessary to extend the theory of Filippov systems to codimension-2 discontinuity manifolds (Chapter 2). Some concepts and tools were obtained for analysing these systems, which might lead to a deeper understanding of Coulomb friction in three-dimensional contact problems. The theory of *extended Filippov systems* contains several open questions, and some further concepts of usual Filippov systems could be possibly generalised for extended Filippov systems.

The developed methods can be used to determine the conditions of slipping in the problem of the dual-point rolling body if the vector fields of the different kinematic cases are compatible (Chapter 3). It would be useful to determine the class of mechanical systems for which the compatibility of the vector fields is satisfied automatically.

The dynamics of the model presented in Chapter 4 is strongly related to a similar system which was analysed briefly in [6]. In that system, the ball is not driven by the fluid flow but by the circular motion of the vessel in the horizontal plane. Further analysis of that system would be useful, because without the complexities of fluid dynamics, an experimental validation of the results could be achieved more conveniently.

The results of Chapter 5 have been derived recently, and there are several further objectives in this project. It would be necessary to compare the dynamics caused by the nonsmooth model of the contact forces with the results from the nonlinear creep

models. The rolling trajectories touching the boundary of the sliding region might lead to limit cycles in a similar way as it was obtained in [5]. In that case, the maximum amplitude without slipping would be an estimation of the limit cycle of the system with the nonlinear creep model.

The usual numerical methods proved to be not reliable for simulating systems with codimension-2 discontinuities. This is the reason why the validation of the analytical results by numerical simulations is missing from Chapters 4 and 5. It seems that the main challenge for the numerical solvers is to follow the trajectories when entering the sliding region from outside of the discontinuity set. It would be necessary to develop numerical algorithms which are capable to follow the trajectories robustly through several transitions between rolling and slipping. Then, the global dynamics of the systems of Chapters 4 and 5 could be investigated, as well. Such a numerical solver can be applied effectively for simulating other problems with three-dimensional frictional contacts, too.

When the sequential results lead to even more tasks and questions about mechanical problems, we can realize the limits of human knowledge. While working on the small questions of science and engineering, we should not forget about the big questions of life.

Deus, propitius esto mihi peccatori.

Bibliography

[1] Alonso, A., Gimenez, J. G., and Garcia, M. Analytical methodology to solve the geometric wheel-rail contact problem taking into account the wheelset yaw angle. In *Proceedings of the 24st IAVSD Symposium, Graz, Austria* (2015), pp. 1–9.

[2] Antali, M. Dynamics of rolling of railway wheelsets. Master's thesis, Budapest University of Technology and Economics, Department of Applied Mechanics, 2013.

[3] Antali, M., and Stepan, G. Nonlinear dynamics of a dual-point-contact ball. In *Proceedings of 8th European Nonlinear Dynamics Conference (ENOC 2014), CD-ROM volume (ISBN: 978-3-200-03433-4)* (2014), H. Ecker et. al., Ed., Vienna University of Technology, pp. 1–2.

[4] Antali, M., and Stepan, G. Nonlinear kinematic oscillations of railway wheelsets of general surface geometry. *Proc. Appl. Math. Mech. 14*, 1 (2014), 303–304.

[5] Antali, M., and Stepan, G. Nonsmooth analysis of a simple rolling-sliding mechanical system with coulomb friction. In *Investigating Dynamics in Engineering and Applied Science (IDEAS 2014), Budapest* (2014). poster.

[6] Antali, M., and Stepan, G. Ket ponton gordulo golyo nem-folytonos dinamikaja (in Hungarian). In *Proceedings of Twelft Hungarian Conference of Mechanics (MAMEK 2015) (ISBN:978-6-155-21674-9)* (2015), A. Baksa, E. Bertoti, and S. Szirbik, Eds., pp. 1–8.

[7] Antali, M., and Stepan, G. Discontinuity-induced bifurcations of a dual-point contact ball. *Nonlinear Dynamics 83*, 1 (2016), 685–702.

[8] Antali, M., and Stepan, G. Loss of stability in a nonsmooth model of dual-point rolling. In *The Dynamics of Vehicles on Roads and Tracks (ISBN: 978-1-138-02885-2)*, M. Rosenberger et. al., Ed. CRC Press, 2016, pp. 937–946.

[9] Antali, M., and Stepan, G. On the nonlinear kinematic oscillations of railway wheelsets. *Journal of Computational and Nonlinear Dynamics 11*, 5 (2016), 1–10.

[10] Antali, M., and Stepan, G. Oscillations of railway wheelsets with discontinuous model of the contact forces. In *6th International Conference on Nonlinear Vibrations, Localization and Energy Transfer, Liege* (2016). poster.

[11] Antali, M., and Stepan, G. Sliding dynamics on codimension-2 discontinuity surfaces. In *Research Perspectives CRM Barcelona – Nonsmooth Dynamics (ISBN: 978-3-319-55641-3)*, M. Jeffrey et al., Ed. Springer-Birkhauser, 2017, pp. 1–4.

[12] Antali, M., Stepan, G., and Hogan, S. J. Kinematic oscillations of railway wheelsets. *Multibody System Dynamics 34*, 3 (2015), 259–274.

[13] Antoine, J.-F., Abba, G., and Molinari, A. A new proposal for explicit angle calculation in angular contact ball bearing. *Journal of Mechanical Design 128* (2005), 468–478.

[14] Ayasse, J.-B., and Chollet, H. *Wheel-Rail Contact. Book chapter in: S. Iwnicki: Handbook of Railway Vehicle Dynamics.* CRC Press, 2006.

[15] Batlle, J. A. The sliding velocity flow of rough collisions in multibody systems. *J. Appl. Mech. 63*, 3 (1996), 804–809.

[16] Campau, D. N. Fluid flow indicator. US Patent, US 4 819 577, 1989.

[17] Carter, F. W. On the action of a locomotive driving wheel. *Proc. Royal Society 112* (1926), 151–157.

[18] de Pater, A. D. The geometrical contact between track and wheelset. *Vehicle System Dynamics 17* (1988), 127–140.

[19] di Bernardo, M., Budd, C. J., Champneys, A. R., and Kowalczyk, P. *Piecewise-smooth Dynamical Systems.* Springer, 2008.

[20] Dieci, L., and Lopez, L. Sliding motion on discontinuity surfaces of high co-dimension. a construction for selecting a Filippov vector field. *Numer. Math. 117* (2011), 779–811.

[21] Eldridge, G., and Eldridge, R. Cyclonic flow meters. US Patent, US 5 905 200, 1999.

[22] EN 15302. *Railway applications – Method for determining the equivalent conicity.* European Comitte for Standardisation, 2008.

[23] Filippov, A. F. *Differential Equations with Discontinuous Righthand Sides.* Kluwer Acacemic Publishers, Dortrecht, 1988.

[24] Gilbert, K. W. Volumetric fluid flow meter. UK Patent, GB 1 246 779, 1970.

[25] Glocker, C. *Set-Valued Force Laws.* Springer, 2001.

[26] Greenwood, D. T. *Advanced Dynamics.* Cambridge University Press, 2003.

[27] Gu-ang, Y., and de Pater, A. D. The determination of the nonlinear motion of a railway vehicle. *Vehicle System Dynamics 20* (1992), 225–239.

[28] Guazzelli, E., and Morris, J. F., Eds. *A Physical Introduction to Suspension Dynamics.* Cambridge University Press, 2012.

[29] Guckenheimer, J., and Holmes, P. *Nonlinear Oscillations, Dynamical Systems, and Bifurcations of Vector Fields.* Springer, 1983.

[30] Hertz, H. Über die Berührung fester elastischer Körper. *Journal f. d. reine u. angewandte Mathematik 92* (1882), 156–171.

[31] Hertz, H. On the contact of elastic solids. In *Mischellaneous Papers by H. Hertz*, D. Jones and G. Scott, Eds. Macmillan, 1896.

[32] Heumann, H. Lauf der Drehgestell-Radsatze in der Geraden. *Organ für die Fortschritte des Eisenbahnwesens 92* (1937), 149–173.

[33] Hoffmann, M., and True, H. The dynamics of european two-axle railway freight wagons with uic standard suspension. *Vehicle System Dynamics 46* (2008), 225–236.

[34] Houlberg, D. M. Fluid flow meter. US Patent, US 4 089 220, 1978.

[35] Iwnicki, S. Simulation of wheel-rail contact forces. *Fatigue Fract Engng Mater Struct 26* (2003), 887–900.

[36] Jeffrey, M. R. Dynamics at a switching intersection: hierarchy, isonomy, and multiple sliding. *J. Appl. Dyn. Syst. 13*, 3 (2015), 1082–1105.

[37] J.Kalker, J. Survey of wheel—rail rolling contact theory. *Vehicle System Dynamics 8*, 4 (1979), 317–358.

[38] Johnson, K. L. *Contact Mechanics*. Cambridge University Press, 1985.

[39] Jordan, D. W., and Smith, P. *Nonlinear Ordinary Differential Equations*, fourth ed. Oxford University Press, 2007.

[40] Kalker, J. J. *On the Rolling Contact of Two Elastic Bodies in the Presence of Dry Friction*. PhD thesis, Delft University of Technology, 1967.

[41] Kalker, J. J. *Three-Dimensional Elastic Bodies in Rolling Contact*. Kluwer Academic Publishers, Dordrecht, 1990.

[42] Kearsley, W. K. Flowmeter. US Patent, US 2 518 149, 1950.

[43] Klingel, J. Über den Lauf von Eisenbahnwagen auf gerader Bahn. *Organ für die Fortschritte des Eisenbahnwesens 38* (1883), 113–123.

[44] Knudsen, C., Feldberg, R., and True, H. Bifurcations and chaos in a model of a rolling railway wheelset. *Phil. Trans. R. Soc. Lond. A 338* (1992), 455–469.

[45] Kumar, S., Kim, J. S., Rao, D. L. P., and Qian, L. Effect of kinematic oscillation on tractive characteristics of steel wheel on rail. *Journal of Engineering for Industry 105* (1983), 61–63.

[46] Kurose, R., and Komuri, S. Drag and lift forces on a rotating sphere in a linear shear flow. *Journal of Fluid Mechanics 384* (1999), 183–206.

[47] Leine, R. I., van Campen, D. H., and van de Vrande, B. H. Bifurcations in nonlinear discontinuous systems. *Nonlinear Dynamics 23*, 2 (2000), 105–164.

[48] Lemaitre, J., Ed. *Handbook of Materials Behavior Models*. Academic Press, 2001.

[49] Lorant, G. Dynamics of rolling wheelsets (in Hungarian). Master's thesis, Budapest University of Technology and Economics, Department of Applied Mechanics, 1993.

[50] Lorant, G., and Stepan, G. The role of non-linearities in the dynamics of a single railway wheelset. *Machine Vibration 5* (1996), 5:18–26.

[51] Marques, F., Flores, P., Claro, J. C. P., and Lankarani, H. M. A survey and comparison of several friction force models for dynamic analysis of multibody mechanical systems. *Nonlinear Dyn. 86* (2016), 1407–1443.

[52] Meijaard, J. P. Kinematic analysis of a wheelset as an aid to understanding and modifying the postcritical behaviour. In *Proceedings of 8th European Nonlinear Dynamics Conference (ENOC 2014), Vienna, Austria* (2014), pp. 1–2.

[53] Meijaard, J. P. The motion of a railway wheelset on a track or on a roller rig. In *Procedia IUTAM* (2016), vol. 19, pp. 274–281.

[54] Noel, D., Rithou, M., Furet, B., and Noch, S. L. Complete analytical expression of the stiffness matrix of angular contact ball bearings. *Journal of Tribology 135*, 4 (2013), DOI: 10.1115/1.4024109.

[55] Pennestri, E., Rossi, V., Salvini, P., and Valentini, P. Review and comparison of dry friction models. *Nonlinear Dyn. 83* (2016), 1785–1801.

[56] Peters, M. L. J. P. Orbital ball flow meter for liquids and gases. World Intellectual Property Organization, WO 01/25829 A1, 2001.

[57] Peters, M. L. J. P. Orbital ball flowmeter for gas and fluis. US Patent, US 8 505 378 B2, 2013.

[58] Polach, O. Characteristic parameters of nonlinear wheel/rail contact geometry. In *Proceedings of the 21st IAVSD Symposium, Stockholm, Sweeden* (2009), pp. 1–12.

[59] Pritchard, P. J. *Introduction to Fluid Mechanics*, 8 ed. Wiley, 2011.

[60] Reynolds, O. On rolling friction. *Phil. Trans. Royal Society 166* (1875), 155.

[61] Rubinow, S. I., and Keller, J. B. The transverse force on a spinning sphere moving in a viscous fluid. *Journal of Fluid Mechanics 11*, 3 (1961), 447–459.

[62] Sallai, G. Dispositif de mesure pour ecoulements fluidiques. French Patent, FR 2 368 698, 1978.

[63] Schwab, A. L., and Meijaard, J. P. Two special finite elements for modelling rolling contact in a multibody environment. In *Proceedings of the 1st Asian Conference on Multibody Dynamics, Iwaki, Japan* (2002), pp. 386–391.

[64] Stichel, S. Limit cycle behaviour and chaotic motions of two-axle freight wagons with friction damping. *Multibody System Dynamics 8* (2002), 243–255.

[65] Strogatz, S. H. *Nonlinear Dynamics and Chaos.* Perseus Books, 1994.

[66] Szabo, Z., and Lorant, G. Parametric excitation of a single railway wheelset. *Vehicle System Dynamics 33* (2000), 49–55.

[67] UIC Code 519. *Method for determining the equivalent conicity.* International Union of Railways, 2004.

[68] Utkin, V. I. *Sliding Modes in Control and Optimization.* Springer, 1992.

[69] Vermeulen, P. J., and Johnson, K. L. Contact of nonspherical elastic bodies transmitting tangential forces. *Journal of Applied Mechanics 31*, 2 (1964), 338–340.

[70] Welker, R. *Continuous Contamination Monitoring Systems. Book chapter in: R. Kohli et al.: Developments in Surface Contamination and Cleaning - Vol. 2.* Elsevier, 2009.

[71] Wickens, A. H. The dynamic stability of railway vehicle wheelsets and bogies having profiled wheels. *Int. J. Solids Structures 1* (1965), 319–341.

[72] Wickens, A. H. *A History of Railway Vehicle Dynamics. Book chapter in: S. Iwnicki: Handbook of Railway Vehicle Dynamics.* CRC Press, 2006.

[73] Wiggins, S. *Introduction to Applied Nonlinear Dynamical Systems and Chaos*, 2nd ed. Springer, 2003.

[74] Wu, X., and Chi, M. Parameters study of hopf bifurcation in railway vehicle system. *Journal of Computational and Nonlinear Dynamics* (2015), 1–10. 031012.

[75] Yukinori, O., and Shui, Y. Flow rate detecting device. European Patent Office, EPO 0 172 451, 1986.

[76] Zhao, J.-S., and et al. Effects of gyroscopic moment on the damage of a tapered roller bearing. *Mechanism and Machine Theory 69* (2013), 185–199.

A. M. D. G.